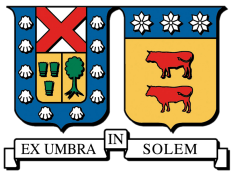

UNIVERSIDAD TÉCNICA FEDERICO SANTA MARÍA
DEPARTAMENTO FÍSICA

Interfacial Dzyaloshinskii-Moriya Interaction in Thin Magnetic Nanotubes

Benjamín Andrés Mimica Figari

Thesis presented to the physics department at Universidad Técnica Federico Santa María to obtain the Masters degree in physics.

March 2023

Valparaíso, Chile

Advisor: Dr. Pedro Landeros

Co-Advisor: Dr. Rodolfo Gallardo

CONSTANCIA DE VALIDACIÓN Y CONFIDENCIALIDAD DE MONOGRAFÍA A REPOSITORIO ACADÉMICO

1.- IDENTIFICACIÓN DEL TRABAJO ACADÉMICO

Tipo de monografía (marcar una opción): ☐ Memoria o trabajo de título; ☒ Tesis de Postgrado;

Título del trabajo: Interfacial Dzyaloshinskii-Moriya Interaction in Thin Magnetic Nanotubes

Nombre del candidato(a): Benjamín Andrés Mimica Figari

Carrera / Grado: Magister en Ciencias con Mención en Física

Campus: Casa Central Valparaiso **;** **Departamento**: Física

2.- VALIDACIÓN DEL PROFESOR GUÍA/DIRECTOR DE TESIS

Yo, Pedro Landeros, en mi calidad de profesor(a) guía/director(a) del trabajo académico mencionado anteriormente **DEJO CONSTANCIA** que:

- He revisado esta versión del documento y corresponde a la versión final aprobada del trabajo.
- El trabajo cumple con los requisitos académicos y de formato establecidos por la institución

3.- EVALUACIÓN DE CONFIDENCIALIDAD POR PROPIEDAD INDUSTRIAL

☒ El trabajo **NO contiene información que amerite confidencialidad** y puede ser publicado de inmediato en repositorio con acceso abierto.

☐ El trabajo **CONTIENE** información con potenciales implicancias de propiedad industrial o intelectual y requiere un periodo de confidencialidad (embargo) por:

☐ 6 meses; ☐ 12 meses; ☐ 2 años; ☐ 3 años; ☐ 5 años; ☐ 10 años

Fundamentación de la necesidad de confidencialidad (obligatorio si se solicita embargo):

4.- FIRMAS

Profesor(a) guía o director(a) de memoria o tesis:

Fecha: 17-06-2025 ; **Firma:** _____

Estudiante o Candidato(a):

Fecha: 17-06-2025 ; **Firma:** _____

Este formulario debe ser insertado como página 2 de la memoria o tesis, completado y firmado por estudiante y profesor(a) antes de la entrega en portal PRISMA de Biblioteca USM.

Thesis title: Interfacial Dzyaloshinskii-Moriya interaction in thin magnetic nanotubes.

Author: **Benjamín Andrés Mimica Figari**

Comittee: Dr. Pedro Landeros (Advisor)

Dr. Rodolfo Gallardo (Co-Advisor)

Dr. Alejandro Riveros

He's so stupid, he doesn't realize how miserable he should be.

- Bojack Horseman

Acknowledgements

I want to express my gratitude to my advisor, Pedro, who has been of enormous help throughout this process. Not everyone has the same luck as I did, to have the guidance of an exceptionally experienced person and, at the same time, always deeply invested in my work. He took the time to guide me with care and attention, also valuing my ideas and allowing for my independence. I genuinely couldn't have asked for a better advisor.

Thanks to the magnetism group at USM. They have built a brilliant, hard-working, and pleasant group of people who not only like to produce excellent scientific work, but can also make it a fun process. Thanks to Rodolfo for being always willing to have great discussions and for offering very valuable insight. He was happy to help me with a big part of this work, even though I am not his student, but he certainly is the non-official co-advisor to this project. A special thanks to Felipe, who always shares his nice coffee with me in the office, and most importantly, he did the simulations that backed the results presented in this project. Thanks to Andreas and Paolo for receiving me at nanoGUNE and discussing important aspects of this work with me. I am grateful, not only for what I learned with them in physics, but also for inspiring me with their great experience and the impeccable work they have done there. Thanks also to Alejandro for agreeing to be part of the committee and reviewing this work and giving valuable insight and feedback.

I also want to thank my family for always being supportive. The more I grow, the more I realize that they are the most important, and I am every day trying to be a better son, brother, and cousin. Thank you, Mom, for your love and care. You are the reason for the person I have become today. You always say that you have to be "positive", and that is an invaluable lesson that everyone should keep deep in their hearts. Thanks to Martín, my brother and friend. I am always very proud of you for becoming the charming, honest, and intelligent person you are now. Thank you, Edu, for being my second father. I admire your patience and willingness to always help everyone around you. Thank you, Dad and Sole, for being a crucial part of my life here at Valparaíso. I value the happy family you have built, and your loving care for my beautiful little brother, Bauti,

to whom I am grateful for his friendship. Thank you for letting me play with your favorite car. Thank you, Ami, my grandmother, for your unconditional love. We all miss you very much, but know you are in a good place.

Thank you, Tammy, my love and partner. Thank you for the laughter and dances we have shared. Your empathy and kind heart are beautiful. I admire you for wanting to improve as a person every day. I love you immensely and feel very loved by you. Thank you to all my friends, especially to Sergio and Jorge, for working beside me and for making this a fun process. Sorry for being so annoying.

Finally, I would like to thank Fondecyt grant 1241589 and Basal Program for Centers of Excellence, Grant AFB220001 (CEDENNA), for their financial support, which made this thesis possible.

Abstract

In finite crystalline lattices, the Dzyaloshinskii-Moriya interaction (DMI) can lead to interesting phenomena like the formation of chiral arrangements of magnetic moments—magnetic textures that lack spatial inversion symmetry—and also to non-reciprocal propagation of spin waves. In this thesis work, the influence of the DMI in thin magnetic nanotubes is studied. A conical-helix magnetization distribution is proposed in the presence of interfacial DMI based on the results of chiral structures induced by DMI on a planar ultrathin film. The total internal energy of the conical-helix texture in the curved membrane is calculated and used to determine its properties, such as its orientation and wavelength, given by the pitch vector of the helix. To determine the low-energy spin configurations and the magnetic reversal modes in the presence of interfacial DMI, the energy and nucleation field of the conical-helix texture are compared with the usual textures in magnetic nanotubes that appear in the absence of DMI. The well-known magnetochiral features that arise from the dipolar field in a curved environment are further explored since the exchange and DMI may also produce handedness in the magnetic behavior. Non-reciprocal counter-propagating spin waves are also explored in nanotubes. By parametrizing the equilibrium magnetization between the saturated state along the symmetry axis of the nanotube and the vortex state, the propagating waves over these two states are compared. The interfacial DMI is known to cause frequency differences between counter-propagating spin waves in the direction perpendicular to the equilibrium magnetization and the normal to the interface. This effect either reinforces or opposes the dipolar-induced non-reciprocity. The formation of the helix textures can also be determined by analyzing the spin-wave dispersion in the fully saturated state stabilized at high external magnetic fields. The reduction of this field achieves a critical value at which the frequency of a particular normal mode reaches zero. This critical field coincides with the nucleation field of the corresponding conical-helix texture with the same wavelength.

Contents

Chapter 1

Nanomagnetism

Nanomagnetism is the area of research in Physics that deals with the magnetic properties of objects with at least one dimension in the nanoscopic range ($1 - 100$ nm). These objects include, for instance, *nanoparticles, nanowires, thin films, multilayers* [1], and do not only provide interesting ideas for fundamental physics studies but also have multiple applications in technology. For instance, the ability to manipulate nanoparticles has enabled advances in medical applications like hyperthermia, targeted drug delivery, and imaging, even postulating them as a possible important tool in cancer treatment [2]. An important example is the discovery of the giant magnetoresistance (GMR) effect in multilayer arrangements of layers of nanometric thickness thin magnetic films. Fert and Grünberg discovered this effect independently in the late 1980s [3, 4], and were later awarded the 2007 Nobel Prize in Physics due to its impact on the technique of data storage and magnetic sensors [5, 6].

From a theoretical point of view, the knowledge of basic magnetic properties—such as the internal magnetic structure or equilibrium states, magnetization reversal process, nucleation field, and coercivity—is of fundamental importance to understand the phenomenology of ferromagnetic materials. Pierre Weiss proposed one of the earliest models to explain ferromagnetism in 1907, introducing the concept of magnetic domains—regions where magnetic moments are aligned [7]. However, very complex structures can arise due to short-distance interactions. *Magnetic Textures* refer to magnetic ground states with a non-collinear alignment of magnetic moments [8]. Among them, chiral magnetic structures have gained significant attention in recent years [9]. On bulk materials, non-centrosymmetric lattices can give rise to

chiral magnetic structures [10, 11]. Low-dimensional systems, such as thin films, can lack structural inversion symmetry, leading to chiral spin textures [12–14] due to the emerging Dzyaloshinskii-Moriya interaction (DMI)—also known as anti-symmetric exchange interaction—, like helical structures [15], bimerons [16], skyrmions and anti-skyrmions [17, 18]. The former are especially interesting due to their potential as topologically stable bits to store information in memory and logic devices [19]. Because of its non-symmetrical nature, it also plays a crucial role in spin-wave dynamics and non-reciprocal phenomena [20, 21], making it a key interaction for modern spintronic and magnonic applications.

Magnonics is the area of physics that deals with the excitation, propagation, control, and detection of spin waves through magnetic media [22, 23]. Analogous to electric currents, magnon-based waves can be used to carry, transport, and process information [24], leading to the invention, for instance, of magnon transistors [25]. The experimental observation of the propagation of magnons created by the spin-transfer torque was reported [26]. Using spin-Hall effects enables the direct conversion of an electric signal into a spin wave and its subsequent transmission over macroscopic distances [27]. Non-reciprocity—the difference in amplitude or frequency between counter-propagating spin waves—offers potential magnonic applications such as circulators, isolators, phase shifters, diodes, and even logic devices [28–30].

Interesting phenomena emerge from geometrically curved magnetic objects [31, 32]. In curved systems, chiral effects can be induced by dipolar or exchange interactions [33, 34], which have been identified as a curvature-induced DMI [35]. For example, vortex domain walls are highly sensitive to chirality due to the dipolar interaction [36, 37]. In this context, *magnetic nanotubes* have been widely investigated in the last decades [38–41] as they have interesting properties and tunable characteristics [42]. Arrays of magnetic nanofibers with desired geometry, composition, and structures can be synthesized, for example, by electrochemical deposition [43]. Small-size nanotubes have been found to reverse their magnetization through coherent rotation or a curling mode depending on geometry [44]. In this regime, there is no space for the apparition of domain walls. As the size of the nanotubes increases, additional interactions besides exchange interaction may become important, and other types of reversal modes may happen, such as vortex domains forming at

the tube ends [45, 46]. The propagation of spin waves can also be altered by curvature. For instance, nanotubes with a vortex magnetization state exhibit spin-wave nonreciprocity due to the curvature-induced chiral dipolar interaction. This can lead to different frequencies [47–49] or attenuation lengths for spin waves traveling in opposite directions [50].

The present work studies the stability of magnetic textures and the spin-wave dynamics in thin magnetic nanotubes using the Micromagnetic Theory [51]. The key assumption of the Micromagnetic Theory is that the magnetic nature of a system can be described using a continuous field called *magnetization*:

$$\boldsymbol{M}(\boldsymbol{r}) = M_s \boldsymbol{m}(\boldsymbol{r}), \qquad |\boldsymbol{m}(\boldsymbol{r})|^2 = 1. \tag{1.1}$$

Such a field changes smoothly over the system and can be regarded as constant over distances smaller than a characteristic length, determined by the strength of the magnetic interactions, which are specific for each ferromagnetic material. In general, the magnetic interactions in a ferromagnetic material are complex, and determining how their constituent spins can be organized is a difficult task. Moreover, the specific structure that emerges not only depends on the present conditions to which the material is subjected but also on the history of any externally applied magnetic field.

1.1 Magnetic Ground State

A physical magnetic configuration must be energetically stable. The energy of a ferromagnetic system in terms of the magnetization is given by

$$E(\boldsymbol{m}) = \iiint_V w(\boldsymbol{m}) dV, \tag{1.2}$$

where the energy density $w(\boldsymbol{m})$ can be obtained from a discrete description of spin-spin interactions as shown in Section 1.2. To find a stable magnetic configuration, the energy must be minimized with respect to the magnetization field. The solution of $\boldsymbol{m}$ is such that the functional differential vanishes for an arbitrary direction $\boldsymbol{v}$ [52]:

$$\delta E(\boldsymbol{m}, \boldsymbol{v}) = \frac{d}{d\epsilon} \iiint_V w(\boldsymbol{m} + \epsilon \boldsymbol{v}) dV = 0. \tag{1.3}$$

In general, this functional differential includes not only an integral of the energy density in the bulk but also a boundary condition to be satisfied by the magnetization field:

$$\delta E = \iiint_V \frac{\delta w}{\delta \boldsymbol{m}} \cdot \boldsymbol{v} dV + \iiint_{\partial V} \boldsymbol{B} \cdot \boldsymbol{v} dS. \tag{1.4}$$

By using Lagrange multipliers, the solution to this problem subject to the condition (1.1) yields the Brown equations [53], which includes the boundary conditions and the equilibrium condition

$$\boldsymbol{m} \times \boldsymbol{H}^{\text{eff}} = 0 \tag{1.5a}$$

$$\boldsymbol{m} \times \boldsymbol{B} = 0, \tag{1.5b}$$

where the definition of the effective magnetic field is

$$\boldsymbol{H}^{\text{eff}} = -\frac{1}{\mu_0 M_s} \frac{\delta w}{\delta \boldsymbol{m}}. \tag{1.6}$$

Accordingly, the equilibrium condition requires a magnetization parallel to an effective magnetic field produced by all spin-spin interactions.

1.2 Magnetic Interactions

A magnetic dipole $\boldsymbol{\mu}$ experiences a torque in the presence of a magnetic field $\boldsymbol{H}$

$$\boldsymbol{\tau} = \boldsymbol{\mu} \times \boldsymbol{H}. \tag{1.7}$$

Accordingly, the energy of a magnetic dipole $\boldsymbol{\mu}$ in the presence of an external magnetic field $\boldsymbol{H}$ is

$$E_{\text{ze}} = -\mu_0 \boldsymbol{\mu} \cdot \boldsymbol{H}, \tag{1.8}$$

which is known as the Zeeman interaction. This energy is minimized when the dipole is aligned with the direction of the applied magnetic field. The total energy of a collection of magnetic dipoles $\boldsymbol{\mu}_i$ is just the sum $E = -\mu_0 \sum_i \boldsymbol{\mu}_i \cdot \boldsymbol{H}$. In terms of the continuous magnetization field given in Eq. (1.1), the total Zeeman

energy in the continuous limit is

$$E_{\text{ze}} = -\mu_0 \iiint_V M_{\text{s}} \boldsymbol{m} \cdot \boldsymbol{H} dV. \tag{1.9}$$

This interaction explains one of the important characteristics of a ferromagnetic material: when subjected to a sufficiently strong magnetic field, it acquires a net magnetization along its direction. Nevertheless, it becomes necessary to understand and develop a theory that includes other kinds of coupling within the system to explain the formation of magnetic textures and the remanent magnetization evidenced by hysteresis loops of ferromagnetic materials.

1.2.1 Exchange interaction

In addition to the Coulomb interaction, the Pauli principle induces a correlation between spin states in neighboring sites of a crystal. This interaction results in an energy difference between the parallel and anti-parallel spin states[1]. To illustrate this effect, consider two electrons in neighboring sites. The Coulomb repulsion between the two particles is minimized if the overlapping wave function is anti-symmetric in space and, therefore, has low amplitude where such interaction is most relevant, as illustrated in Fig. 1.1. Because the total wave function of fermions has to be anti-symmetric, the spin state has to be symmetric. Therefore, the alignment of neighboring spins along the same direction results in a lower energy expectation value. In the context of micromagnetism, the *Heisenberg Hamiltonian* provides a semiclassical approach to describe this interaction, given by the expression

$$\mathscr{H}_{\text{ex}} = -\sum_{\langle ij \rangle} J_{ij} \boldsymbol{S}_i \cdot \boldsymbol{S}_j, \tag{1.10}$$

where the summation is done over neighbor sites and J_{ij} are the exchange integrals. The case $J_{ij} > 0$ describes a ferromagnetic coupling as illustrated above, while antiferromagnetic materials can be described with $J_{ij} < 0$. Assuming a homogeneous system, the exchange integrals $J_{ij} = J$ can be considered independent of the site. Also, by noting that $|\hat{\boldsymbol{S}}_i - \hat{\boldsymbol{S}}_j|^2 = 2 - 2\hat{\boldsymbol{S}}_i \cdot \hat{\boldsymbol{S}}_j$, it

[1] Details are extensive. A good fundamental discussion can be found, for example, at references [51, 54, 55].

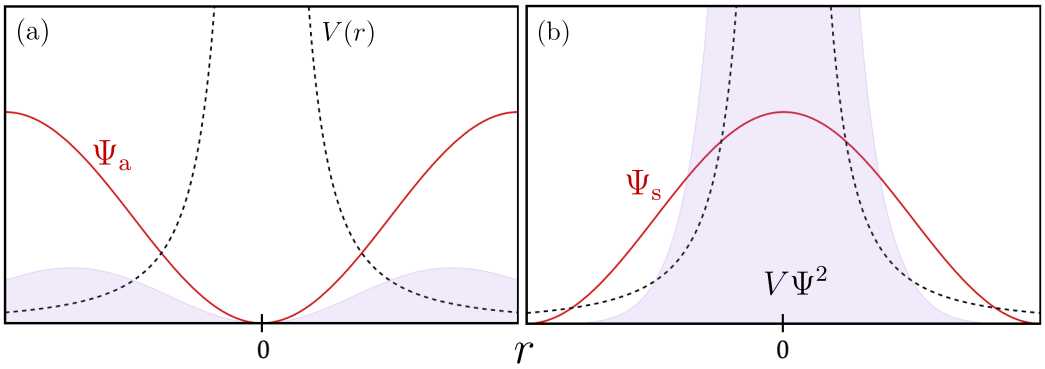

Figure 1.1: Antisymmetric (a) and symmetric (b) wave functions illustration. Dashed line represents the Coulomb interaction and purple area measures its expected value $E_C \sim \int_\Omega V\Psi^2 d\Omega$, and it is shown to be more relevant around $r = 0$. The antisymmetric overlapping of two functions vanishes when the spatial coordinates of the two particles are the same ($r = x_1 - x_2 = 0$), while the symmetric does not.

is obtained

$$\mathscr{H}_{\text{ex}} = \frac{S^2 J}{2} \sum_{\langle ij \rangle} |\hat{\boldsymbol{S}}_i - \hat{\boldsymbol{S}}_j|^2, \tag{1.11}$$

where the constant term that does not depend on the spins has been neglected. The former Hamiltonian in terms of the continuous magnetization field—Eq. (1.1)— is given by the discrete summation over neighboring sites

$$\begin{aligned} \mathscr{H}_{\text{ex}} &= \frac{S^2 J}{2} \sum_{\langle ij \rangle} \left(\boldsymbol{m}(\boldsymbol{r}_i) - \boldsymbol{m}(\boldsymbol{r}_i + \Delta \boldsymbol{r}_j)\right)^2 \\ &\approx \frac{S^2 J}{2} \sum_{\langle ij \rangle} \left(\nabla \boldsymbol{m}(\boldsymbol{r}_i) \cdot \Delta \boldsymbol{r}_j\right)^2 . \end{aligned} \tag{1.12}$$

Here, a first-order Taylor expansion has been considered where $\nabla \boldsymbol{m}$ denotes the Jacobian of the magnetization field. By considering a specific lattice structure, the last summation can be transformed into an integral. For example, a BCC lattice yields[2]

$$E_{\text{ex}} = \iiint_V A[(\nabla m_x)^2 + \left(\nabla m_y\right)^2 + (\nabla m_z)^2]\text{dV}, \tag{1.13}$$

[2]Details of this calculation can be found in Appendix 3 of Reference [56] or Chapter 2 of reference [1].

where $A = 2JS^2/a$ is the *exchange stiffness constant* and a denotes the lattice constant. Because the exchange interaction favors the alignment of neighboring spins, the exchange constant is related to the distance along which the spins can be considered collinear—and thus the magnetization field can be considered constant. This distance is called *exchange length* and is defined as

$$l_{\text{ex}} = \sqrt{\frac{2A}{\mu_0 M_s^2}}. \tag{1.14}$$

The exchange effective field, obtained using the variational derivative as explained in Section 1.1 is

$$\boldsymbol{H}_{\text{ex}} = M_s l_{\text{ex}}^2 \nabla^2 \boldsymbol{m}. \tag{1.15}$$

1.2.2 Anisotropy

There are several types of anisotropy, the most common of which is the magnetocrystalline anisotropy caused by the spin-orbit interaction. The electron orbits depend on the crystallographic structure, and their interaction with the spins makes the latter align along well-defined crystallographic directions [51, 57]. One example is the *uniaxial anisotropy*, where the energy only depends on the angle the spins make in a particular direction $\hat{\boldsymbol{n}}$. The magnetic energy due to the anisotropy is

$$E_{\text{u}} = -\iiint_V K_{\text{u}} (\boldsymbol{m} \cdot \hat{\boldsymbol{n}})^2 dV, \tag{1.16}$$

where K_{u} is the anisotropy constant. When K_{u} is positive, $\hat{\boldsymbol{n}}$ is called the easy axis. On the other hand, when K_{u} is negative, $\hat{\boldsymbol{n}}$ is called the hard axis, and the plane perpendicular to it is called the easy plane. Then, the effective anisotropy field is

$$\boldsymbol{H}_{\text{u}} = \frac{2}{\mu_0 M_s} K_{\text{u}} \hat{\boldsymbol{n}} (\hat{\boldsymbol{n}} \cdot \boldsymbol{m}). \tag{1.17}$$

1.2.3 Dipolar interaction

In the absence of free currents, the Maxwell equations corresponding to magnetostatics can be written as

$$\nabla \times \boldsymbol{H} = 0 \tag{1.18a}$$

$$\nabla \cdot \boldsymbol{H} = -\nabla \cdot \boldsymbol{M}. \tag{1.18b}$$

These equations resemble the equations of electrostatic theory. That is, the two missing Maxwell equations

$$\nabla \times \boldsymbol{E} = 0 \tag{1.19a}$$

$$\nabla \cdot \boldsymbol{E} = \frac{\rho}{\epsilon_0}. \tag{1.19b}$$

Mathematically, the two sets of differential equations are the same; therefore, the well-known methods of electrostatic theory can be applied. In particular, the divergence of the magnetization can be regarded as an effective magnetic charge density. In consequence, after considering the correct boundary conditions, the magnetic field can be found through a scalar potential [58] $\boldsymbol{H}_\mathrm{d} = -\nabla\Phi$, where:

$$\Phi = \iiint_V \frac{\rho_\mathrm{m}(\boldsymbol{r}')}{4\pi|\boldsymbol{r}-\boldsymbol{r}'|}dV' + \iint_{\partial V} \frac{\sigma_\mathrm{m}(\boldsymbol{r}')}{4\pi|\boldsymbol{r}-\boldsymbol{r}'|}dS'. \tag{1.20}$$

Here $\rho_\mathrm{m} = -\nabla \cdot \boldsymbol{M}$ and $\sigma_\mathrm{m} = \hat{\boldsymbol{n}} \cdot \boldsymbol{M}$ are the corresponding volumetric and superficial *effective magnetic charges*. The three-fold integration of Eq. (1.20) considers the dipolar magnetic field produced by every magnetized part of the system. Since the dipole-dipole interaction is long-ranged, the total energy corresponds to the interaction of this magnetic field through the whole material:

$$E_\mathrm{d} = -\frac{\mu_0}{2}\iiint_V \boldsymbol{H}_\mathrm{d} \cdot \boldsymbol{M}dV. \tag{1.21}$$

1.2.3.1 Pole avoidance principle

The dipolar energy involves a very complex six-fold integration calculation. Although Eq. (1.21) gives a direct but complicated way to compute the dipolar energy, it can also give indirect insight into what the dipolar energy avoids. It

can be proved that the dipolar energy can be computed as[3]

$$E_{\mathrm{d}} = \frac{\mu_0}{2} \iiint_V \boldsymbol{H}_{\mathrm{d}}^2 dV. \tag{1.22}$$

This last equation proves the *pole avoidance principle*. The integrand is real and positive everywhere. This means that the lowest possible value of the dipolar energy term is zero, which can only be achieved when the dipolar field $\boldsymbol{H}_{\mathrm{d}}$ is zero everywhere. Therefore, the magnetostatic energy always favors magnetic configurations without volumetric or surface magnetic charges. In determining the formation of magnetic textures, this not only gives a good intuition of the actual solution of the problem but also in some cases allows for approximations of this energy term. For example, in ultrathin films where the volumetric charge ρ_{m} is negligible, the dipolar term will mainly avoid the formation of surface charges $\sigma_{\mathrm{m}} = \hat{\boldsymbol{n}} \cdot \boldsymbol{M}$, and as such it can be approximated as a local hard-axis anisotropy.

1.2.4 Dzyaloshinskii-Moriya

The Dzyaloshinskii-Moriya interaction (DMI) is an anti-symmetrical exchange coupling that favors canted or helical-like spin structures. Such interaction occurs in crystals lacking inversion symmetry [17] or it is induced through symmetry breaking at large spin-orbit coupled interfaces [59]. It was first proposed by Dzyaloshinskii [60, 61] and then by Moriya [62] as a higher-order contribution from the spin-orbit coupling effect. The DMI between neighboring spins is modeled as mediated by a vector $\boldsymbol{D}_{ij}$ and is represented by the following Hamiltonian

$$\mathscr{H}_{\mathrm{dmi}} = \sum_{\langle ij \rangle} \boldsymbol{D}_{ij} \cdot (\boldsymbol{S}_i \times \boldsymbol{S}_j), \tag{1.23}$$

where $\boldsymbol{D}_{ij}$ depends on the crystalline structure of the material [63–65]. Fig. 1.2 shows the DMI vector induced in the interface of a ferromagnetic material with a metal layer with strong spin-orbit coupling. The vector $\boldsymbol{D}_{12}$ lies perpendicular to the plane formed by the two magnetic sites and the metal site. Therefore, the DM interaction between neighboring spins is minimized when the two spins are perpendicular. The figure shows that the DMI favors the clockwise rotation of the magnetization as one moves in the $+y$ direction. Under a spatial inversion

[3] For demonstration details see reference [51] Section 7.3.2

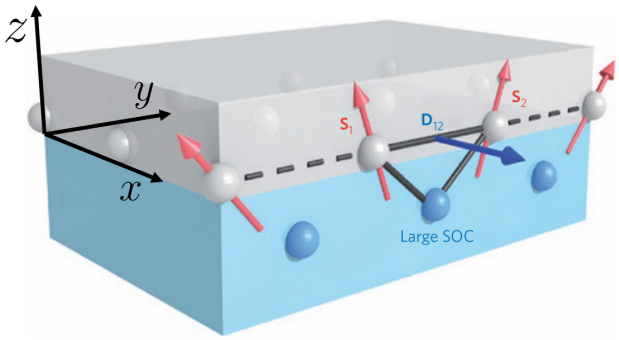

Figure 1.2: DMI at the interface between a ferromagnetic material (grey) and a metal with a strong spin-orbit coupling (blue). Figure reproduced from Ref. [66].

transformation ($\boldsymbol{r} \rightarrow -\boldsymbol{r}$), the metallic layer ends on top of the ferromagnetic material, and the $\boldsymbol{D}_{12}$ vector is inverted. In this case, the DM interaction will favor a counter-clockwise rotation of the magnetization as one moves in the $+y$ direction.

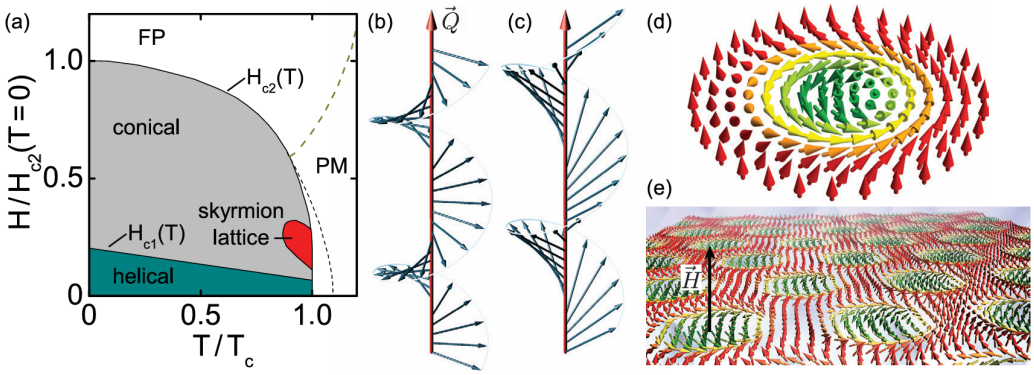

Figure 1.3: Magnetic phase diagram of the formation of chiral structures stabilized by DMI (a), defining the critical field H_{c2} and the critical temperature T_c. PM represents the paramagnetic phase, and FP the field-polarized state. Illustrations of (b) helical and (c) conical spin texture. $\vec{Q}$ is the helical propagation vector. (d) Spin texture of a Bloch-type individual magnetic skyrmion. (e) Skyrmion lattice forming in a plane perpendicular to the applied field $\vec{H}$. Figure reproduced from Ref. [11].

The DM interaction can stabilize periodic magnetic configurations like helices and skyrmion lattices, as illustrated in Fig. 1.3. Magnetic *skyrmions* are nanometric swirling topological structures in the magnetization texture (see Fig. 1.3 (d)) that have drawn increasing scientific attention in the last decade due to their potential as topologically stable bits to store information in memory and

logic devices [19]. On the other hand, *helical* textures are wave-like periodic magnetic structures as shown in Fig. 1.3 (b-c). In thin magnetic films, helical textures have been found as a possible magnetic ground state in the presence of interfacial DMI [67]. Moreover, their wave-like nature allows for a direct connection with magnonic excitations as discussed in Chapter 4.

This work focuses on the texture formation and the spin-wave dynamics of nanotubes with interfacial DMI. The micromagnetic interfacial DMI energy is obtained for a nanotube with a ferromagnetic/heavy metal interface with its normal in the radial direction (see Fig. 2.1) in the supplementary material of Ref. [68]:

$$E_{\text{dmi}} = \iiint_V D\hat{\boldsymbol{\rho}} \cdot (\boldsymbol{m}(\nabla \cdot \boldsymbol{m}) - (\boldsymbol{m} \cdot \nabla)\boldsymbol{m}) dV. \tag{1.24}$$

The effective field in this case is given by

$$\boldsymbol{H}_{\text{dmi}} = -\frac{2D}{\mu_0 M_{\text{s}}}\left(\hat{\boldsymbol{\rho}}(\nabla \cdot \boldsymbol{m}) - \nabla(\boldsymbol{m} \cdot \hat{\boldsymbol{\rho}}) + \frac{m_\phi}{\rho}\hat{\boldsymbol{\phi}}\right). \tag{1.25}$$

The details for the derivation are given in Appendix B. The term $m_\phi \hat{\boldsymbol{\phi}}/\rho$ can be attributed to the curved geometry of the system. An additional term $(m_\phi/\rho)\hat{\boldsymbol{\phi}}$ is obtained here in comparison with the result reported in Ref. [52] where a planar system is assumed.

1.3 The Nucleation Problem

One of the main characteristics of ferromagnetic materials is that their magnetization state depends on the history of the applied magnetic field. An important consequence is that the energy minimization of a magnetic system is meaningless on its own, as even if one can find an energetically stable magnetic state, this state is not necessarily available to the system. A way to address this problem is to align the magnetization along a particular direction by the action of a strong external magnetic field. The beginning of the reversal from the fully saturated state is called the *nucleation* process. A mechanical analogy is shown in Fig. 1.4. At point (a) the ball is at a local minimum. Even though there is a lower energy state, it is not available for the system. The energy landscape can be changed by exerting an external force. When this force reaches a critical value F_{crit}, the former state is no longer stable, and the system is required to

change to another minimum of energy, as shown in Figure (c). The essential idea is to begin from a known stable initial state, achieved by the modification of a control parameter or external force, and examine the transition to a different state.

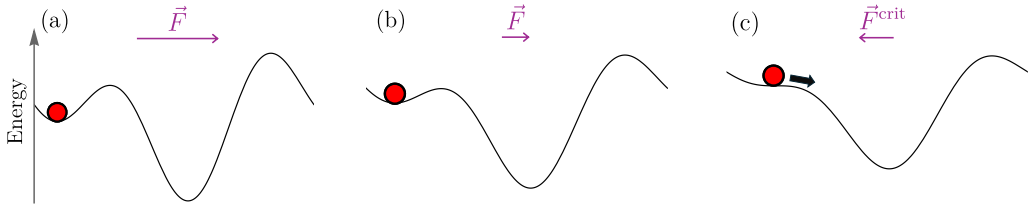

Figure 1.4: The energy landscape is changed by an externally applied force. In point (a), the force applied maintains the ball at a stable point. When this force is diminished (b), this state becomes less stable until it reaches a critical force (c) at which the ball has to move to a new energy value.

A way to study the nucleation process in ferromagnetic systems is using the linearized Brown equations (1.5b) and analyzing small changes from the saturated state [51]. A different approach will be taken here. A rotational mode $\boldsymbol{m}_\alpha(\boldsymbol{r}, \theta)$ is proposed as an ansatz solution for the reversal from the saturated state along the nanotubes axis $\hat{\boldsymbol{z}}$, where θ is the angle between the magnetization and the external magnetic field. Therefore, the energy of the system is a function of the magnetization and the applied magnetic field $E(\boldsymbol{m}_\alpha, \boldsymbol{H})$. For a sufficiently large applied field, the following conditions over the energy hold

$$\frac{\partial E}{\partial \theta}(\theta = 0) = 0, \qquad \frac{\partial^2 E}{\partial \theta^2}(\theta = 0) > 0, \tag{1.26}$$

and consequently the saturated state $\theta = 0$ is a stable energy minimum of the system. The nucleation process occurs when, by decreasing the applied field, the condition

$$\frac{\partial^2 E}{\partial \theta^2}(\theta = 0) = 0, \tag{1.27}$$

is achieved. At this point, the saturated state becomes unstable and the magnetic configuration starts to change (see Fig. 1.4). The value of the magnetic field at which this process occurs H_{n}^{α} is called the *nucleation field*. Because it was calculated using an ansatz, this nucleation field value has to be compared with other potential rotational modes. The actual rotational mode that will happen will have the highest value of the nucleation field. That is because, if a different rotational mode $\boldsymbol{m}_\beta$ starts at a nucleation field $H_{\text{n}}^{\beta} > H_{\text{n}}^{\alpha}$, then by decreasing the

applied field from a saturated state, the higher value will be achieved first and the $\boldsymbol{m}_\alpha$-rotation will no longer be available to the system.

1.4 Dynamics: Landau-Lifshitz-Gilbert equation

Spin waves on magnetic structures are perturbations of the magnetic ground state. The quanta of magnetic oscillations are magnons. To describe the temporal evolution of magnetization, the Landau-Lifshitz-Gilbert equation is used

$$\frac{d}{dt}\boldsymbol{M}(\boldsymbol{r},t) = -\mu_0\gamma\boldsymbol{M}(\boldsymbol{r},t)\times\boldsymbol{H}^{\text{eff}}(\boldsymbol{r},t) - \lambda\boldsymbol{M}\times(\boldsymbol{M}\times\boldsymbol{H}^{\text{eff}}), \tag{1.28}$$

where $\boldsymbol{H}^{\text{eff}}$ is the effective magnetic field acting on the structure, $\gamma = g|e|/(2m_e c)$ is the gyromagnetic ratio, g the Landé factor, and λ is a phenomenological damping parameter. Here, the term proportional to γ describes the precession of the magnetization around the axis defined by the direction of the magnetic effective field. On the other hand, the term proportional to λ describes the energy loss in real materials. Without it, the precession of the magnetization would describe a perpetual motion. This work is interested in studying the normal modes of oscillations on magnetic nanotubes. Therefore, the Landau-Lifshitz equation is studied without considering the damping parameter of the magnetization dynamics:

$$\frac{d}{dt}\boldsymbol{M}(\boldsymbol{r},t) = -\mu_0\gamma\boldsymbol{M}(\boldsymbol{r},t)\times\boldsymbol{H}^{\text{eff}}(\boldsymbol{r},t). \tag{1.29}$$

In Chapter 3, this equation is used to analyze the normal oscillation modes of spin waves over magnetic nanotubes with DMI and obtain the dispersion relation $f(\boldsymbol{k})$. In particular, because the DMI is produced by a spatial reversion symmetry breaking, this can lead to non-reciprocal phenomena like different frequencies [47–49] or attenuation lengths for spin waves traveling in opposite directions [50]. This work is focused on the frequency *non-reciprocity* of spin waves, measured by the frequency shift defined as:

$$\Delta f = f(\boldsymbol{k}) - f(-\boldsymbol{k}). \tag{1.30}$$

Chapter 2

Nucleation: Conical-Helix Textures

Consider a thin cylindrical shell of height L, external radius R, and internal radius $a = \beta R$. The shell consists of a ferromagnetic layer in contact with a heavy metal layer as depicted in Fig. 2.1, which induces an interfacial DMI. The heavy metal interface put as the outer or inner layer determines the sign of the DMI strength D. The Conical-Helix (CH) state has been shown to be a possible reversal mode in planar systems in the presence of DMI [11, 67]. The direct adaptation of this magnetization model to a cylindrical geometry with coordinates (ρ, ϕ, z) is given by the following normalized magnetization field:

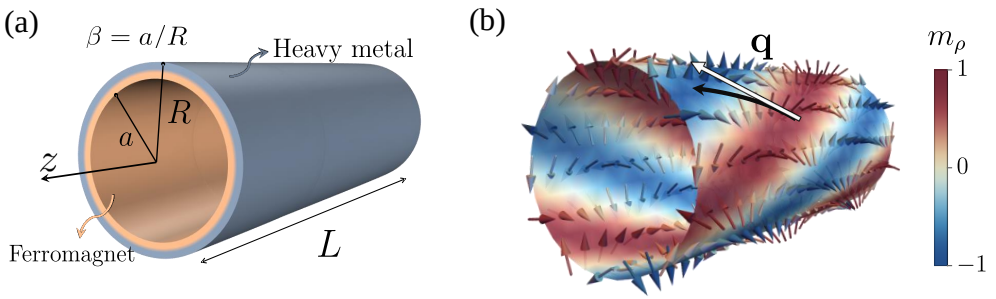

Figure 2.1: Schematic representation of the ferromagnetic nanotube with external radius R, internal radius a and height L (a). A heavy metal material in the interface induces the DM interaction. Conical-helix state with a mixed state of $z-$ and $\phi-$periodicity to form a net pseudo-pitch vector $\boldsymbol{q}$ (b).

$$\boldsymbol{m} = \cos(n\phi + q_z z)\sin\theta\hat{\boldsymbol{\rho}} + \sin(n\phi + q_z z)\sin\theta\hat{\boldsymbol{\phi}} + \cos\theta\hat{\boldsymbol{z}}, \tag{2.1}$$

where q_z describes the periodicity along the symmetry axis of the cylinder z, and the azimuthal index n indicates the periodicity along the coordinate ϕ,

which can only take integer values due to the tube edge-less boundary condition

$$\boldsymbol{m}(\phi) = \boldsymbol{m}(\phi + 2\pi). \tag{2.2}$$

The parameter θ is a fixed parameter along the system and describes the angle between the magnetization $\boldsymbol{m}$ and z, being $\theta = 0$ the fully saturated state. A pseudo pitch vector that characterizes the CH texture can be defined locally at the cylinder surface:

$$\boldsymbol{q} = \frac{n}{R}\hat{\boldsymbol{\phi}} + q_z\hat{\boldsymbol{z}}, \tag{2.3}$$

Fig. 2.2 shows one-wavelength-long helices with opposite vector spin chirality ($\boldsymbol{S}_i \times \boldsymbol{S}_j$) in planar and curved systems. In the planar system, the left-handed helices (a) are equivalent to the right-handed helices (b) and have the same (static) energy [67]. Suppose the same state is curved into a semi-circumference.

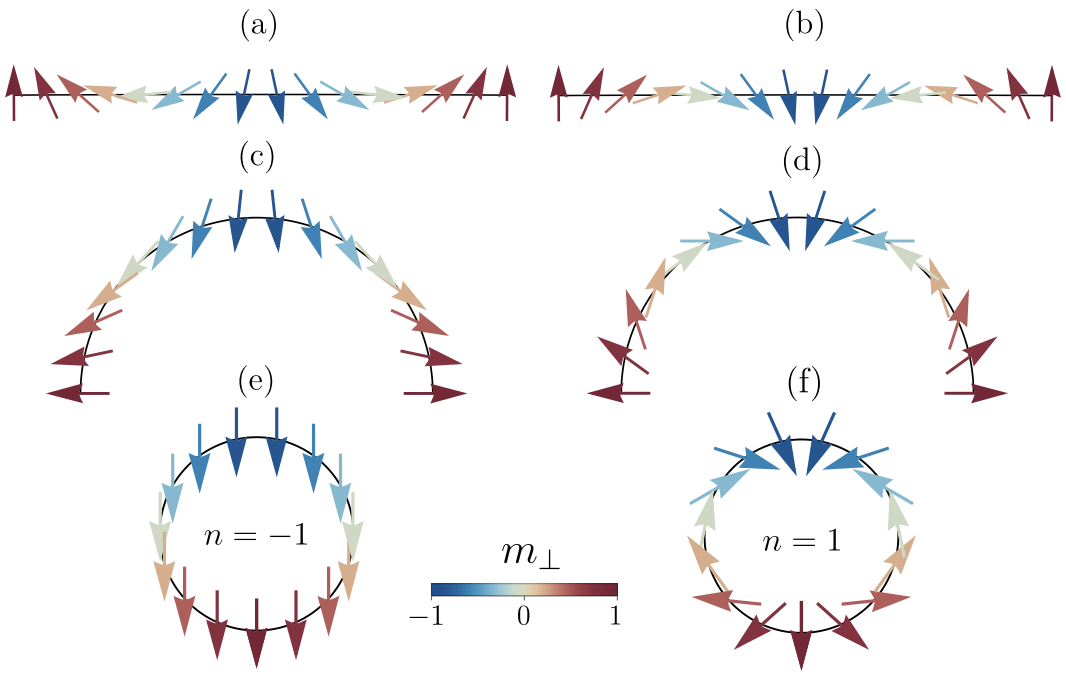

Figure 2.2: Cross-sectional schematic representation of one-wavelength-long CH states of different chirality in planar (a,b) and curved films (c-f). The color code represents the out-of-surface component of the magnetization. The helices in (a) left-handed and (b) right-handed planar systems, (c) left-handed and (d) right-handed curved semicircle, and circumferential system with (e) $n = -1$ and (f) $n = 1$ are illustrated.

In this case, the left-handed helix (c) has smaller angles between neighbor spins

than the right-handed helix (d) because the out-of-plane direction is not fixed due to the curvature. Accordingly, in a full circumference, the one-wavelength states with opposite chiralities are entirely different. Spins in the state with $n = -1$ (e) are collinear, and thus the whole system makes a uniform magnetization state. On the other hand, the state with $n = 1$ (f) is such that the neighboring spins make a large angle and thus have a significantly higher exchange cost. This simple analysis offers an intuitive way to understand the chirality induced by the curvature of the film.

2.1 Energy of the Conical-Helix Texture

In this section, each contribution to the energy of the Conical-Helix model is calculated using the magnetization model given by Eq. (2.1) to study its formation. For simplicity, the energy is normalized to the dimensionless quantity $\epsilon = E/(\mu_0 M_s^2 V)$, where $V = \pi(R^2 - a^2)L$ is the volume of the system. The total energy of the system is given by:

$$\epsilon = \epsilon_{ze} + \epsilon_{ex} + \epsilon_{d} + \epsilon_{an} + \epsilon_{dmi}, \tag{2.4}$$

where the interactions considered are respectively the Zeeman coupling with an external magnetic field (ϵ_{ze}), the exchange coupling (ϵ_{ex}), the dipolar coupling (ϵ_{d}), a perpendicular uniaxial anisotropy (ϵ_{an}) and the interfacial DMI (ϵ_{dmi}). A uniform magnetic field is applied along the nanotube axis's direction ($\hat{z}$). After integration (Eq. (1.9)), the energy asociated with this field is given by:

$$\epsilon_{ze} = -\frac{H}{M_s}\cos\theta. \tag{2.5}$$

The integrals calculated in the following section are valid for $n \neq 0$ because the special case $n = 0$ results in the Hegdehog (Hg) or Curling (C) reversal modes, which are analyzed separately (see Appendix C).

2.1.1 Exchange Energy

The exchange energy is calculated using Eq. (1.13). In cylindrical coordinates:

$$(\nabla m_i)^2 = \left(\frac{1}{\rho}\frac{\partial m_i}{\partial \phi}\right)^2 + \left(\frac{\partial m_i}{\partial z}\right)^2, \tag{2.6}$$

where m_i denotes each Cartesian coordinate. The CH magnetization (2.1) can be written in Cartesian coordinates as

$$\boldsymbol{m} = \cos((n+1)\phi + q_z z)\sin\theta\hat{\boldsymbol{x}} + \sin((n+1)\phi + q_z z)\sin\theta\hat{\boldsymbol{y}} + \cos\theta\hat{\boldsymbol{z}}, \tag{2.7}$$

so the dimensionless exchange energy results in:

$$\begin{aligned}\epsilon_{\text{ex}} =& \frac{A}{\mu_0 M_s^2 V}\iiint_V \frac{\sin^2\theta\left(n^2+2n+\rho^2 q_z^2+1\right)}{\rho^2}dV \\ =& \frac{A}{\mu_0 M_s^2}\left(q_z^2 + 2(1+n)^2\frac{\ln 1/\beta}{R^2(1-\beta^2)}\right)\sin^2\theta.\end{aligned} \tag{2.8}$$

The exchange energy term is minimized at values $(n, q_z) = (-1, 0)$, which correspond to the uniform magnetization mode—the state at which every spin is collinear (see Fig. 2.2 (e)).

2.1.2 Anisotropy

It has been found that the heavy metal coupling to the ferromagnetic film can produce an interfacial perpendicular anisotropy [69, 70]. As in the DMI case, this perpendicular direction is radial. According to Eq. (1.16),

$$E_{\text{an}} = -\iiint_V K_{\text{u}}(\hat{\boldsymbol{\rho}}\cdot\boldsymbol{m})^2 dV. \tag{2.9}$$

Finally, we get,

$$\epsilon_{\text{an}} = -\frac{K_{\text{u}}}{2\mu_0 M_s^2}\sin^2\theta. \tag{2.10}$$

2.1.3 Dipolar Energy

The whole calculation is done for the conical-helix model in Appendix A. Section 1.2.3.1 discussed that the dipolar energy favors magnetic structures

that minimize the appearance of bound magnetic charges. Consider the dipolar energy as a local interaction [33] that favors in-plane magnetization components—a hard axis radial anisotropy:

$$\epsilon_{\mathrm{d}} = -\frac{1}{\mu_0 M_{\mathrm{s}}^2 V} \iiint K_{\mathrm{d}} (\boldsymbol{m} \cdot \hat{\boldsymbol{\rho}})^2 dV. \tag{2.11}$$

To obtain the value of the effective anisotropy constant K_{d}, consider a uniform magnetization along the nanotube $\boldsymbol{m} = \sin\theta\hat{\boldsymbol{x}} + \cos\theta\hat{\boldsymbol{z}} = \sin\theta(\cos\phi\hat{\boldsymbol{\rho}} - \sin\phi\hat{\boldsymbol{\phi}}) + \cos\theta\hat{\boldsymbol{z}}$. The dipolar energy is given by [44]

$$\epsilon_{\mathrm{d}}^{\mathrm{u}} = \frac{N_x}{2}\sin^2\theta + \frac{N_z}{2}\cos^2\theta. \tag{2.12}$$

Using Eq. (2.11), the uniform magnetization texture dipolar energy results in

$$\epsilon_{\mathrm{d}}^{\mathrm{u}} = -\frac{K_{\mathrm{d}}}{2\mu_0 M_{\mathrm{s}}^2}\sin^2\theta. \tag{2.13}$$

The demagnetizing factors are constrained by the condition $2N_x + N_z = 1$. Also, for large aspect nanotubes $L \gg R$, $N_z \approx 0$ and therefore $N_x \approx 1/2$. Comparing equations (2.12) and (2.13) allows us to obtain the effective anisotropy constant that approximates the dipolar interaction:

$$K_{\mathrm{d}} = -\frac{\mu_0 M_{\mathrm{s}}^2}{2}. \tag{2.14}$$

Inserting (2.14) into (2.11):

$$\epsilon_{\mathrm{d}} = \frac{1}{2V}\int (\boldsymbol{m} \cdot \hat{\boldsymbol{\rho}})^2 dV. \tag{2.15}$$

Even though this notion of local anisotropy approximation for the nonlocal dipolar coupling was derived for a uniform magnetization, it can be used to analyze different magnetic textures. In Appendix A, the local approximation of the dipolar coupling is compared with the full dipolar form of Eq. (1.21). For the conical-helix model, it is obtained

$$\epsilon_{\mathrm{d}} = \frac{1}{2}\sin^2\theta. \tag{2.16}$$

Note that the combined effect of the dipolar and the volume-averaged surface anisotropy energy results in an effective anisotropy constant

$$K_{\text{eff}} = K_{\text{u}} - \frac{\mu_0 M_{\text{s}}^2}{2} = \frac{\mu_0 M_{\text{s}}^2}{2}(Q-1), \tag{2.17}$$

where $Q = 2K_{\text{u}}/\mu_0 M_{\text{s}}^2$ is called the *quality factor* and characterizes the balance between the dipolar and anisotropy interactions. When $Q = 0$, the system exhibits no radial anisotropy, and only dipolar interaction (shape anisotropy) appears. When $Q = 1$, the radial and shape anisotropies are compensated, and the system does not prefer either the out-of-plane ($\hat{\boldsymbol{\rho}}$) or the in-plane magnetization direction.

2.1.4 DMI Energy

The interfacial DMI energy is given by Eq. (1.24). In a ferromagnetic nanotube covered with a heavy-metal layer, as depicted in Fig. 2.3(a), the normal vector to the interface is $\hat{\boldsymbol{\rho}}$. The energy is then given by [71]:

$$E_{\text{dmi}} = \iiint_V D\hat{\boldsymbol{\rho}} \cdot (\boldsymbol{m}(\nabla \cdot \boldsymbol{m}) - (\boldsymbol{m} \cdot \nabla)\boldsymbol{m}) dV. \tag{2.18}$$

In cylindrical coordinates, the first term is computed as

$$\begin{aligned}(\hat{\boldsymbol{\rho}} \cdot \boldsymbol{m})(\nabla \cdot \boldsymbol{m}) =& m_\rho \left(\frac{1}{\rho}\frac{\partial \rho m_\rho}{\partial \rho} + \frac{1}{\rho}\frac{\partial m_\phi}{\partial \phi} + \frac{\partial m_z}{\partial z} \right) \\ =& \frac{1}{\rho}(n+1)\sin^2(\theta)\cos^2(n\phi + q_z z),\end{aligned} \tag{2.19}$$

while the second term is

$$\begin{aligned}\hat{\boldsymbol{\rho}} \cdot (\boldsymbol{m} \cdot \nabla)\boldsymbol{m} &= \hat{\boldsymbol{\rho}} \cdot \left(m_\rho \frac{\partial}{\partial \rho} + \frac{m_\phi}{\rho}\frac{\partial}{\partial \phi} + m_z \frac{\partial}{\partial z} \right)\boldsymbol{m} \\ &= \hat{\boldsymbol{\rho}} \cdot \left(\frac{m_\phi}{\rho}\frac{\partial m_\rho}{\partial \phi}\hat{\boldsymbol{\rho}} + \frac{m_\phi^2}{\rho}\frac{\partial \hat{\boldsymbol{\phi}}}{\partial \phi} + m_z \frac{\partial m_\rho}{\partial z}\hat{\boldsymbol{\rho}} \right) \\ &= \frac{m_\phi}{\rho}\frac{\partial m_\rho}{\partial \phi} - \frac{m_\phi^2}{\rho} + m_z \frac{\partial m_\rho}{\partial z} \\ &= -\frac{1}{\rho}(n+1)\sin^2(\theta)\sin^2(n\phi + q_z z) - q_z \sin(\theta)\cos(\theta)\sin(n\phi + q_z z),\end{aligned}$$

where $\partial_\phi \hat{\boldsymbol{\phi}} = -\hat{\boldsymbol{\rho}}$ is used and the terms perpendicular to $\hat{\boldsymbol{\rho}}$ have been omitted. The normalized DMI energy results in

$$\epsilon_{\text{dmi}} = \frac{2D(1+n)}{\mu_0 M_s^2 R(1+\beta)} \sin^2\theta. \tag{2.20}$$

The DMI term has a linear dependence on n. As expected, this interaction favors the formation of helical textures, with the handedness that depends on the sign of the DMI strength (D).

2.2 Nucleation Field

The total energy of the conical-helix mode magnetization given by Eq. (2.4) is

$$\epsilon^{\text{ch}} = \left(\frac{1-Q}{4} + \frac{A}{\mu_0 M_s^2}\left(q_z^2 + \frac{2(n+1)^2 \ln 1/\beta}{R^2(1-\beta^2)}\right) + \frac{2D(n+1)}{\mu_0 M_s^2 R(1+\beta)}\right)\sin^2\theta - \frac{H}{M_s}\cos\theta \tag{2.21}$$

The nucleation field H_n is obtained using this energy by solving Eq. (1.27) for variable H, which results in

$$H_n^{\text{ch}} = \frac{(Q-1)M_s}{2} - \frac{4D(n+1)}{\mu_0 M_s R(1-\beta)} - \frac{2A}{\mu_0 M_s}\left(q_z^2 + \frac{2(n+1)^2 \ln 1/\beta}{R^2(1-\beta^2)}\right). \tag{2.22}$$

Note that the energy can be written in terms of the nucleation field as

$$\epsilon^{\text{ch}} = -\frac{H_n^{\text{ch}}}{2M_s}\sin^2\theta - \frac{H}{M_s}\cos\theta. \tag{2.23}$$

A consequence of the former equation implies the parameters (n, q_z) that maximize the nucleation field are the same that minimize the energy. Therefore, the reversal mode from the saturated state simultaneously describes the magnetic ground state. The nucleation field (2.22) is maximized when $q_z = 0$ and $n = n_{\text{nt}}$, where

$$n_{\text{nt}} = \left\lfloor -1 - \frac{D}{2A}\frac{R(1-\beta)}{\ln 1/\beta} \right\rceil, \tag{2.24}$$

where $\lfloor x \rceil$ denotes the approximation of x to the nearest integer, which arises from the periodic boundary condition (2.2) resulting in the quantization of the

wavelength of the helix in the nanotube:

$$\lambda_{\mathrm{nt}} = \frac{2\pi R}{|n_{\mathrm{nt}}|}. \tag{2.25}$$

From Eq. (2.3), the pitch vector in the nanotube is given by

$$\boldsymbol{q}_{\mathrm{nt}} = \frac{1}{R}\left[-1 - \frac{D}{2A}\frac{R(1-\beta)}{\ln 1/\beta}\right]\hat{\boldsymbol{\phi}}. \tag{2.26}$$

Note that in the ultrathin ($\beta \to 1$) and planar limit ($R \to \infty$) the pitch vector converges to $q_0 = D/(2A)$ agreeing with the reported value [11, 67]. Notably, the handedness of the helix can be associated with the sign of n_{nt} and, therefore, with the sign of D. Similar to the planar case, the interfacial DMI creates helix textures and induces a pitch vector $\boldsymbol{q}$ perpendicular to the initial saturation field [67, 72].

2.3 Micromagnetic Simulations

Micromagnetic simulations were performed using the finite element micromagnetic package Finmag [73]. A nanotube of radius $R = 15$ nm, shell thickness $d = 3$ nm and height $L = 0.5$ μm was analyzed. Simulations considered exchange, dipolar, and Zeeman interactions. In addition, radial anisotropy and cylindrical interfacial DMI were implemented in a forked version of the code [74]. Standard magnetic parameters for Permalloy ($Ni_{80}Fe_{20}$) have been used: $M_s = 796$ kA/m and $A = 13$ pJ/m. The simulations consisted of a field reduction process from an axially saturated state, using field steps of 5 mT, starting from a sufficiently large field, down to zero field, or even lower, depending on the case [71]. Local energy minimum configurations were found at every field step by relaxing the system using the Landau-Lifshitz-Gilbert equation with a substantially large damping value and removing the precessional dynamics. Visualizations were done using the PyVista library [75]. The right panels of Fig. 2.3 (a-g) show the states obtained for simulated tubes with $Q = 0.9$ and several DMI values $D = -6, -5, -4, \ldots, 6$ mJ/m^2 at the start of the reversion from the saturated state along the nanotube's axis—the states just below the nucleation field value $H \lesssim H_{\mathrm{n}}$. The reversal modes are denoted S_n where $n = -4, -3, \ldots, 2$ is the azimuthal periodicity described in

the CH model. The left scheme of each panel shows the cross-sectional view of the corresponding n–mode graphed with the magnetization model for the conical-helix Eq. (2.1).

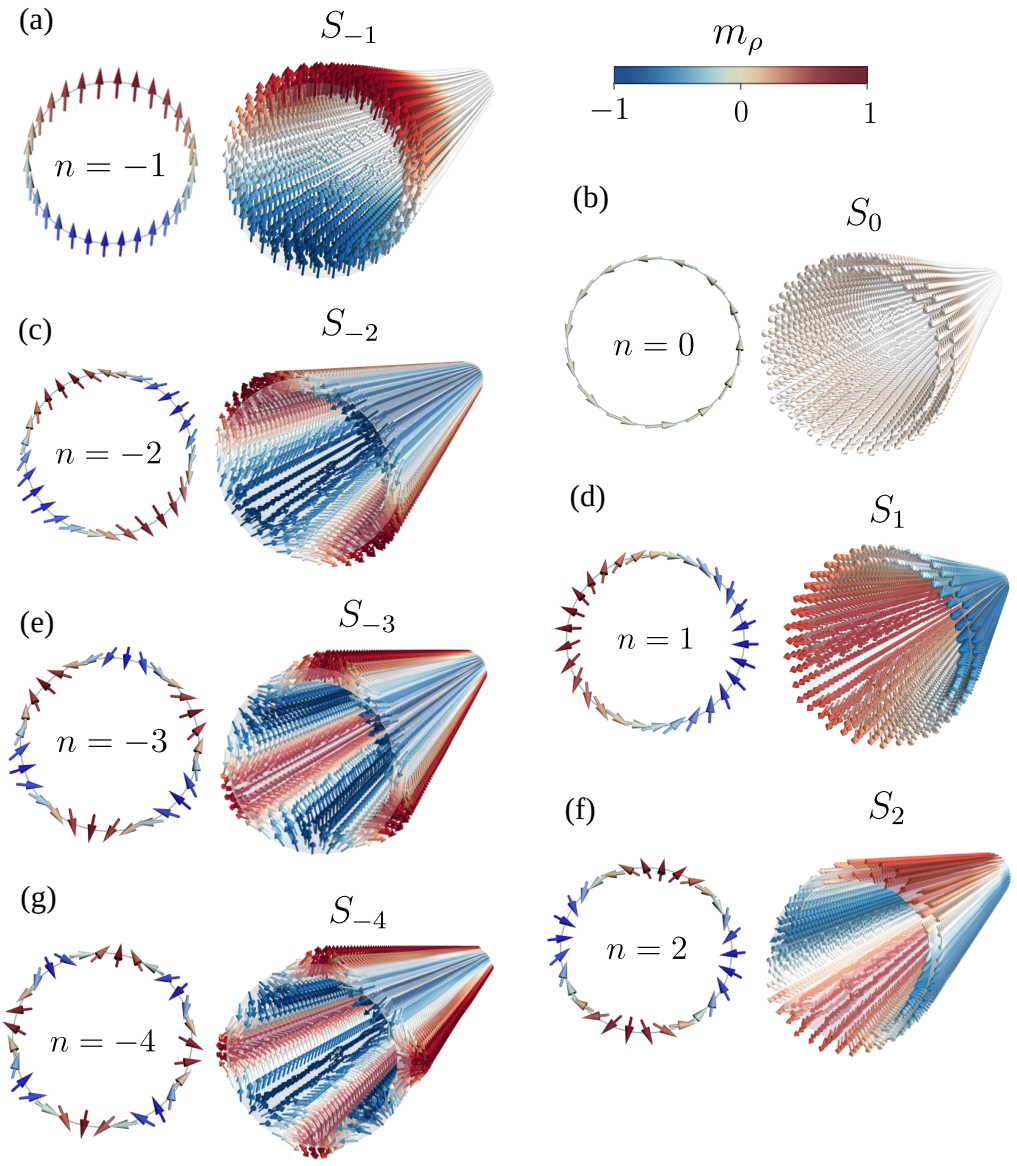

Figure 2.3: Cross-section of the CH states obtained using the model Eq. (2.1) for different values of the azimuthal index n and their corresponding state obtained in the micromagnetic simulations denoted by S_n for a quality factor $Q = 0.9$ and different values of the DMI strength as shown in Fig. 2.4.

2.4 Texture Formation

Permalloy parameters are used in this section for calculations; $M_s = 796$ kA/m and $A = 13$ pJ/m. The thickness of the film is $R - a = 3$ nm. With the approximation of the nonlocal dipolar interaction as a local anisotropy, the nucleation field of the conical-helix mode given in Eq. (2.22) does not depend on the nanotube's height L. The DMI strength D, and the geometrical parameters, R and β, determine the pitch vector that characterizes the higher nucleation field and the lower energy solution within the CH ansatz (Eq. (2.26)). Although it does not depend on the radial anisotropy, this parameter becomes important when the nucleation field of the CH is compared with other reversal modes: the curling (C) mode (C.1b) or the hedgehog (Hg) mode (C.1c). The graphs in this section show the favorable reversion mode for different sets of magnetic parameters. This is obtained analitically by comparing the CH nucleation field (2.22) evaluated at the parameters that maximize the nucleation field (2.24) with the nucleation fields of the C and Hg modes (Eqns (C.3a) and (C.3b)).

Fig. 2.4 shows the reversal mode of the nanotubes as a function of the DMI strength D and the quality factor Q for a radius $R = 15$ nm. Different values of n are obtained and represented in different colors in the diagram from $n = -4$ to $n = 2$, including the Curling and Hedgehog states. Blue diamonds denoted by S_n represent the conical-helix n-state obtained in Finmag simulated nanotubes of 15-nm radius with different D values [71]. The reversion mode obtained in the simulations and the cross-sectional views of the conical-helix magnetization states are depicted in Fig. 2.3. As the absolute value of D increases, the value of n that maximizes the nucleation field given by Eq. (2.24) increases, and therefore the length of the helix λ_{nt} decreases. The chirality of the helix formed depends on the sign of D. Positive values $D > 0$ favor helices with $n < 0$ and negative values $D > 0$ favor helices with $n > 0$. However, opposite-chirality helices are not energetically equivalent. This can be seen from the graph, as it is not symmetric with respect to $D = 0$. See, for instance, the simulated reversion for $D = 4$ mJ/m^2 occurs through the S_{-3} mode depicted in Fig. 2.3 (f). On the other hand, for $D = -4$ mJ/m^2 the reversion occurs through the S_1 helix shown in Fig. 2.3 (b). This asymmetry between positive and negative values of D occurs because the curved surface of the nanotube produces an exchange energy difference between opposite rotation states, as discussed in Fig. 2.2.

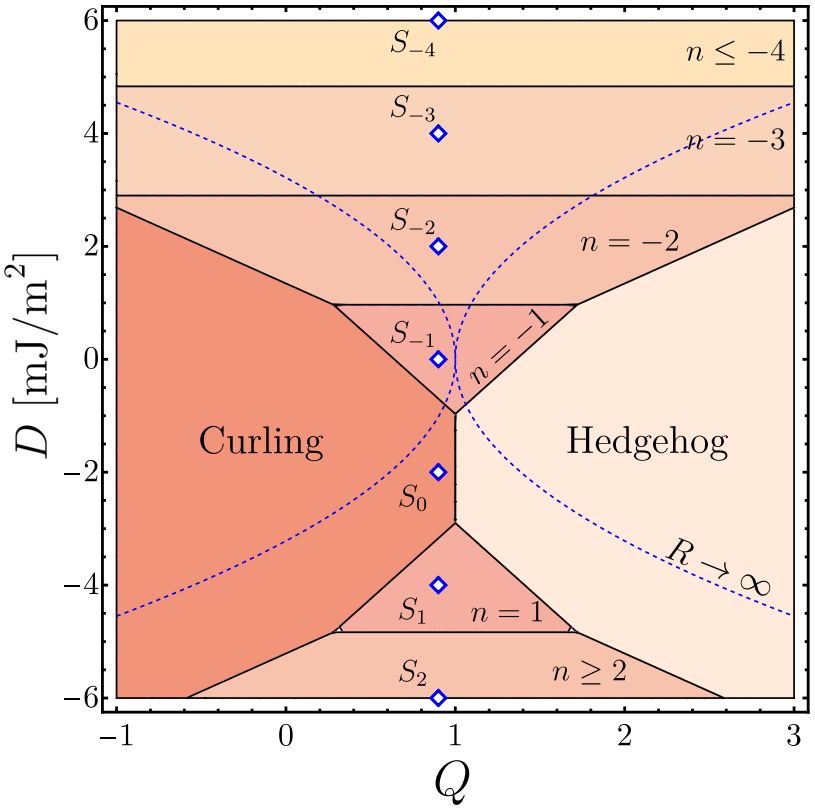

Figure 2.4: Reversal mode as a function of the DMI strength D and the quality factor Q of a nanotube of radius $R = 15$ nm and thickness $R - a = 3$ nm. Blue dashed lines represent the interface between the in-plane and out-of-plane reversal modes (C or Hg mode) and the CH reversal mode in a planar magnetic film [67, 72] that coincides with the asymptotic solution of the nanotube in the limit $R \to \infty$. Blue diamonds represent simulated nanotubes shown in Fig. 2.3.

The radial anisotropy controls a tendency in the system to reverse through either the C reversal mode, in-plane magnetization, or the Hg reversal mode, out-of-plane magnetization. Consequently, for larger absolute values of Q, these two states cover a wider range of D values, meaning that a bigger value of the DMI strength is needed to achieve a CH state. As discussed in Section 2.1.3, the quality factor Q measures the competition between the anisotropy and the dipolar interactions. For $Q > 1$—high anisotropy value—the anisotropy dominates over the dipolar interaction, and therefore, the Hg state is favored over the C state. In contrast, $Q < 1$ means that the dipolar interaction dominates over the radial anisotropy; hence, the C state is preferred. The further the quality factor is from the value $Q = 1$, the bigger the value of DMI strength needed for the reversal through the CH state is. Moreover, far from this value, the Curling and Hedgehog states cover a wider range of D values. For example,

at $Q = 0$ the states $n = \pm 1$ are not available, and at a DMI strength value of $D = 0$ and $D = -4$ mJ/m^2 (values at which the system nucleates through the states $n = -1$ and $n = -1$ respectively at $Q = 0.9$), reverses through the C mode. In other words, the boundary between Curling/Hedgehog states and conical-helix states with $n \neq 0$ defines the critical DMI strength value $D_{\text{crit}}(Q)$ at which the nucleation occurs through the CH state. The blue dashed line represents the critical value D_{crit} for the case of a planar magnetic film [67] and it is symmetric concerning $D = 0$. This coincides with the critical value for the nanotube in the limit $R \to \infty$, thus providing a way to confirm the solution of this diagram asymptotically.

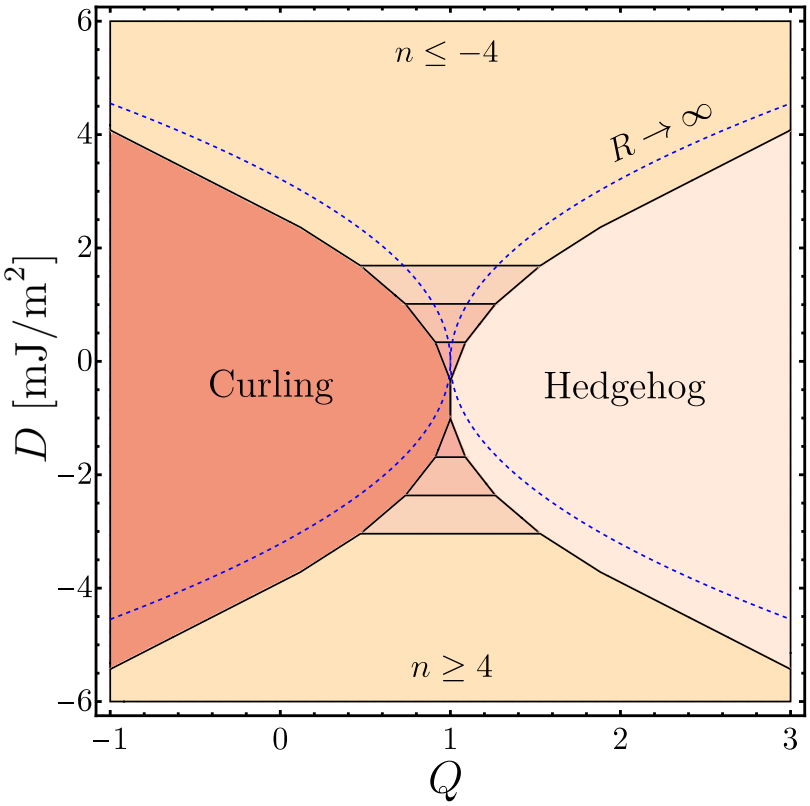

Figure 2.5: Reversal mode as a function of D and Q of a nanotube of radius $R = 40$ nm. Blue dashed lines represent the interface between the in-plane and out-of-plane reversal modes (curling or hedgehog mode) and the conical-helix reversal mode (CH mode) in a planar magnetic film [67]. Blue diamonds are simulated points nanotubes shown in Fig. 2.3.

Fig 2.5 shows a similar Q vs D diagram for a nanotube of radius $R = 40$ nm. The main difference is that the asymmetry with respect to $D = 0$ is less noticeable than in the former diagram. Bigger radius nanotubes have a less

curved surface and the energy difference between opposite-chirality CH states is lower. In this case, the critical value D_{crit} shows a clear tendency to the planar critical value represented in the blue dotted line. Compared to the $R = 15$ nm nanotube, more states can be obtained within the same range of D values. The larger the radius, the lower the range of D values each n-state covers, until the limit $R \to \infty$ where the azimuthal index converges to a continuum of values, as in the case of the planar system.

The reversal modes for different radii, DMI strength D, and a quality factor $Q = 0.9$ are shown in Fig. 2.6. Blue diamonds represent the same nanotubes simulated in Fig. 2.4. As evidenced in the previous figures, the Hg mode only appears for anisotropy values such that $Q > 1$. Therefore, the C mode is favored for any given R and D values. As was already discussed, for fixed radius and quality factor, larger absolute values of D originate CH textures with smaller wavelengths λ_{nt}, resembling the behavior of planar magnetic films [67]. For larger radii, the number of states obtained in a certain range of D values increases as the number of values of the wavelength (given by Eq. (2.25)) that can fit through the perimeter is larger. This diagram also shows the asymmetry concerning $D = 0$ caused by the energy difference of opposed chirality helices. This difference is most notable at small radii (large curvature) and converges to a symmetric diagram at the large radius limit. The $n = \pm 1$ reversions only occur at small radii because at $Q = 0.9$ the C mode is favored. Unlike the planar system where the pitch vector of the helix is approximately $q_0 = D/(2A)$ and thus lower values of the DMI produce a larger wavelength value $\lambda_0 = 2\pi/q_0$, the larger possible wavelength that can be formed in the nanotube along the azimuthal direction due to the periodicity is the full perimeter $\lambda = 2\pi R$, namely the state $n = \pm 1$. Therefore, larger wavelength helices can be found in a nanotube with a larger radius, but these large-λ_{nt} states can only occur when the dipolar and the anisotropy interactions are well compensated ($Q \approx 1$). For bigger values $Q > 1$ (smaller values $Q < 1$), large areas of in-plane (out-of-plane) magnetization are not allowed. Consequently, the C and Hg modes become more favorable than the large wavelength states.

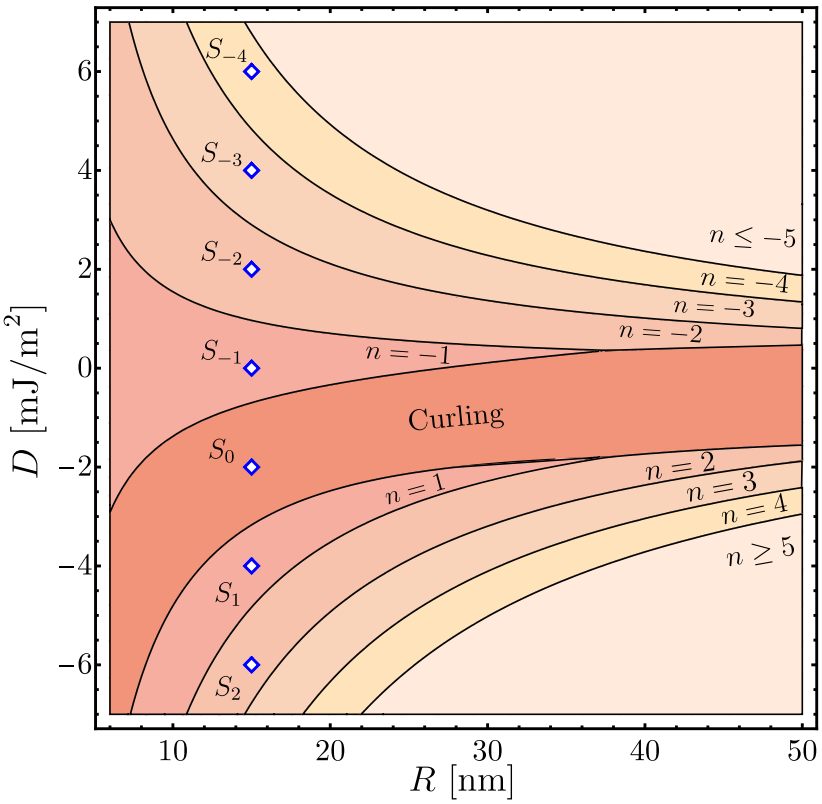

Figure 2.6: Reversal mode as a function of the DMI strength D and the nanotube radius R for a quality factor $Q = 0.9$. Blue diamonds correspond to the simulated points.

Chapter 3

Spin Wave Dynamics

The effect of the interfacial DMI on the frequency of spin waves on nanotubes has not yet been reported. The Landau-Lifshitz (LL) Eq. (1.29) models the time dependence of the magnetization. To study the normal modes that propagate along the nanotube's surface, consider small perturbations from an equilibrium magnetization

$$\boldsymbol{M}(t) = \boldsymbol{M}_0 + \delta\boldsymbol{m}(t) \tag{3.1a}$$

$$\boldsymbol{H}^{\text{eff}}(t) = \boldsymbol{H}_0^{\text{eff}}(\boldsymbol{M}_0) + \delta\boldsymbol{h}(t). \tag{3.1b}$$

Here $\boldsymbol{H}_0^{\text{eff}}$ is the effective field produced by the equilibrium magnetization $\boldsymbol{M}_0$, and $\delta\boldsymbol{h}$ is the effective field produced by the magnetization deviations $\delta\boldsymbol{m}$. To describe these perturbations, a plane wave ansatz can be used $\delta\boldsymbol{m}(t) \sim \exp[i(\boldsymbol{k}\cdot\boldsymbol{r} - \omega t)]$. As in the previous chapter, the basic assumption is that the magnetization along the radial direction is constant for very thin nanotubes. Therefore, oscillations propagate only in the z and ϕ directions [48, 49]:

$$\delta\boldsymbol{m}(t) = \boldsymbol{m}e^{i(k_z z + l\phi - \omega t)} \tag{3.2a}$$

$$\delta\boldsymbol{h}(t) = \boldsymbol{h}e^{i(k_z z + l\phi - \omega t)}, \tag{3.2b}$$

Considering Eq. (1.29) up to first order in deviations, the Linearized Landau Lifshitz equation is obtained:

$$\omega\boldsymbol{m} = i\gamma\mu_0(\boldsymbol{H}_0^{\text{eff}} \times \boldsymbol{m} + \boldsymbol{h} \times \boldsymbol{M}_0). \tag{3.3}$$

This problem can be solved if the equilibrium magnetization $\boldsymbol{M}_0$ is known. Depending on the angle at which an external magnetic field is applied concerning the nanotube axis, the most commonly studied equilibrium magnetizations on nanotubes are a saturated state along the axis or a vortex-like magnetization along the nanotube. The well-known curling reversal mode [51] gives a continuous parameterization between both states [44, 76]:

$$\boldsymbol{M}_0 = M_s(C\sin\theta_0\hat{\boldsymbol{\phi}} + \cos\theta_0\hat{\boldsymbol{z}}) = M_s\hat{\boldsymbol{z}}', \tag{3.4}$$

where the angle θ_0 controls the orientation $\hat{\boldsymbol{z}}'$ of the magnetization as shown in Fig. 3.1. The parameter C determines a right-handed ($C = 1$) or left-handed ($C = -1$) curling state. Note that the equilibrium magnetization implicitly depends on the azimuthal angle ϕ, so this orientation is not uniform; rather, it is defined locally at the location on the nanotube surface. For ($\theta_0 = 0$), the magnetization is saturated along the symmetry axis, and at ($\theta_0 = \pi/2$), it forms a vortex-like state. Condition (1.5b) must be satisfied to have a correct equilibrium state.

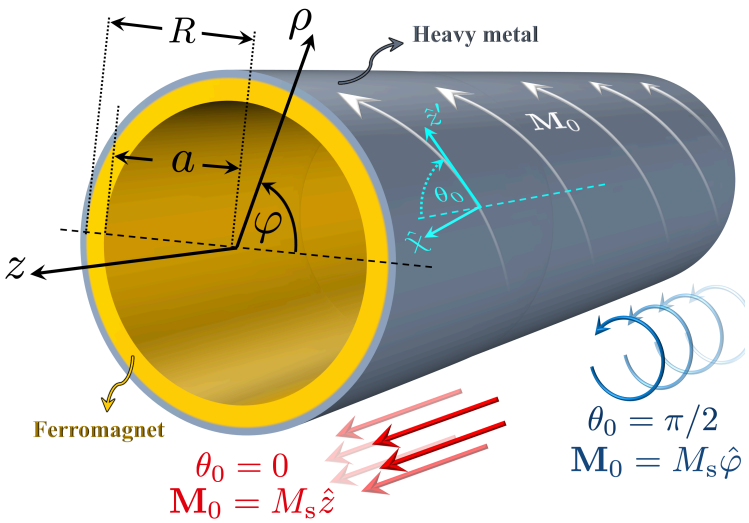

Figure 3.1: An infinitely long ferromagnetic nanotube of external (internal) radius R (a) covered with a heavy-metal layer is considered. The equilibrium magnetization of the system describes a curling state: it points along the $\hat{\boldsymbol{z}}'$ direction, which forms an angle θ_0 with the nanotube's symmetry axis $\hat{\boldsymbol{z}}$.

Consequently, $\boldsymbol{H}_0^{\text{eff}} = H_0^{\text{eff}}\hat{\boldsymbol{z}}'$ and thus, from Eq. (3.3), the Fourier coefficients $\boldsymbol{m}$ do not have a component along the direction of the equilibrium magnetization. Then, it is convenient to describe the dynamic magnetization through a local reference system defined by the plane orthogonal to $\boldsymbol{M}_0$. This is quickly done

by noting that it has no radial component $\boldsymbol{\rho} \cdot \boldsymbol{M}_0 = 0$, so a third orthogonal vector can be constructed as $\hat{\boldsymbol{\chi}} = \hat{\boldsymbol{\rho}} \times \hat{z}'$ to obtain

$$\hat{\boldsymbol{\chi}} = -\cos\theta_0 \hat{\boldsymbol{\phi}} + C \sin\theta_0 \hat{z} \tag{3.5a}$$

$$\hat{\boldsymbol{\rho}} = \hat{\boldsymbol{\rho}} \tag{3.5b}$$

$$\hat{z}' = C \sin\theta_0 \hat{\boldsymbol{\phi}} + \cos\theta_0 \hat{z} \tag{3.5c}$$

The set of right-handed ordered vectors $(\hat{\boldsymbol{\chi}}, \hat{\boldsymbol{\rho}}, \hat{z}')$ define a more convenient new basis B. Fourier coefficients of Eq. (3.2a) are given in this basis by $\boldsymbol{m} = m_\chi \hat{\boldsymbol{\chi}} + m_\rho \hat{\boldsymbol{\rho}}$. The linearized LL Eq. (3.3) results in

$$\omega m_\chi = i\gamma\mu_0(-H_0^{\text{eff}} m_\rho + M_\text{s} h_\rho) \tag{3.6a}$$

$$\omega m_\rho = i\gamma\mu_0(H_0^{\text{eff}} m_\chi - M_\text{s} h_\chi). \tag{3.6b}$$

Because the effective fields are obtained as linear operations over the magnetization as shown in Section 1.2, the dynamic field can be written as a linear combination of the dynamic magnetization [48]

$$\boldsymbol{h} = -\boldsymbol{\Lambda} \cdot \boldsymbol{m}, \qquad h_i = -\Lambda_{ij} m_j, \tag{3.7}$$

where $\boldsymbol{\Lambda}$ is a dynamic tensor that includes terms of the different energy contributions. As a result, equations (3.6) form a set of coupled equations that can be written in matrix form as follows:

$$\omega \begin{pmatrix} m_\chi \\ m_\rho \end{pmatrix} = i\gamma\mu_0 M_\text{s} \boldsymbol{T} \begin{pmatrix} m_\chi \\ m_\rho \end{pmatrix}, \tag{3.8}$$

with

$$\boldsymbol{T} = \begin{pmatrix} -\Lambda_{\rho\chi} & -\Lambda_{\rho\rho} - \frac{H_0^{\text{eff}}}{M_\text{s}} \\ \frac{H_0^{\text{eff}}}{M_\text{s}} + \Lambda_{\chi\chi} & \Lambda_{\chi\rho} \end{pmatrix}. \tag{3.9}$$

Solving this eigenvalue problem will yield the angular frequency ω. The dispersion relation is then obtained by $f = \omega/(2\pi)$:

$$f = \frac{i\gamma\mu_0 M_\text{s}}{4\pi}\left((\Lambda_{\chi\rho} - \Lambda_{\rho\chi}) \pm \sqrt{(\Lambda_{\rho\chi} + \Lambda_{\chi\rho})^2 - 4\left(\frac{H_0^{\text{eff}}}{M_\text{s}} + \Lambda_{\rho\rho}\right)\left(\frac{H_0^{\text{eff}}}{M_\text{s}} + \Lambda_{\chi\chi}\right)}\right). \tag{3.10}$$

Here the two eigenvalues obtained are related by $f_1(k_z, l) = -f_2(-k_z, -l)$, and the physical solution is chosen to be the positive one. In the following section, the dispersion relation is obtained by calculating the equilibrium magnetic field H_0^{eff} and the total dynamic tensor $\boldsymbol{\Lambda}$.

3.1 Effective Fields and Dynamic Tensors

In calculating the effective fields, a dependence on the radial coordinate ρ may appear through derivatives (even though the magnetization does not depend on it) because of curvature (e.g., (1.15)). To avoid this problem, in what follows, the averaged value of each field over the nanotube's radius is considered in the calculations:

$$\boldsymbol{H} \equiv \langle \boldsymbol{H} \rangle = \frac{1}{R(1-\beta)} \int \boldsymbol{H} d\rho, \tag{3.11}$$

where the integrals go from $a = \beta R$ to R. The equilibrium and the dynamic effective magnetic fields, considering every interaction, are

$$\boldsymbol{H}_0^{\text{eff}} = \boldsymbol{H}_{\text{ze}} + \boldsymbol{H}_{\text{ex}}^0 + \boldsymbol{H}_{\text{u}}^0 + \boldsymbol{H}_{\text{d}}^0 + \boldsymbol{H}_{\text{dmi}}^0, \tag{3.12a}$$

$$\delta\boldsymbol{h} = -(\boldsymbol{\Lambda}_{\text{ex}} + \boldsymbol{\Lambda}_{\text{u}} + \boldsymbol{\Lambda}_{\text{d}} + \boldsymbol{\Lambda}_{\text{dmi}})\, \boldsymbol{m} e^{i(k_z z + l\phi - \omega t)}. \tag{3.12b}$$

3.1.1 Exchange interaction

The exchange effective field is obtained by taking the mean value of the expression (1.15) across the thickness. The Laplacian of a vector field $\boldsymbol{v}$ without radial dependence is given by

$$\nabla^2 \boldsymbol{v} = \left(\nabla^2 v_x\right) \hat{\boldsymbol{x}} + \left(\nabla^2 v_y\right) \hat{\boldsymbol{y}} + \left(\nabla^2 v_z\right) \hat{\boldsymbol{z}} \tag{3.13a}$$

$$\nabla^2 = \frac{1}{\rho^2} \frac{\partial^2}{\partial \phi^2} + \frac{\partial^2}{\partial z^2} \tag{3.13b}$$

Using the basis definition (3.5), $\boldsymbol{M}_0$ in Cartesian coordinates is given by

$$\boldsymbol{M}_0 = M_{\text{s}}(-C \sin\theta_0 \sin\phi \hat{\boldsymbol{x}} + C \sin\theta_0 \cos\phi \hat{\boldsymbol{y}} + \cos\theta_0 \hat{\boldsymbol{z}}), \tag{3.14}$$

so that

$$\nabla^2 \boldsymbol{M}_0 = \left(-\frac{C M_{\text{s}}}{\rho^2} \sin\theta_0 \hat{\boldsymbol{\phi}}\right), \tag{3.15}$$

and the exchange effective field is:

$$\begin{aligned}\boldsymbol{H}^0_{\mathrm{ex}} &= \frac{1}{R(1-\beta)}\int l^2_{\mathrm{ex}}\left(-\frac{M_{\mathrm{s}}}{\rho^2}C\sin\theta_0\hat{\boldsymbol{\phi}}\right)d\rho \\ &= -H_{\mathrm{ex}}C\sin\theta_0\hat{\boldsymbol{\phi}} \\ &= H_{\mathrm{ex}}C\sin\theta_0(\cos\theta_0\hat{\boldsymbol{\chi}} - \sin\theta_0\hat{\boldsymbol{z}}'),\end{aligned} \tag{3.16}$$

where $H_{\mathrm{ex}} = M_{\mathrm{s}}l^2_{\mathrm{ex}}/\beta R^2$. Accordingly, the dynamic magnetization fourier coefficients of Eq. (3.2a) in Cartesian coordinates are

$$\boldsymbol{m} = (m_\rho\cos\phi + m_\chi\cos\theta_0\sin\phi)\hat{\boldsymbol{x}} + (m_\rho\sin\phi - m_\chi\cos\theta_0\cos\phi)\hat{\boldsymbol{y}} + m_\chi C\sin\theta_0\hat{\boldsymbol{z}}. \tag{3.17}$$

Once more, using equations (3.13) and (3.17) and returning to the basis B, the relevant dynamic effective field components are given by:

$$\delta h_{\mathrm{ex},\boxtimes} = \frac{1}{R(1-\beta)}\int l^2_{\mathrm{ex}}(\nabla^2\delta\boldsymbol{m})_\chi d\rho \tag{3.18a}$$

$$\delta h_{\mathrm{ex},\boxtimes} = \frac{1}{R(1-\beta)}\int l^2_{\mathrm{ex}}(\nabla^2\delta\boldsymbol{m})_\rho d\rho, \tag{3.18b}$$

so that the Fourier coefficients of Eq. (3.2b) are

$$h_{\mathrm{ex},\boxtimes} = -\frac{l^2_{\mathrm{ex}}}{\beta R^2}\left(m_\chi\left(\cos^2\theta_0 + l^2 + \beta R^2k_z^2\right) + 2ilm_\rho\cos\theta_0\right) \tag{3.19a}$$

$$h_{\mathrm{ex},\boxtimes} = -\frac{l^2_{\mathrm{ex}}}{\beta R^2}\left(m_\rho\left(1 + l^2 + \beta R^2k_z^2\right) - 2ilm_\chi\cos\theta_0\right), \tag{3.19b}$$

and consequently, the dynamic exchange tensor defined by (3.7) is given by:

$$\boldsymbol{\Lambda}_{\mathrm{ex}} = \frac{H_{\mathrm{ex}}}{M_{\mathrm{s}}}\begin{pmatrix}\cos^2\theta_0 + l^2 + \beta R^2k_z^2 & 2il\cos\theta_0 \\ -2il\cos\theta_0 & 1 + l^2 + \beta R^2k_z^2\end{pmatrix}. \tag{3.20}$$

3.1.2 Anisotropy

A uniaxial anisotropy perpendicular to the surface is considered. The anisotropy effective field is defined by Eq. (1.17), where $\hat{\boldsymbol{n}} = \hat{\boldsymbol{\rho}}$ is the radial direction perpendicular to the outer surface. The equilibrium contribution

vanishes because $\hat{\boldsymbol{\rho}} \cdot \boldsymbol{M}_0$. On the other hand,

$$\begin{aligned}\delta \boldsymbol{h}_{\mathrm{u}} &= \frac{1}{R(1-\beta)} \int \frac{2K_{\mathrm{u}}}{\mu_0 M_{\mathrm{s}}} (\hat{\boldsymbol{\rho}} \cdot \delta \boldsymbol{m}) \hat{\boldsymbol{\rho}} d\rho \\ &= H_{\mathrm{u}} m_\rho e^{i(k_z z + l\phi - \omega t)} \hat{\boldsymbol{\rho}}, \end{aligned} \tag{3.21}$$

so the dynamic tensor is

$$\boldsymbol{\Lambda}_{\mathrm{u}} = \frac{H_{\mathrm{u}}}{M_{\mathrm{s}}} \begin{pmatrix} 0 & 0 \\ 0 & 1 \end{pmatrix}. \tag{3.22}$$

The radial anisotropy produces a dynamic effective field proportional to the radial component of the dynamic magnetization $\sim \delta m_\rho$, which explains the fact that there is only one non-zero component of the dynamic tensor $\boldsymbol{\Lambda}_{\mathrm{u}}$.

3.1.3 Dipolar interaction

In the absence of electric currents, the dipolar magnetic field is $\boldsymbol{H}_{\mathrm{d}} = -\nabla\Phi$, where the magnetostatic potential Φ is given as (1.20). The equilibrium effective field calculation is straightforward. Note that $\nabla \cdot \boldsymbol{M}_0 = 0$. Additionally, for an infinitely long nanotube, there are only lateral surfaces and $\hat{\boldsymbol{\rho}} \cdot \boldsymbol{M}_0 = 0$ in the surfaces. Consequently, $\boldsymbol{H}_{\mathrm{d}}^0 = 0$ and only the dynamic magnetization produces a dipolar field:

$$\nabla \cdot \delta \boldsymbol{m} = \left(\frac{m_\rho}{\rho} + i \left(-\frac{l \cos\theta_0}{\rho} + k_z C \sin\theta_0 \right) m_\chi \right) e^{i(k_z z + l\phi - \omega t)} \tag{3.23a}$$

$$\boldsymbol{n} \cdot \delta \boldsymbol{m} = \pm m_\rho e^{i(k_z z + l\phi - \omega t)} \tag{3.23b}$$

Integrals can be solved considering the following identity [1]:

$$\int_{-\infty}^{\infty} dz' \frac{e^{i\boldsymbol{k}\cdot\boldsymbol{r}'}}{|\boldsymbol{r} - \boldsymbol{r}'|} = 2K_0(|k_z||\boldsymbol{\rho} - \boldsymbol{\rho}'|) e^{i\boldsymbol{k}\cdot\boldsymbol{r}}, \tag{3.24}$$

so considering $\boldsymbol{k} = k_z \hat{\boldsymbol{z}}$ allows to integrate coordinate z. The volume term is then given by

$$\Phi_V = -\Omega_1 m_\rho e^{i(k_z z + l\phi - \omega t)} + (il \cos\theta_0 \Omega_1 - ikC \sin\theta_0 \Omega_2) m_\chi e^{i(k_z z + l\phi - \omega t)}, \tag{3.25}$$

[1] This can be otbained from Problem 14.7.10 of reference [77].

where Ω_1, Ω_2 are integrals on coordinates ρ, ϕ defined as,

$$\Omega_1 = \frac{1}{2\pi} \iint K_0(|k_z|[\rho^2 + \rho'^2 - 2\rho\rho' \cos(\phi' - \phi))] e^{il(\phi' - \phi)} d\rho' d\phi' \tag{3.26a}$$

$$\Omega_2 = \frac{1}{2\pi} \iint \rho' K_0(|k_z|[\rho^2 + \rho'^2 - 2\rho\rho' \cos(\phi' - \phi))] e^{il(\phi' - \phi)} d\rho' d\phi'. \tag{3.26b}$$

Here, the ρ' integrals go from βR to R and the ϕ' integrals go from 0 to 2π. In order to simplify these expressions, consider a 2π-periodic function $F(\phi)$. Note that,

$$\frac{\partial}{\partial \phi} \int_0^{2\pi} F(\phi' - \phi) d\phi' = \frac{\partial}{\partial \phi} \int_\phi^{2\pi + \phi} F(\phi') d\phi' = F(2\pi) - F(0) = 0. \tag{3.27}$$

Therefore, Ω_1, Ω_2 do not depend on variable ϕ and $\phi = 0$ can be considered. The following function is now defined:

$$G(\rho, \rho', \phi') = \frac{e^{il\phi'}}{2\pi R(1 - \beta)} K_0\Big(|k_z| \sqrt{\rho^2 + \rho'^2 - 2\rho\rho' \cos\phi'}\Big), \tag{3.28}$$

so the former integrals can be written as

$$\Omega_1(\rho) = R(1 - \beta) \iint G(\rho, \rho', \phi') d\rho' d\phi', \tag{3.29a}$$

$$\Omega_2(\rho) = R(1 - \beta) \iint \rho' G(\rho, \rho', \phi') d\rho' d\phi'. \tag{3.29b}$$

On the other hand, the superficial term is:

$$\Phi_S = \Omega_3 m_\rho e^{i(k_z z + l\phi - \omega t)}. \tag{3.30}$$

By similar manipulations, the surface integral Ω_3 is given by

$$\Omega_3(\rho) = R(1 - \beta) \int (RG(\rho, R, \phi') - \beta RG(\rho, \beta R, \phi')) d\phi' \tag{3.31a}$$

$$= R(1 - \beta) \iint \partial_{\rho'} \rho' G(\rho, \rho', \phi') d\rho' d\phi'. \tag{3.31b}$$

The total magnetic potential is then given by

$$\begin{aligned}\Phi =&((-\Omega_1+\Omega_3)m_\rho + i(l\cos\theta_0\Omega_1 - k_z C\sin\theta_0\Omega_2)m_\chi)e^{i(k_z z+l\phi-\omega t)}. &(3.32a)\\ =&R(1-\beta)\iint \rho'\partial_{\rho'}G(\rho,\rho',\phi')d\rho' d\phi' m_\rho e^{i(k_z z+l\phi-\omega t)}\\ &+R(1-\beta)\iint i(l\cos\theta_0 - k_z C\sin\theta_0\rho')G(\rho,\rho',\phi')d\rho' d\phi' m_\chi e^{i(k_z z+l\phi-\omega t)} &(3.32b)\end{aligned}$$

Thus, the dipolar dynamic field is found using Eq. (3.11):

$$\delta\boldsymbol{h}_{\mathrm{d}} = \frac{1}{R(1-\beta)}\int(-\nabla\Phi)d\rho \tag{3.33}$$

where,

$$\begin{aligned}-\nabla\Phi =& -\left(\frac{\partial\Phi}{\partial\rho}\hat{\boldsymbol{\rho}} + \frac{1}{\rho}\frac{\partial\Phi}{\partial\phi}\hat{\boldsymbol{\phi}} + \frac{\partial\Phi}{\partial z}\hat{\boldsymbol{z}}\right)\\ =&\left(\frac{1}{\rho}\frac{\partial\Phi}{\partial\phi}\cos\theta_0 - \frac{\partial\Phi}{\partial z}C\sin\theta_0\right)\hat{\boldsymbol{\chi}} - \frac{\partial\Phi}{\partial\rho}\hat{\boldsymbol{\rho}} - \left(\frac{\partial\Phi}{\partial z}\cos\theta_0 + \frac{1}{\rho}\frac{\partial\Phi}{\partial\phi}C\sin\theta_0\right)\hat{\boldsymbol{z}}'\\ =&\left(\frac{il}{\rho}\cos\theta_0 - ik_z C\sin\theta_0\right)\Phi\hat{\boldsymbol{\chi}} - \frac{\partial\Phi}{\partial\rho}\hat{\boldsymbol{\rho}} - \left(ik_z\cos\theta_0 + \frac{il}{\rho}C\sin\theta_0\right)\Phi\hat{\boldsymbol{z}}'. &(3.34)\end{aligned}$$

By Eq. (3.12b), this results in the following dynamic tensor components:

$$\Lambda_{\mathrm{d},\chi\chi} = \iiint(l\cos\theta_0 - k_z C\sin\theta_0\rho)(l\cos\theta_0 - k_z C\sin\theta_0\rho')\frac{1}{\rho}G_0(\rho,\rho',\phi')d\rho d\rho' d\phi' \tag{3.35a}$$

$$\Lambda_{\mathrm{d},\chi\rho} = -i\iiint(l\cos\theta_0 - k_z C\sin\theta_0\rho)\frac{\rho'}{\rho}G_1(\rho',\rho,\phi')d\rho d\rho' d\phi' \tag{3.35b}$$

$$\Lambda_{\mathrm{d},\rho\chi} = i\iiint(l\cos\theta_0 - k_z C\sin\theta_0\rho')G_1(\rho,\rho',\phi')d\rho d\rho' d\phi' \tag{3.35c}$$

$$\Lambda_{\mathrm{d},\rho\rho} = \iiint\rho' G_2(\rho,\rho',\phi')d\rho d\rho' d\phi', \tag{3.35d}$$

where it has been defined,

$$G_0(\rho,\rho',\phi') = \frac{e^{il\phi'}}{2\pi R(1-\beta)}K_0\left(|k_z|\sqrt{\rho^2+\rho'^2-2\rho\rho'\cos\phi'}\right) \tag{3.36a}$$

$$G_1(\rho,\rho',\phi') = \partial_\rho G_0(\rho,\rho',\phi') \tag{3.36b}$$

$$G_2(\rho,\rho',\phi') = \partial_{\rho\rho'}G_0(\rho,\rho',\phi'). \tag{3.36c}$$

The thin film approximation allows for yet another consideration. Integration with limits $\beta R \to R$ can be well approximated as proportional to the function evaluated on its midpoint $R_\mathrm{m} = R(1+\beta)/2$:

$$\int_{\beta R}^{R} F(\rho) d\rho = R(1-\beta) F(R_\mathrm{m}). \tag{3.37}$$

This way, the threefold integration on (3.35) is simplified to a 1-dimensional integration:

$$\Lambda_{\mathrm{d},\chi\chi} = (l\cos\theta_0 - k_z R_\mathrm{m} C \sin\theta_0)^2 I_0 \tag{3.38a}$$

$$\Lambda_{\mathrm{d},\chi\rho} = -\Lambda_{\mathrm{d},\boxtimes\boxtimes} = -i(l\cos\theta_0 - k_z R_\mathrm{m} C \sin\theta_0) I_1 \tag{3.38b}$$

$$\Lambda_{d,\rho\rho} = I_2 \tag{3.38c}$$

where,

$$I_0 = R^2(1-\beta)^2 \int \frac{1}{R_\mathrm{m}} G_0(R_\mathrm{m}, R_\mathrm{m}, \phi') d\phi' \tag{3.39a}$$

$$I_1 = R^2(1-\beta)^2 \int G_1(R_\mathrm{m}, R_\mathrm{m}, \phi') d\phi' \tag{3.39b}$$

$$I_2 = R^2(1-\beta)^2 \int R_\mathrm{m} G_2(R_\mathrm{m}, R_\mathrm{m}, \phi') d\phi'. \tag{3.39c}$$

Integrals I_1, I_2, I_3 can only be solved numerically. A first order expansion in k_z allows for analytical expressions. For $l = 0$:

$$I_0(l=0) = \frac{4(1-\beta)}{(1+\beta)^2}\left(\gamma + \ln\left(\frac{|k|R}{2}\right)\right) \tag{3.40a}$$

$$I_1(l=0) = -\left(\frac{1-\beta}{1+\beta}\right) \tag{3.40b}$$

$$I_2(l=0) = 1, \tag{3.40c}$$

while for $l \neq 0$:

$$I_0 = \left(\frac{1-\beta}{1+\beta}\right)\frac{1}{|l|} \tag{3.41a}$$

$$I_1 = 0 \tag{3.41b}$$

$$I_2 = \frac{1}{1+\beta}\left(\left(\frac{1+\beta}{2}\right)^{|l|} + \beta\left(\frac{2\beta}{1+\beta}\right)^{|l|}\right). \tag{3.41c}$$

The explicit calculations are shown in Appendix D.

3.1.4 DM interaction

The interfacial DMI field is obtained by taking the mean value of expression (1.25). Noting that

$$-\left(\hat{\boldsymbol{\rho}}(\nabla\cdot\boldsymbol{M}_0)-\nabla(\boldsymbol{M}_0\cdot\hat{\boldsymbol{\rho}})+\frac{M_{0\phi}\hat{\boldsymbol{\phi}}}{\rho}\right)=-\frac{M_\mathrm{s}}{\rho}C\sin\theta_0\hat{\boldsymbol{\phi}}, \tag{3.42}$$

so that

$$\boldsymbol{H}_\mathrm{dmi}=-H_\mathrm{dmi}C\sin\theta_0\hat{\boldsymbol{\phi}}=H_\mathrm{dmi}C\sin\theta_0(\cos\theta_0\hat{\boldsymbol{\chi}}-C\sin\theta_0\hat{\boldsymbol{z}}') \tag{3.43}$$

where $H_\mathrm{dmi}=2D\ln(1/\beta)/(\mu_0 M_\mathrm{s}R(1-\beta))$. The dynamic field is

$$\boldsymbol{h}_\mathrm{dmi}=\frac{1}{R(1-\beta)}\int\frac{2D}{\mu_0 M_\mathrm{s}}\left(\hat{\boldsymbol{\rho}}(\nabla\cdot\boldsymbol{m})-\nabla(\boldsymbol{m}\cdot\hat{\boldsymbol{\rho}})+\frac{m_\phi}{\rho}\hat{\boldsymbol{\phi}}\right) \tag{3.44}$$

then results in,

$$\boldsymbol{\Lambda}_\mathrm{dmi}=\frac{H_\mathrm{dmi}}{M_\mathrm{s}}\begin{pmatrix}\cos^2\theta_0 & i\left(l\cos\theta_0-k_zC\sin\theta_0\frac{R(1-\beta)}{\ln(1/\beta)}\right)\\ -i\left(l\cos\theta_0-k_zC\sin\theta_0\frac{R(1-\beta)}{\ln(1/\beta)}\right) & 1\end{pmatrix} \tag{3.45}$$

3.2 Nonreciprocity

To satisfy the equilibrium condition (1.5b) the effective field of the equilibrium magnetization is such that $\boldsymbol{H}_0^\mathrm{eff}\cdot\hat{\boldsymbol{\chi}}=0$. Therefore, an external field is applied in the direction $\boldsymbol{H}_\mathrm{ze}=H_\mathrm{ze}(\sin\theta_\mathrm{ze}\hat{\boldsymbol{\phi}}+\cos\theta_\mathrm{ze}\hat{\boldsymbol{z}})$ and the equilibrium condition results in:

$$(H_\mathrm{ex}+H_\mathrm{dmi})\cos\theta_0 C\sin\theta_0+H_\mathrm{ze}\sin(\theta_0-\theta_\mathrm{ze})=0. \tag{3.46}$$

With the results obtained in the former section, it can be noted that $\Lambda_{\chi\rho}=-\Lambda_{\rho\chi}$. Therefore, the spin-wave frequency given by Eq. 3.10 results in:

$$f=\frac{\gamma\mu_0 M_\mathrm{s}}{2\pi}\left(i\Lambda_{\chi\rho}+\sqrt{\left(\frac{H_0^\mathrm{eff}}{M_\mathrm{s}}+\Lambda_{\rho\rho}\right)\left(\frac{H_0^\mathrm{eff}}{M_\mathrm{s}}+\Lambda_{\chi\chi}\right)}\right). \tag{3.47}$$

In nanotubes, the frequency shift (1.30) is given by $\Delta f(k_z, l) = f(k_z, l) - f(-k_z, -l)$. Because only non-diagonal terms on the Λ tensor are odd functions of parameters k_z, l, the frequency shift results in:

$$\Delta f = \frac{i\gamma\mu_0 M_s}{\pi}\Lambda_{\chi\rho}. \tag{3.48}$$

Depending on the angle of equilibrium magnetization θ_0, a difference in the frequency of counter-propagating waves is found. Explicitly, the frequency shift can be separated into terms proportional to the axial wave vector (k_z) and azimuthal (l/R) wave vectors, $\Delta f = \Delta f_{k_z} + \Delta f_l$, where:

$$\Delta f_{k_z} = \frac{\mu_0 M_s \gamma}{\pi} k_z C \sin\theta_0 \left(\frac{2D}{\mu_0 M_s^2} - R_m I_1\right), \tag{3.49}$$

and

$$\Delta f_l = \frac{\mu_0 M_s \gamma}{\pi}\frac{l}{R}\cos\theta_0 \left(RI_1 - \frac{2D\ln(1/\beta)}{\mu_0 M_s^2(1-\beta)} - \frac{2l_{ex}^2}{\beta R}\right). \tag{3.50}$$

Here Δf_{k_z} and Δf_l quantify the non-reciprocity along the axial (z) and the azimuthal (ϕ) directions respectively. In Eqs. (3.49) and (3.49), it is noted that the dipolar, exchange, and DM interactions induce asymmetry in the spin-wave dispersion. In the absence of DMI, the frequency shift is generated only by the dipole-dipole and exchange interactions, in concordance with previous results [47, 48, 76].

3.3 Results

As in the previous chapter, Permalloy magnetic parameters are used for the calculations, namely $M_s = 796$ kA/m and an exchange constant $A = 13$ pJ/m. The gyromagnetic ratio is $\gamma = 175.929$ GHz/T. The external and internal radii of the nanotube are $R = 40$ nm and $a = 35$ nm respectively. The equations obtained in the previous sections allow for the analysis of the dynamics considering different equilibrium magnetizations from the saturated state along the nanotube's axis ($\theta_0 = 0$) to the vortex state ($\theta_0 = \pi/2$) and all intermediate states. Here, results are shown for the limiting cases of the saturated state and the right-handed vortex ($C = 1$) [78]. Zero radial anisotropy is considered $K_u = 0$.

3.4 Effects of the interfacial DMI

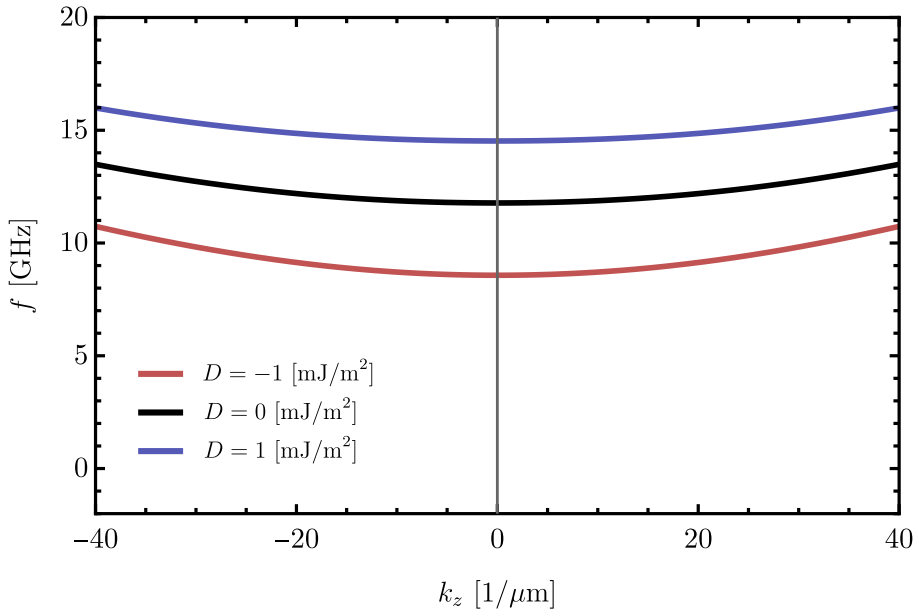

Figure 3.2: Spin-wave frequency of the nanotube in the saturated state ($\theta_0 = 0$) as equilibrium magnetization and an azimuthal index $l = 0$ as a function of the wave vector along the z direction for DMI strength values of $D = -1, 0, 1$ mJ/m^2 in red, black and blue respectively.

The spin-wave frequency in the saturated state ($\theta_0 = 0$) is calculated with a magnetic field of magnitude $\mu_0 H_{\text{ze}} = 130$ mT along the $\hat{z}$. Fig. 3.2 shows the $l = 0$ azimuthal mode spin-wave frequency as a function of the z-wave vector $f(k_z)$ for three different values of the DMI, namely $D = -1$ mJ/m^2 (red line), $D = 0$ mJ/m^2 (black line) and $D = 1$ mJ/m^2 (blue line). Spin waves propagating in the axial direction of the nanotube show reciprocal behavior because from Eq. (3.49), $\Delta f_k = 0$ at $\theta_0 = 0$. The influence of the DMI is to increase or decrease the energy of the system and therefore the frequency of the spin waves, depending on the sign of D. For $D > 0$ the frequency of the $l = 0$ state increases (blue line), while for $D < 0$ it decreases (red line). For the case of the vortex equilibrium state $\theta_0 = \pi/2$, an external magnetic field $\mu_0 H = 130$ mT $\hat{\boldsymbol{\phi}}$ direction is sufficient to stabilize it. The spin waves modes with $l = 0$ are shown in Fig. 3.3 as a function of the z-wave vector $f(k_z)$ for three values of the DMI: $D = -1, 0, 1$ mJ/m^2. The vortex state is known to have dipolar-induced nonreciprocity in the propagation of spin waves along the axial direction z

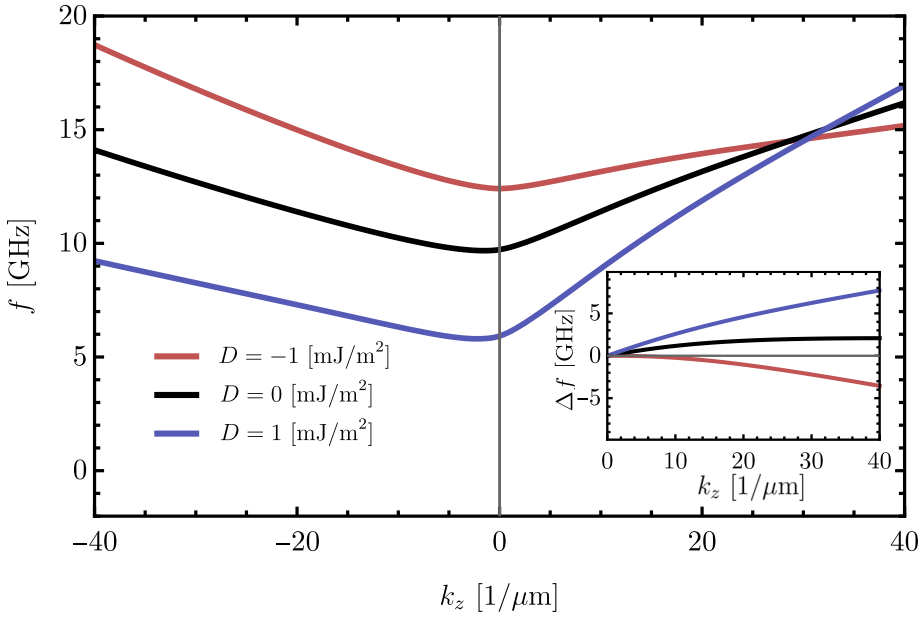

Figure 3.3: Spin-wave frequency in the vortex state ($\theta_0 = \pi/2$) and an azimuthal index $l = 0$ as a function of the wave vector along the z direction for $D = -1, 0, 1$ mJ/m^2. The inset shows the frequency shift for the same D values.

[34, 47–49, 76]. This is shown in the black curve, which is nonsymmetrical concerning $k_z = 0$ in contrast to the saturated case, and in the inset, where a positive frequency shift ($\Delta f > 0$) is found in the absence of DMI meaning that the propagating waves along the z direction have a higher frequency than those along the opposite direction $-z$. The DMI either reinforces this asymmetry, for $D > 0$ (blue line), or opposes it for $D < 0$ (red line). Thus, the nonreciprocity can switch for positive values of the DMI as shown by the negative values of Δf, causing the waves to propagate to the $-k_z$ direction to have a higher frequency.

The next azimuthal modes $l = 1$ (solid lines) and $l = -1$ (dashed lines) are shown for the saturated state $\theta_0 = 0$ in Fig. 3.4 and for the vortex state $\theta_0 = \pi/2$ in Fig. 3.5. The spin wave frequency is calculated for the same set of parameters. In the saturated state, the frequency of these modes is not the same because for $l \neq 0$ magnetic oscillations along the azimuthal direction occur, and counter-propagating spin waves along ϕ in the saturated state ($\theta_0 = 0$) show a nonreciprocal behavior because from Eq. (3.50), $\Delta f_l \neq 0$. The quantity Δf_l depends on the dipolar integral $I_1(k, l)$ and on the exchange length l_{ex}, therefore the nonreciprocity arises not only from the DM interaction but also from the dipolar and exchange interactions. Indeed, for $D = 0$ (black lines), both states

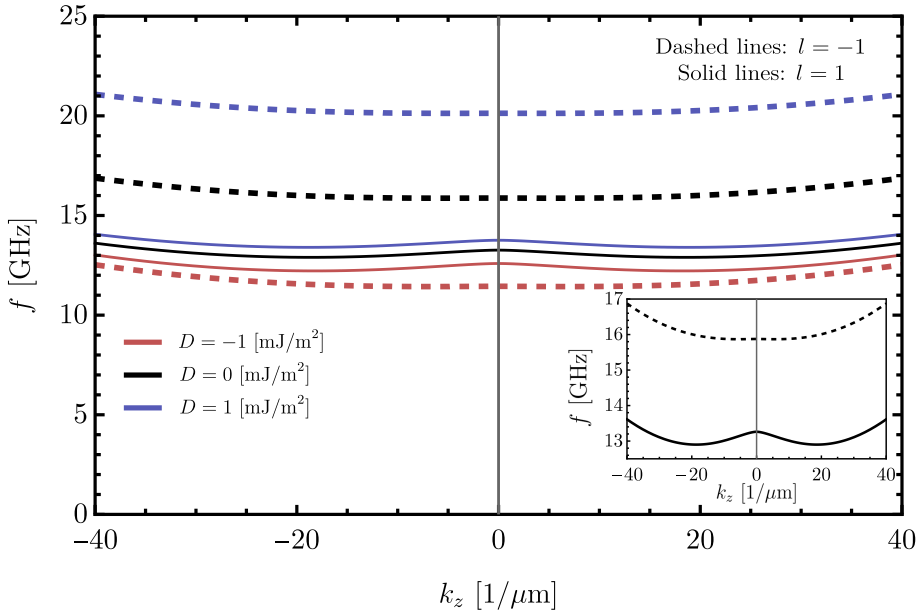

Figure 3.4: Spin-wave dispersion in the saturated state ($\theta_0 = 0$). Azimuthal modes $l = 1$ and $l = -1$ are shown in solid and dashed lines respectively. DMI strength values are again considered $D = -1, 0, 1$ mJ/m^2. The inset shows a zoom to a lower range of frequency values for the case $D = 0$.

show different frequencies and different dispersions. The effect of the dipolar interaction in nanotubes also produces interesting magnon dispersion curves. The inset of Fig. 3.4 shows a close-up of the magnon dispersion of the $D = 0$ case. The k_z dependence of the dipolar interaction through I_1 produces a change in the dispersion for opposite azimuthal chirality modes, even producing a negative group velocity zone in the $l = 1$ mode for $k_z \approx 0$. This effect is also present in the $l = -1$ mode, but is shown to be less relevant. As depicted in Fig. 3.5, for the vortex state $\theta_0 = \pi/2$ the $l = 1$ (solid lines) and $l = -1$ (dashed lines) modes are equal, as the frequency difference is quantified by $\Delta f_l \sim \cos\theta_0$. In the absence of DMI (black lines), the dipolar-induced nonreciprocity is much less relevant than in the $l = 0$ case, as evidenced in the inset. Again, the DMI effect is to cause a positive (negative) frequency shift $\Delta f > 0$ ($\Delta f < 0$) for $D > 0$ ($D < 0$).

The Δf_l frequency shift observed in the saturated state is better understood in a plot of the frequency as a function of the azimuthal index shown in Fig. 3.6. A value $k_z = 0$ is considered again for three different DMI strengths, namely $D = -1$ mJ/m^2 (red circles), $D = 0$ mJ/m^2 (black triangles) and $D = 1$ mJ/m^2

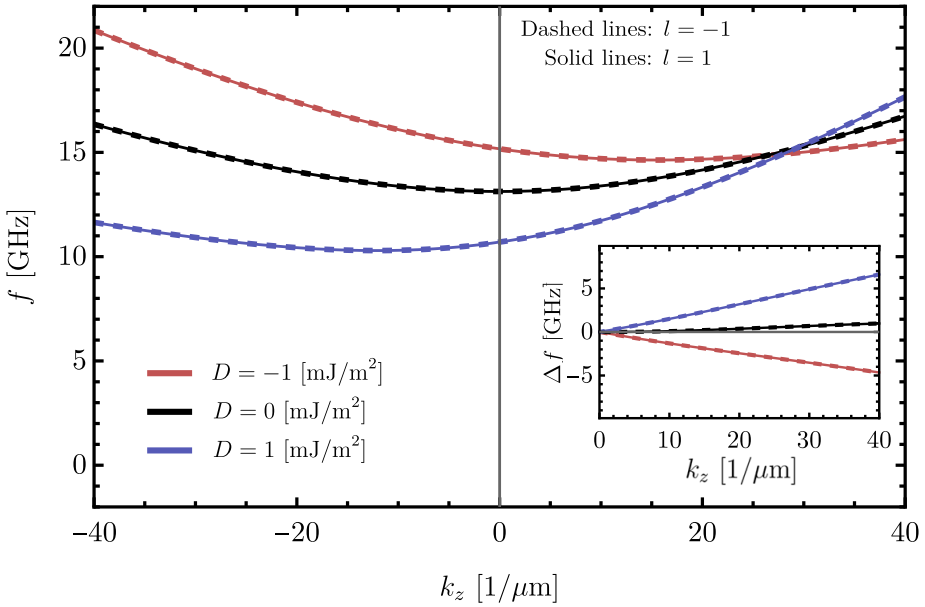

Figure 3.5: Spin-wave frequency in the vortex state ($\theta_0 = \pi/2$) of the $l = 1$ (solid lines) and $l = -1$ (dashed lines) modes as a function of the wave vector along the z direction for $D = -1, 0, 1$ mJ/m^2. The inset shows the frequency shift for the same D values.

(blue diamonds). As discussed in the previous figure, the plot for $D = 0$ already shows a dipolar- and exchange-induced nonreciprocity. The frequency shift is depicted in the inset of the figure and is shown to be negative, which means higher frequency values for negative l-values. Positive DMI values ($D > 0$) reinforce this nonreciprocity, causing a more negative frequency shift Δf, and negative values ($D < 0$) oppose it.

The dynamic magnetization profiles can be calculated as the eigenvector associated with the corresponding frequency eigenvalue in equation (3.8). A snapshot at $t = t_0$ of the cross-sectional view of the dynamic magnetization profiles of $l = -1, 0, 1$ modes is shown in Fig. 3.7. In each equilibrium state, the dynamic magnetization only has components along the directions perpendicular to $\hat{z}'$. In the vortex state, the dynamic magnetization has radial (ρ) and axial (z) components. The states $l = 1$, $l = 0$ and $l = -1$ are shown in Fig. 3.7 (a-c). The $l = \pm 1$ profiles represent the same oscillation but with a phase difference and thus have the same energy and frequency as discussed in the previous figures. On the other hand, in the saturated state, the dynamic magnetization has radial (ρ) and azimuthal (ϕ) components Fig. 3.7 (d-f). The $l =$

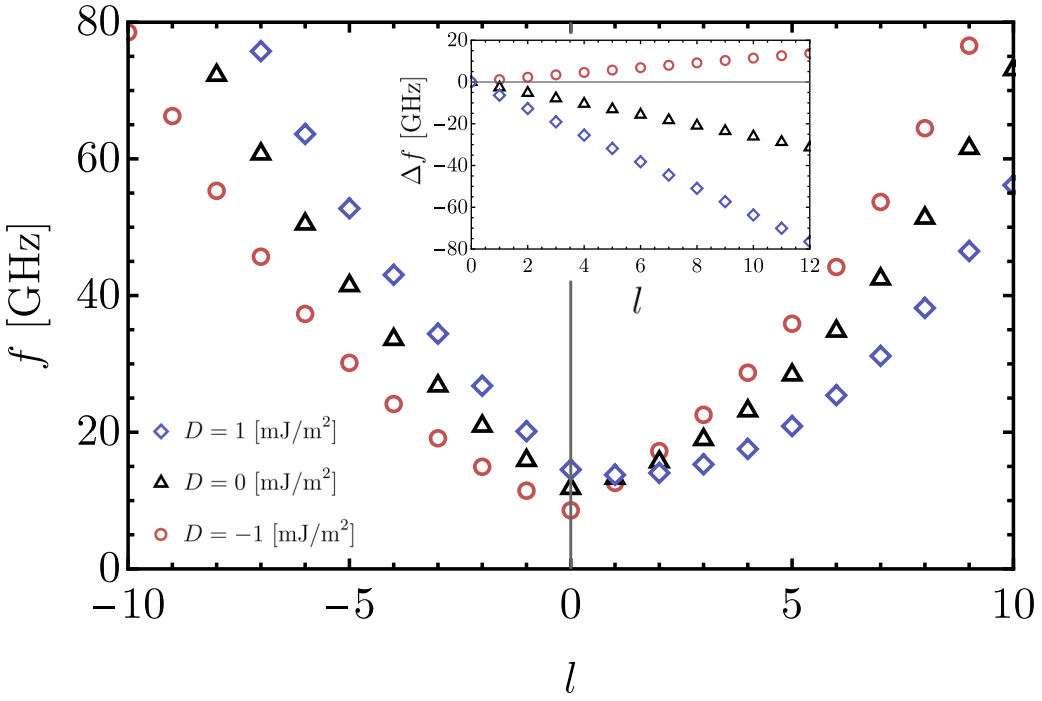

Figure 3.6: Spin-wave dispersion in the saturated state ($\theta_0 = 0$) as a function of the azimuthal index l for $k_z = 0$ for DMI strengths of $D = -1, 0, 1$ mJ/m^2 depicted in red, black and blue respectively. The inset shows the frequency shift Δf for these values of the DMI strength.

± 1 states have a different spatial distribution, which explains the difference in energy. The $l = 1$ state is similar to a uniform distribution, so the exchange cost is less than in the $l = -1$ mode. Due to the absence of radial anisotropy ($Q = 0$), the dipolar energy dominates, and the in-plane magnetization is favored over the out-of-plane in each case. Therefore, there is a smaller amplitude in the zones with radial magnetization than in those with in-surface magnetization. This is not the case for the $l = 0$ mode, where the amplitude is uniform along the perimeter in both cases $\theta_0 = 0$ and $\theta_0 = \pi/2$.

3.5 Effects of the radial anisotropy

To analyze the effect of the radial anisotropy on the spin-wave dispersion, the $l = 0$ excitation mode in the vortex equilibrium state is illustrated in Fig. 3.8 for three different values of the quality factor, namely $Q = 0$, $Q = 0.6$ and $Q = 1.1$. The values $D = -1$ mJ/m^2 and $D = 1$ mJ/m^2 are shown in the left and right diagrams respectively. Because the frequency shift Δf does not depend on K_u,

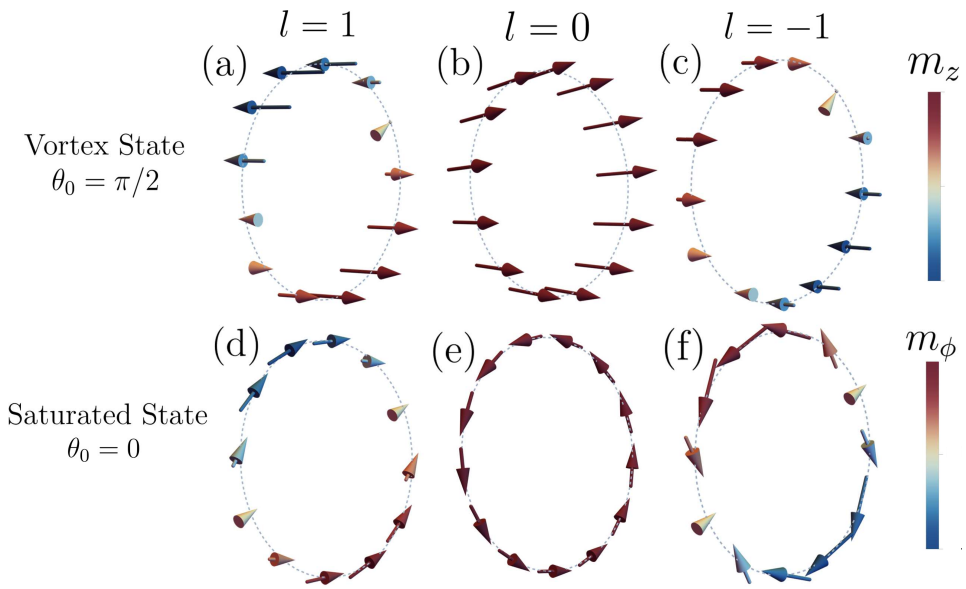

Figure 3.7: Cross-sectional view of the dynamic magnetization of modes $l = -1, 0, 1$ in the vortex state (a-c) and the saturated state (d-f) colored by the m_z and m_ϕ components. Values $Q = 0$ and $D = 0$ are considered.

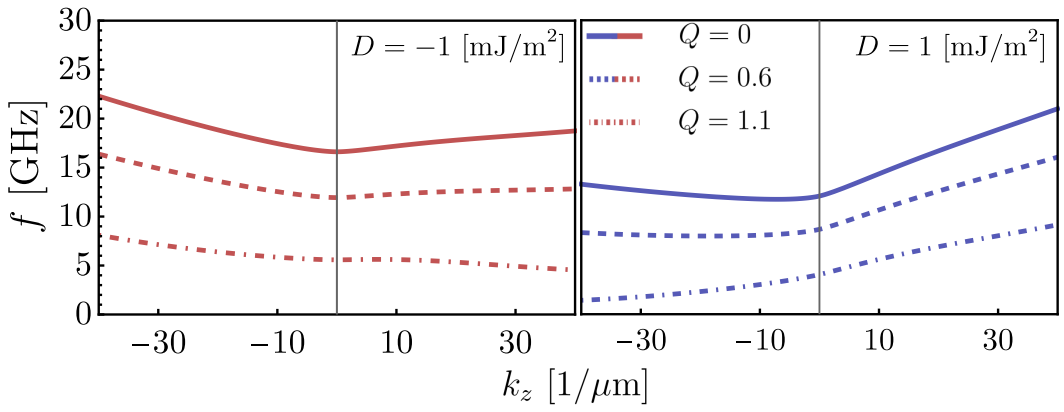

Figure 3.8: Spin-wave dispersion of the $l = 0$ mode in the vortex state. DMI values $D = -1$ mJ/m^2 and $D = 1$ mJ/m^2 are shown in the left (red) and right (blue) panels, respectively. Anisotropy values $K_u = Q\mu_0 M_s^2/2$ considered are $Q = 0, 0.6, 1.1$ in solid, dashed and dot-dashed lines respectively.

it does not change when the value of Q is modified. The dispersion curves in each case show a decreasing frequency for increasing values of the radial anisotropy and a change in the slope of $f(k_z)$. For example, the right diagram shows a negative slope of the dispersion curve with $Q = 0$ for $k_z < 0$, while for $Q = 1.1$ the slope becomes positive in the same range. This implies that for

a certain value of the anisotropy, the frequency can achieve the value $f = 0$ for some finite value of $k_z \neq 0$, which can give information about the texture formation in nanotubes. This idea will be further explored in Chapter 4.

In the saturated state, the radial anisotropy also decreases the frequency of each mode. Most importantly, the anisotropy affects the dynamic magnetization profile. Fig 3.9 shows the dynamic magnetization for two values

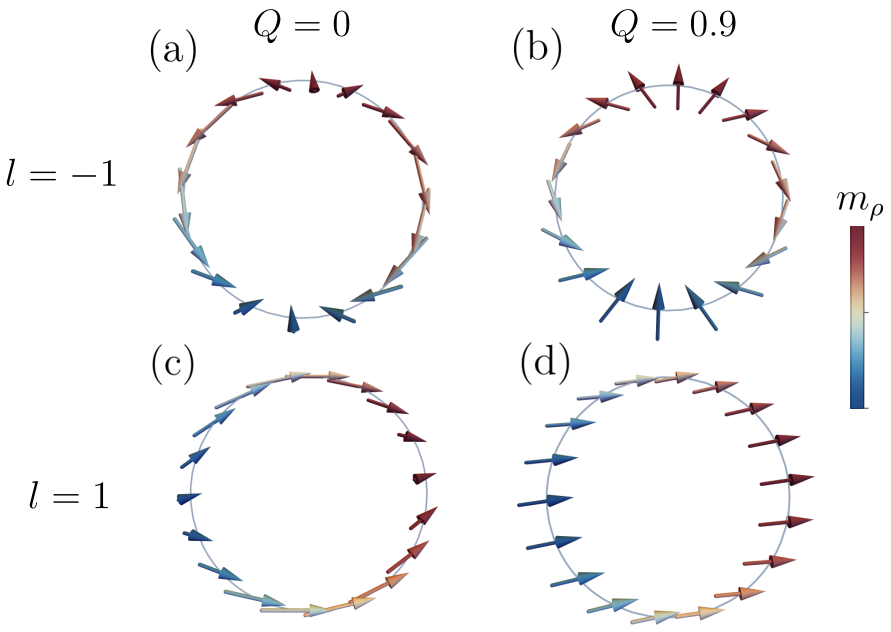

Figure 3.9: Illustration of the dynamic magnetization profiles for modes (a-b) $l = -1$ and (c-d) $l = 1$ for (a,c) $Q = 0$ and (b,d) $Q = 0.9$.

of the anisotropy, that is (a,c) $Q = 0$ and (b,d) $Q = 0.9$ of the $l = -1$ and $l = 1$ modes. The anisotropy changes the shape of the dynamic magnetization modes. In the cases $Q = 0.9$, the dynamic profiles are similar to the conical-helix modes (Fig. 2.2) for the same $n = 1$ and $n = -1$ values[2]. This is because at $Q = 0.9$, the anisotropy and the dipolar energy are almost compensated, and therefore, the eigenvectors associated with this frequency have a circular shape, namely $(1, \pm i)$. On the other hand, at $Q = 0$, the corresponding eigenvectors have an elliptical shape $(e, \pm i)$. Therefore, the zones with a radial component of the dynamic magnetization show a lower amplitude than the zones with mainly an azimuthal component in both $l = \pm 1$ cases. This is due to the dipolar effect

[2]In comparison with the CH model, the handedness is opposite. This is because of how the set of coordinates (χ, ρ, z') was defined. Nonetheless, this is a matter of convention, and the physical interpretation holds.

favoring the in-plane component of magnetization.

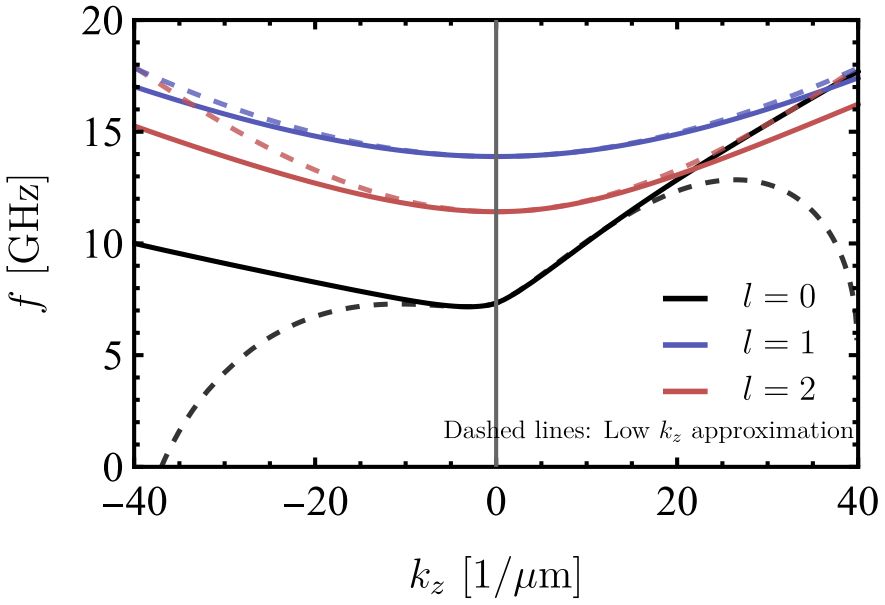

Figure 3.10: Spin waves frequency of the modes $l = 0$ (black), $l = 1$ (red) and $l = 2$ (blue) in the vortex state. Considered values are $K_u = 0$, $\mu_0 H = 150$ mT and $D = 1$ mJ/m^2. In dashed lines with the same colors, the first order in k_z approximations given by (3.40) and (3.41) are calculated.

Finally, Fig. 3.10 shows the low k_z approximation for modes $l = 0$ (black), $l = 1$ (red) and $l = 2$ (blue) in the vortex state. The dispersion relations are well described by these expressions (Eqs. (3.40) and (3.41)) in the low k limit for any value of l. Moreover, the methods for calculating these expressions are solid and permit the calculation of higher orders in k, which may reveal interesting features of the dipolar energy. However, this is out of the scope of this work.

Chapter 4

Dynamic Origin of the Conical-Helix Textures

The magnetic texture formed at the onset of the nucleation process can be predicted by analyzing the stability of the spin-wave dispersion at the saturated state. In magnetic stripes, it has been found that the lowest frequency standing-wave mode has the same spatial structure as the stripe domains at remanence [79]. In planar films with DMI, the conical-helix state is a reversion mode and is also connected with the spin waves excited close to the instability of the field-polarized state [67, 72]. In what follows, a nanotube of radius $R = 15$ nm and thickness $R - a = 3$ nm in the saturated state $\theta_0 = 0$ is considered to further investigate texture nucleation by analyzing spin-wave dynamics.

The spin-wave frequency of the vortex state at $D = 0$ is shown in Fig. 4.1. The frequency is diminished by decreasing the applied magnetic field that stabilizes the equilibrium magnetization. The frequency reaches zero at the critical point $\mu_0 H_{ze} = \mu_0 H_c = 22$ mT, where the equilibrium state becomes unstable. The system then changes its ground state and forms a magnetic texture. Such texture is directly related to the wavelength (k_z) and azimuthal index (l) at which the mode reaches zero. The reversion of the saturated state can be studied then by calculating the spin-wave frequency at $\theta_0 = 0$ and finding the critical (nucleation) field H_c and its corresponding (l, k_z) values. This process is done in the saturated state to explore the helix formation from the nucleation field.

Fig. 4.2 shows the spin-wave frequency as a function of the mode index l for a quality factor $Q = 0.9$. The values of the DMI considered are: $D = -4$ mJ/m^2

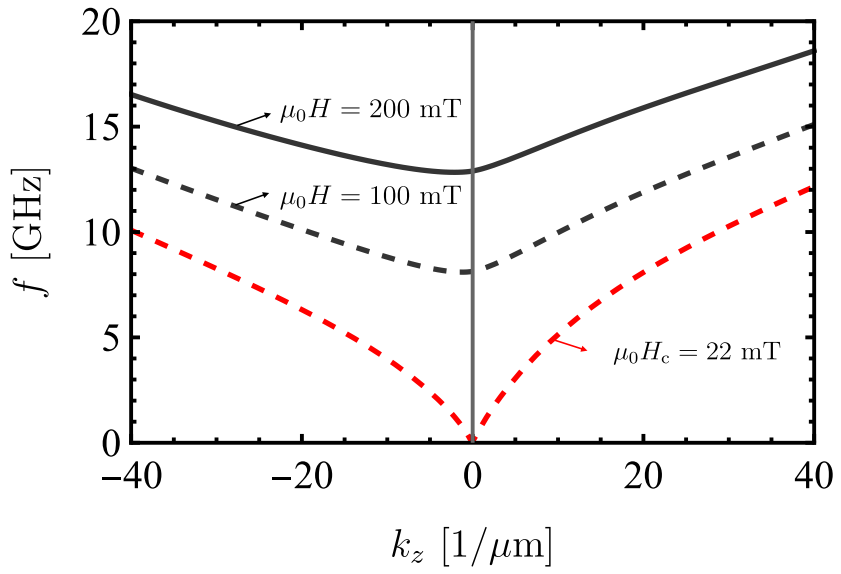

Figure 4.1: Spin-wave frequency in the vortex state ($\theta_0 = \pi/2$) for $l = 0$ and three values of the applied field. The frequency is zero at the critical value $\mu_0 H_c = 22$ mT, where the vortex state becomes unstable.

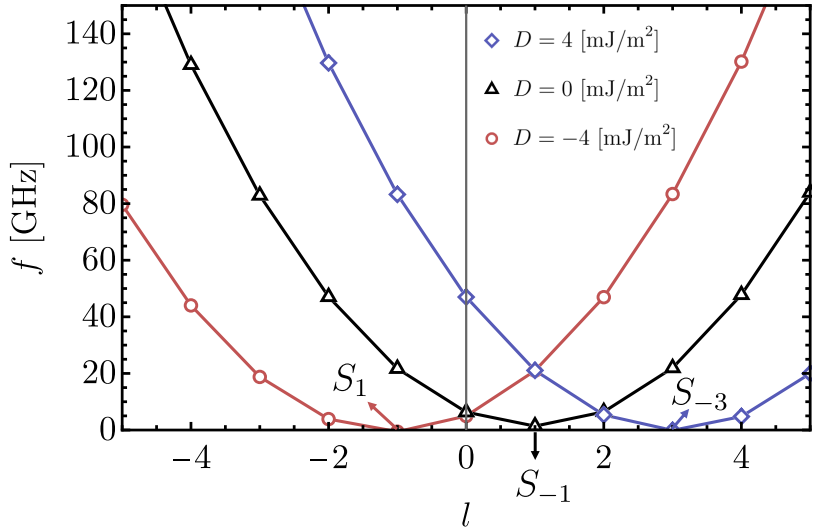

Figure 4.2: Frequency as a function of the azimuthal index l for a nanotube with radius $R = 15$ nm in the saturated state $\theta_0 = 0$. Three values of the DMI are considered, $D = -4$ mJ/m^2 (red circles), $D = 0$ mJ/m^2 (black triangles), and $D = 4$ mJ/m^2 (blue diamonds). Each curve is plotted at its corresponding critical field $H_c(D)$. The k-point at which the frequency reaches zero corresponds to the texture shown in the simulations (Fig. 2.3). At zero frequency, the corresponding simulated reversion modes are S_1, S_{-1} and S_{-3}.

(red circles), $D = 0$ (black triangles), and $D = -4$ mJ/m^2 (blue diamonds). Each curve has been plotted at an applied field such that it achieves the value $H =$

$H_c(D)$ where the frequency becomes zero. This critical field should coincide with the nucleation field, the field at which the saturated state is no longer stable and the texture formation starts to happen. Moreover, because the DMI causes an energy difference between the $+l$ and $-l$ modes, it causes the frequency to reach the zero value at different values of l. The dynamic profiles of the states at $l = -1$ and $l = 1$ are plotted for $Q = 0.9$ in Fig. 3.9 (b,d). The spatial distribution of these states resembles the states $n = 1$ and $n = -1$ depicted in Fig. 2.3. Every curve reaches this value at $k_z = 0$ except for the $l = 1$, for which it happens at a finite k_z due to dipolar effects (see the inset in Fig. 3.4).

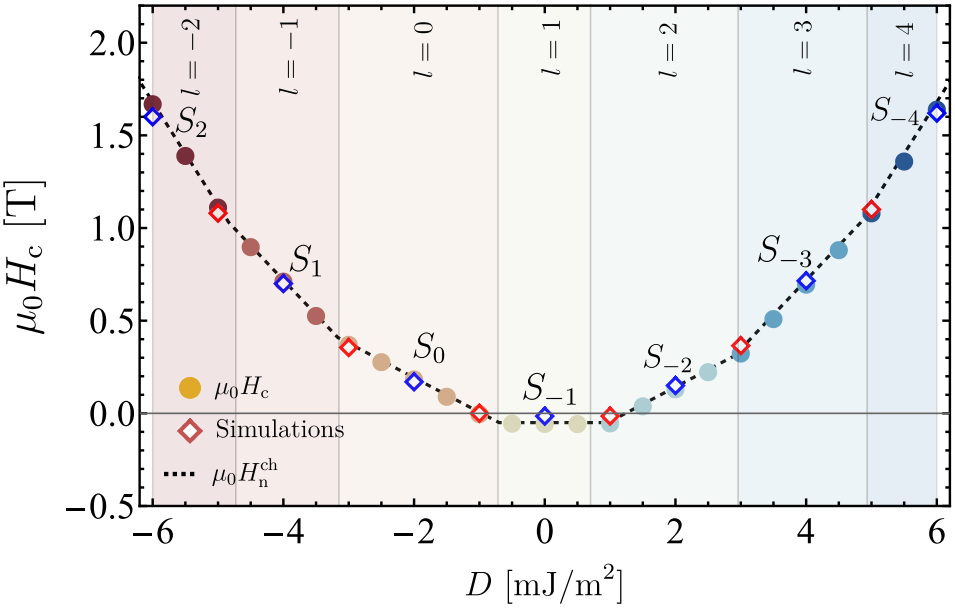

Figure 4.3: Critical field $\mu_0 H_c$ in colored dots as a function of the DMI strength for a nanotube with $R = 15$ nm in the saturated state and $Q = 0.9$, as studied in Fig. 2.6. The instability of the saturated state occurs at $k_z = 0$ and the color code represents each l index from $l = -2$ to $l = 4$. The dashed line is the maximum nucleation field evaluated as a function of D, namely $H_n^{ch}(n_{nt}(D))$. The diamonds represent the simulated values of the nucleation field, the blue being the states represented in Fig. 2.3 and the red being additional simulations. The simulated states, S_{-4} to S_2, are shown in Fig. 2.3, and the spin-wave frequency at the critical fields is plotted in Fig. 4.2.

The critical field as a function of the DMI for an anisotropy/dipolar ratio $Q = 0.9$ is depicted in Fig. 4.3 by the colored circles. The color coding corresponds to the background color that indicates the azimuthal index l at which the critical field occurs. The dashed lines represent the nucleation field at which each conical-helix reversal mode occurs, according to Eq. (2.22). Additionally, open

diamonds show the nucleation field obtained from the simulations, the blue ones being the states depicted in Fig. 2.3 and therefore also shown in diagrams 2.4 and 2.6. The critical field obtained from the spin wave instability, the nucleation field that results from the conical-helix model, and the nucleation field obtained by the micromagnetic simulations give the same results as seen in Fig. 4.3. As seen from equation (2.22), the nucleation field has a linear dependence on D. The slope is proportional to the $n = n_{\mathrm{nt}}$ value and therefore increases with increasing D. The n values obtained from the simulations and CH model are related to the l indexes obtained from spin waves as $n = -l$. This is because the n and l indexes have opposite chiralities (compare figures 2.2 and 3.9).

Two additional values of the radial anisotropy are calculated, $Q = 0$ (top diagram) and $Q = 2$ (bottom diagram), which are shown in Fig. 4.4. Because the radial anisotropy diminishes the frequency of the spin waves, the critical magnetic field is higher. Also, from Eqn. 2.22, it is noted that the nucleation field (black dashed curve) increases linearly with the radial anisotropy. The simulations still show that both the critical and the nucleation fields describe well the nucleation process even for $Q \approx 1$. The main difference is that in the analysis through the nucleation field, the states $l = \pm 1$ are not allowed for $Q = 0$ or $Q = 2$ (see Fig. 2.4) while the critical field of the spin waves shows that these states can still be formed for certain values of D. At higher or lower values of the radial anisotropy, the conical-helix model fails to describe the states formed because they are not circular anymore. In this regard, the critical field from spin-wave instability is more accurate due to the possibility of describing elliptical orbits of the helix states (see discussion of Fig. 3.9).

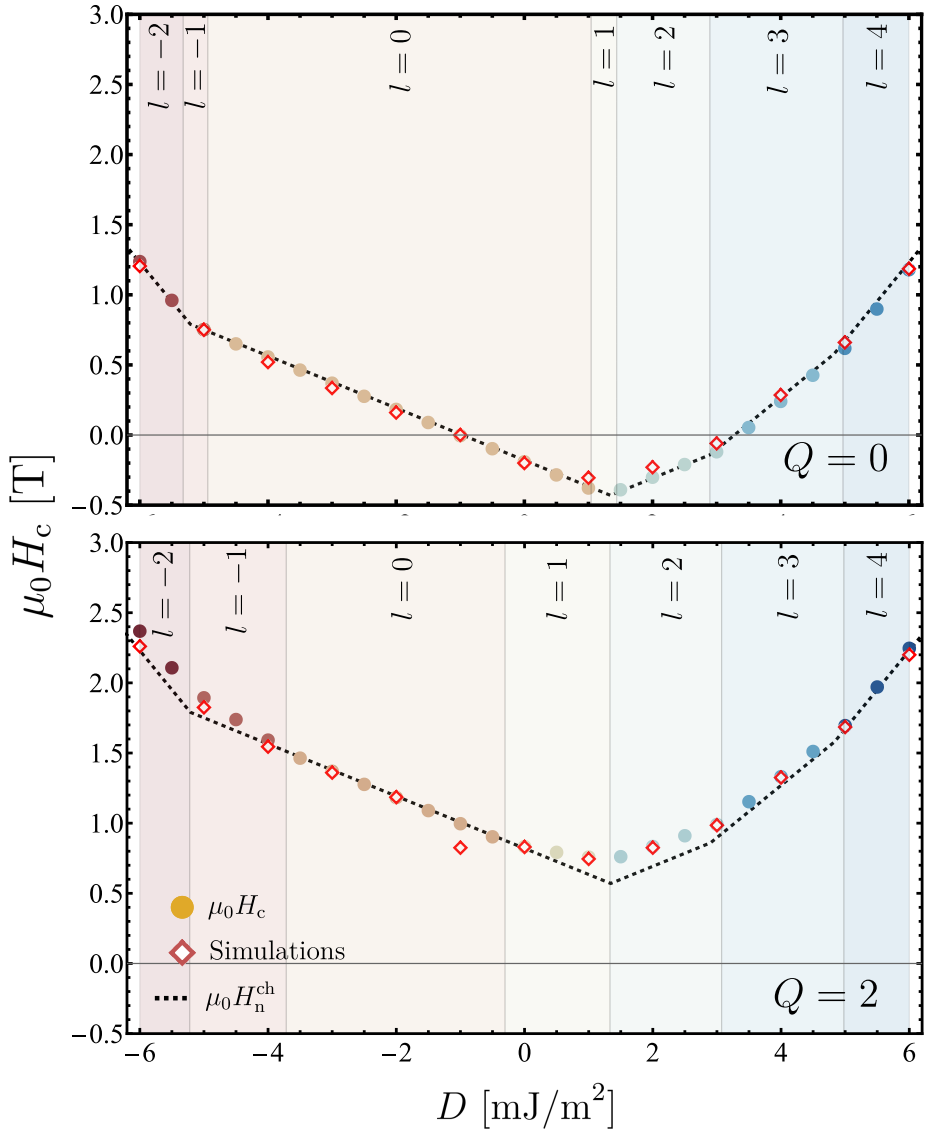

Figure 4.4: Critical field $\mu_0 H_c$ for a nanotube of radius $R = 15$ nm in the saturated state and anisotropy/dipolar ratios $Q = 0$ (top diagram) and $Q = 2$ (bottom diagram). Again a value $k_z = 0$ is considered and the color code represents each l index obtained from $l = -2$ to $l = 4$. The dashed line is the minimum nucleation field, while the diamonds represent the simulated values of the nucleation field.

4.1 Conclusions

This thesis has explored the effects of the interfacial Dzyaloshinskii-Moriya interaction (DMI) on magnetic nanotubes, focusing on the nucleation process and the nonreciprocity of spin waves. The magnetic textures formed in thin magnetic nanotubes with interfacial Dzyaloshinskii-Moriya interaction (DMI) have been studied using micromagnetic theory and simulations. Interfacial DMI induced by a heavy-metal interface coupled to the ferromagnetic material produces conical-helix (CH) structures with a pitch vector along the nanotube's perimeter, that is, perpendicular to the saturating field. Because of the periodicity induced by the cylindrical geometry, the pitch vector is quantized, and its possible values depend on the radius of the nanotube. The direction and the length of the pitch vector that characterizes the conical-helix textures are obtained, concluding that the sign of the DMI strength and the orientation of the equilibrium magnetization determines the chirality of the helix, which in curved systems competes with the contributions of exchange- and dipolar-induced chiral effects. The radial anisotropy is studied and is shown to be an important interaction; due to the preference of the dipolar interaction for in-plane magnetization, the out-of-plane easy axis anisotropy allows the circular orbits described by the (CH) model.

The study also investigated spin-wave dynamics in nanotubes with DMI. The dispersion relation was found as a function of θ_0, which parametrizes the equilibrium magnetization with limiting cases being the vortex and axially saturated magnetization states. Therefore, the effect of the DMI on the spin wave frequency and normal modes in both states and intermediate states can be easily compared. The frequency nonreciprocity—difference in the frequency of counter-propagating spin waves—induced by curvature is compensated or magnified by the DM interaction, which also induces chiral behavior. The presence of radial anisotropy has also been analyzed and found to induce interesting dynamic modes and oscillation profiles. Additionally, an approximation to small wave vectors provides analytical formulas of the dipolar terms. These calculations can be further extended for higher-order approximations, which could reveal interesting features of the dipolar interaction.

Finally, the spin-wave instability analysis provides a different method to

study texture formation in nanotubes. By identifying the critical field at which a normal mode reaches zero frequency, the nucleation fields and spatial magnetization distribution during the transition from a saturated state to a CH texture are obtained. It has been found that these critical fields coincide with the nucleation fields obtained both by the CH model and through simulations. These findings offer valuable insight into the interplay between curvature, anisotropy, and chiral interactions in magnetic nanotubes, with potential applications in magnonics and spintronic devices.

Bibliography

[1] A.P. Guimarães. *Principles of Nanomagnetism*. NanoScience and Technology. Springer International Publishing, 2017. ISBN 9783319594101. URL https://books.google.cl/books?id=YOIrvwEACAAJ.

[2] Elsa M. Materón, Celina M. Miyazaki, Olivia Carr, Nirav Joshi, Paulo H.S. Picciani, Cleocir J. Dalmaschio, Frank Davis, and Flavio M. Shimizu. Magnetic nanoparticles in biomedical applications: A review. *Applied Surface Science Advances*, 6:100163, 2021. ISSN 2666-5239. doi: https://doi.org/10.1016/j.apsadv.2021.100163. URL https://www.sciencedirect.com/science/article/pii/S2666523921001094.

[3] G. Binasch, P. Grünberg, F. Saurenbach, and W. Zinn. Enhanced magnetoresistance in layered magnetic structures with antiferromagnetic interlayer exchange. *Phys. Rev. B*, 39:4828–4830, Mar 1989. doi: 10.1103/PhysRevB.39.4828. URL https://link.aps.org/doi/10.1103/PhysRevB.39.4828.

[4] M. N. Baibich, J. M. Broto, A. Fert, F. Nguyen Van Dau, F. Petroff, P. Etienne, G. Creuzet, A. Friederich, and J. Chazelas. Giant magnetoresistance of (001)fe/(001)cr magnetic superlattices. *Phys. Rev. Lett.*, 61:2472–2475, Nov 1988. doi: 10.1103/PhysRevLett.61.2472. URL https://link.aps.org/doi/10.1103/PhysRevLett.61.2472.

[5] The Royal Swedish Academy of Sciences. The discovery of giant magnetoresistance. *AAPPS Bulletin*, 17(6):2–11, December 2007. Originally released by the Nobel Foundation on the website Nobel e-Museum.

[6] A.O. Adeyeye and G. Shimon. Chapter 1 - growth and characterization of magnetic thin film and nanostructures. In Robert E. Camley, Zbigniew Celinski, and Robert L. Stamps, editors, *Magnetism of Surfaces, Interfaces, and Nanoscale Materials*, volume 5 of *Handbook of Surface Science*, pages 1–41. North-Holland, 2015. doi: https://doi.org/10.1016/B978-0-444-62634-9.00001-1. URL https://www.sciencedirect.com/science/article/pii/B9780444626349000011.

[7] Pierre Weiss. L'hypothèse du champ moléculaire et la propriété ferromagnétique. *J. Phys. Theor. Appl.*, 6(1):661–690, 1907. doi: 10.1051/jphystap:019070060066100. URL https://hal.science/jpa-00241247.

[8] Haiming Yu, Jiang Xiao, and Helmut Schultheiss. Magnetic texture based magnonics. *Physics Reports*, 905:1–59, 2021. ISSN 0370-1573. doi: https://doi.org/10.1016/j.physrep.2020.12.004. URL https://www.sciencedirect.com/science/article/pii/S0370157320304270. Magnetic texture based magnonics.

[9] Börge Göbel, Ingrid Mertig, and Oleg A. Tretiakov. Beyond skyrmions: Review and perspectives of alternative magnetic quasiparticles. *Physics Reports*, 895:1–28, 2021. ISSN 0370-1573. doi: https://doi.org/10.1016/j.physrep.2020.10.001. URL https://www.sciencedirect.com/science/article/pii/S0370157320303525. Beyond skyrmions: Review and perspectives of alternative magnetic quasiparticles.

[10] Naoto Nagaosa and Yoshinori Tokura. Topological properties and dynamics of magnetic skyrmions. *Nature Nanotechnology*, 8(12):899–911, 2013. doi: 10.1038/nnano.2013.243. URL https://doi.org/10.1038/nnano.2013.243.

[11] Markus Garst, Johannes Waizner, and Dirk Grundler. Collective spin excitations of helices and magnetic skyrmions: review and perspectives of magnonics in non-centrosymmetric magnets. *Journal of Physics D: Applied Physics*, 50(29):293002, jun 2017. doi: 10.1088/1361-6463/aa7573. URL https://dx.doi.org/10.1088/1361-6463/aa7573.

[12] M. Bode, M. Heide, K. von Bergmann, P. Ferriani, S. Heinze, G. Bihlmayer, A. Kubetzka, O. Pietzsch, S. Blügel, and R. Wiesendanger. Chiral magnetic order at surfaces driven by inversion asymmetry. *Nature*, 447(7141):190–193, 2007. ISSN 1476-4687. doi: 10.1038/nature05802. URL https://doi.org/10.1038/nature05802.

[13] Albert Fert, Mairbek Chshiev, André Thiaville, and Hongxin Yang. From Early Theories of Dzyaloshinskii–Moriya Interactions in Metallic Systems to Today's Novel Roads. *Journal of the Physical Society of Japan*, 92:081001, April 2023. doi: 10.7566/JPSJ.92.081001. URL https://hal.science/hal-04098774.

[14] Z.V. Gareeva, N.V. Shulga, and R.A. Doroshenko. Influence of the dzyaloshinskii – moriya interaction on the properties of magnetic states in nanostructures. *Journal of Magnetism and Magnetic Materials*, 536:168079, 2021. ISSN 0304-8853. doi: https://doi.org/10.1016/j.jmmm.2021.168079. URL https://www.sciencedirect.com/science/article/pii/S0304885321003553.

[15] Charles S. Spencer, Jacob Gayles, Nicholas A. Porter, Satoshi Sugimoto, Zabeada Aslam, Christian J. Kinane, Timothy R. Charlton, Frank Freimuth, Stanislav Chadov, Sean Langridge, Jairo Sinova, Claudia Felser, Stefan Blügel, Yuriy Mokrousov, and Christopher H. Marrows. Helical magnetic structure and the anomalous and topological hall effects in epitaxial b20

$fe_{1-y}co_yGe$ films. *Phys. Rev. B*, 97:214406, Jun 2018. doi: 10.1103/PhysRevB.97.214406. URL https://link.aps.org/doi/10.1103/PhysRevB.97.214406.

[16] David Galvez, Mario Castro, Guilherme Bittencourt, Vagson Carvalho, and Sebastian Allende. Magnetic bimerons in cylindrical nanotubes. *Nanomaterials*, 13(21), 2023. ISSN 2079-4991. doi: 10.3390/nano13212841. URL https://www.mdpi.com/2079-4991/13/21/2841.

[17] Robert E. Camley and Karen L. Livesey. Consequences of the dzyaloshinskii-moriya interaction. *Surface Science Reports*, 78(3):100605, 2023. ISSN 0167-5729. doi: https://doi.org/10.1016/j.surfrep.2023.100605. URL https://www.sciencedirect.com/science/article/pii/S0167572923000201.

[18] Roland Wiesendanger. Nanoscale magnetic skyrmions in metallic films and multilayers: a new twist for spintronics. *Nature Reviews Materials*, 1 (7):16044, 2016. doi: 10.1038/natrevmats.2016.44. URL https://doi.org/10.1038/natrevmats.2016.44. Accessed: 2025-03-03.

[19] Albert Fert, Nicolas Reyren, and Vincent Cros. Magnetic skyrmions: advances in physics and potential applications. *Nature Reviews Materials*, 2(7):17031, 2017. ISSN 2058-8437. doi: 10.1038/natrevmats.2017.31. URL https://doi.org/10.1038/natrevmats.2017.31.

[20] R. A. Gallardo, D. Cortés-Ortuño, R. E. Troncoso, and P. Landeros. *Three-dimensional magnonics: layered, micro-and nanostructures*, pages 121–160. Jenny Stanford Publishing, Berlin, Heidelberg, 2019. ISBN 9789814800730. URL https://www.crcpress.com/Three-Dimensional-Magnonics/Gubbiotti/p/book/9789814800730.

[21] M. Kuepferling, A. Casiraghi, G. Soares, G. Durin, F. Garcia-Sanchez, L. Chen, C. H. Back, C. H. Marrows, S. Tacchi, and G. Carlotti. Measuring interfacial dzyaloshinskii-moriya interaction in ultrathin magnetic films. *Rev. Mod. Phys.*, 95:015003, Mar 2023. doi: 10.1103/RevModPhys.95.015003. URL https://link.aps.org/doi/10.1103/RevModPhys.95.015003.

[22] Anjan Barman, Gianluca Gubbiotti, S Ladak, A O Adeyeye, M Krawczyk, J Gräfe, C Adelmann, S Cotofana, A Naeemi, V I Vasyuchka, B Hillebrands, S A Nikitov, H Yu, D Grundler, A V Sadovnikov, A A Grachev, S E Sheshukova, J-Y Duquesne, M Marangolo, G Csaba, W Porod, V E Demidov, S Urazhdin, S O Demokritov, E Albisetti, D Petti, R Bertacco, H Schultheiss, V V Kruglyak, V D Poimanov, S Sahoo, J Sinha, H Yang, M Münzenberg, T Moriyama, S Mizukami, P Landeros, R A Gallardo, G Carlotti, J-V Kim, R L Stamps, R E Camley, B Rana, Y Otani, W Yu, T Yu, G E W Bauer, C Back, G S Uhrig, O V Dobrovolskiy, B Budinska, H Qin, S van Dijken, A V Chumak, A Khitun, D E Nikonov, I A Young, B W Zingsem, and M Winklhofer. The 2021 magnonics roadmap. *Journal of Physics: Condensed Matter*, 33(41):413001, aug 2021. doi: 10.1088/1361-648X/abec1a. URL https://dx.doi.org/10.1088/1361-648X/abec1a.

[23] Benedetta Flebus, Dirk Grundler, Bivas Rana, YoshiChika Otani, Igor Barsukov, Anjan Barman, Gianluca Gubbiotti, Pedro Landeros, Johan Akerman, Ursula Ebels, Philipp Pirro, Vladislav E Demidov, Katrin Schultheiss, Gyorgy Csaba, Qi Wang, Florin Ciubotaru, Dmitri E Nikonov, Ping Che, Riccardo Hertel, Teruo Ono, Dmytro Afanasiev, Johan Mentink, Theo Rasing, Burkard Hillebrands, Silvia Viola Kusminskiy, Wei Zhang, Chunhui Rita Du, Aurore Finco, Toeno van der Sar, Yunqiu Kelly Luo, Yoichi Shiota, Joseph Sklenar, Tao Yu, and Jinwei Rao. The 2024 magnonics roadmap. *J. Phys. Condens. Matter*, 36(36):363501, jun 2024. doi: 10.1088/1361-648X/ad399c. URL https://dx.doi.org/10.1088/1361-648X/ad399c.

[24] A. V. Chumak, V. I. Vasyuchka, A. A. Serga, and B. Hillebrands. Magnon spintronics. *Nature Physics*, 11:453–461, 2015. doi: 10.1038/nphys3347.

[25] Q. Wang, H. Y. Yuan, and X. R. Wang. Magnon transistor for all-magnon data processing. *Physical Review Letters*, 124(12):127202, 2020. doi: 10.1103/PhysRevLett.124.127202.

[26] M. Madami, S. Bonetti, G. Consolo, S. Tacchi, G. Carlotti, G. Gubbiotti, F. B. Mancoff, M. A. Yar, and J. Åkerman. Direct observation of a propagating spin wave induced by spin-transfer torque. *Nature Nanotechnology*, 6(10):635–638, 2011. ISSN 1748-3395. doi: 10.1038/nnano.2011.140. URL https://doi.org/10.1038/nnano.2011.140.

[27] Y. Kajiwara, K. Harii, S. Takahashi, J. Ohe, K. Uchida, M. Mizuguchi, H. Umezawa, H. Kawai, K. Ando, K. Takanashi, S. Maekawa, and E. Saitoh. Transmission of electrical signals by spin-wave interconversion in a magnetic insulator. *Nature*, 464(7286):262–266, 2010. ISSN 1476-4687. doi: 10.1038/nature08876. URL https://doi.org/10.1038/nature08876.

[28] Mahdi Jamali, Jae Hyun Kwon, Soo-Man Seo, Kyung-Jin Lee, and Hyunsoo Yang. Spin wave nonreciprocity for logic device applications. *Scientific Reports*, 3(1):3160, 2013. doi: 10.1038/srep03160. URL https://doi.org/10.1038/srep03160.

[29] Jin Lan, Weichao Yu, Ruqian Wu, and Jiang Xiao. Spin-wave diode. *Phys. Rev. X*, 5:041049, Dec 2015. doi: 10.1103/PhysRevX.5.041049. URL https://link.aps.org/doi/10.1103/PhysRevX.5.041049.

[30] Negar Reiskarimian and Harish Krishnaswamy. Magnetic-free non-reciprocity based on staggered commutation. *Nature Communications*, 7(1):11217, 2016. ISSN 2041-1723. doi: 10.1038/ncomms11217. URL https://doi.org/10.1038/ncomms11217.

[31] Robert Streubel, Peter Fischer, Florian Kronast, Volodymyr P Kravchuk, Denis D Sheka, Yuri Gaididei, Oliver G Schmidt, and Denys Makarov. Magnetism in curved geometries. *Journal of Physics D: Applied Physics*, 49(36):363001, aug 2016. doi: 10.1088/0022-3727/49/36/363001. URL https://dx.doi.org/10.1088/0022-3727/49/36/363001.

[32] Denys Makarov and Denis Sheka (Eds.). *Curvilinear Micromagnetism: From Fundamental to Applications*. Springer, 2022.

[33] P. Landeros and Álvaro S. Núñez. Domain wall motion on magnetic nanotubes. *Journal of Applied Physics*, 108(3):033917, 08 2010. ISSN 0021-8979. doi: 10.1063/1.3466747. URL https://doi.org/10.1063/1.3466747.

[34] Denis D. Sheka, Oleksandr V. Pylypovskyi, Pedro Landeros, Yuri Gaididei, Attila Kákay, and Denys Makarov. Nonlocal chiral symmetry breaking in curvilinear magnetic shells. *Commun. Phys.*, 3(1):128, 2020. doi: 10.1038/s42005-020-0387-2. URL https://doi.org/10.1038/s42005-020-0387-2.

[35] Mykola I. Sloika, Yuri Gaididei, Volodymyr P. Kravchuk, Oleksandr V. Pylypovskyi, Denys Makarov, and Denis D. Sheka. Impact of curvature-induced dzyaloshinskii–moriya interaction on magnetic vortex texture in spherical caps. *Low Temperature Physics*, 48(11):956–961, 11 2022. ISSN 1063-777X. doi: 10.1063/10.0014596. URL https://doi.org/10.1063/10.0014596.

[36] J.A. Otálora, J.A. López-López, P. Landeros, P. Vargas, and A.S. Núñez. Breaking of chiral symmetry in vortex domain wall propagation in ferromagnetic nanotubes. *J. Magn. Magn. Mater.*, 341:86–92, 2013. ISSN 0304-8853. doi: https://doi.org/10.1016/j.jmmm.2013.04.014. URL https://www.sciencedirect.com/science/article/pii/S0304885313002333.

[37] H. D. Salinas, J. Restrepo, and Òscar Iglesias. Change in the magnetic configurations of tubular nanostructures by tuning dipolar interactions. *Scientific Reports*, 8(1):10275, 2018. ISSN 2045-2322. doi: 10.1038/s41598-018-28598-1. URL https://doi.org/10.1038/s41598-018-28598-1.

[38] Riccardo Hertel. Computational micromagnetism of magnetization processes in nickel nanowires. *Journal of Magnetism and Magnetic Materials*, 249(1):251–256, 2002. ISSN 0304-8853. doi: https://doi.org/10.1016/S0304-8853(02)00539-5. URL https://www.sciencedirect.com/science/article/pii/S0304885302005395. International Workshop on Magnetic Wires.

[39] P. Landeros, S. Allende, J. Escrig, E. Salcedo, D. Altbir, and E. E. Vogel. Reversal modes in magnetic nanotubes. *Applied Physics Letters*, 90(10):102501, 03 2007. ISSN 0003-6951. doi: 10.1063/1.2437655. URL https://doi.org/10.1063/1.2437655.

[40] Manuel Vázquez. *Magnetic Nano-and Microwires: Design, Synthesis, Properties and Applications*. Woodhead Publishing, 2020.

[41] Pedro Landeros, Jorge A. Otálora, Robert Streubel, and Attila Kákay. *Tubular Geometries*, pages 163–213. Springer International Publishing, Cham, 2022. ISBN 978-3-031-09086-8. doi: 10.1007/978-3-031-09086-8_4. URL https://doi.org/10.1007/978-3-031-09086-8_4.

[42] Michal Staňo and Olivier Fruchart. Chapter 3 - magnetic nanowires and nanotubes. volume 27 of *Handbook of Magnetic Materials*, pages 155–267. Elsevier, 2018. doi: https://doi.org/10.1016/bs.hmm.2018.08.002. URL https://www.sciencedirect.com/science/article/pii/S1567271918300027.

[43] Luc Piraux. Magnetic nanowires. *Applied Sciences*, 10(5), 2020. ISSN 2076-3417. doi: 10.3390/app10051832. URL https://www.mdpi.com/2076-3417/10/5/1832.

[44] DF Gutierrez-Guzman, LI Lizardi, JA Otálora, and P Landeros. Hyperthermia in low aspect-ratio magnetic nanotubes for biomedical applications. *Applied Physics Letters*, 110(13), 2017. doi: 10.1063/1.4979165. URL https://doi.org/10.1063/1.4979165.

[45] P. Landeros, O. J. Suarez, A. Cuchillo, and P. Vargas. Equilibrium states and vortex domain wall nucleation in ferromagnetic nanotubes. *Phys. Rev. B*, 79:024404, 2009. doi: 10.1103/PhysRevB.79.024404.

[46] A. Mehlin, B. Gross, M. Wyss, T. Schefer, G. Tütüncüoglu, F. Heimbach, A. Fontcuberta i Morral, D. Grundler, and M. Poggio. Observation of end-vortex nucleation in individual ferromagnetic nanotubes. *Phys. Rev. B*, 97: 134422, Apr 2018. doi: 10.1103/PhysRevB.97.134422. URL https://link.aps.org/doi/10.1103/PhysRevB.97.134422.

[47] Jorge A. Otálora, Ming Yan, Helmut Schultheiss, Riccardo Hertel, and Attila Kákay. Curvature-induced asymmetric spin-wave dispersion. *Phys. Rev. Lett.*, 117:227203, Nov 2016. doi: 10.1103/PhysRevLett.117.227203. URL https://link.aps.org/doi/10.1103/PhysRevLett.117.227203.

[48] R. A. Gallardo, P. Alvarado-Seguel, and P. Landeros. High spin-wave asymmetry and emergence of radial standing modes in thick ferromagnetic nanotubes. *Phys. Rev. B*, 105:104435, Mar 2022. doi: 10.1103/PhysRevB.105.104435. URL https://link.aps.org/doi/10.1103/PhysRevB.105.104435.

[49] L. Körber, R. Verba, Jorge A. Otálora, V. Kravchuk, J. Lindner, J. Fassbender, and A. Kákay. Curvilinear spin-wave dynamics beyond the thin-shell approximation: Magnetic nanotubes as a case study. *Phys. Rev. B*, 106:014405, Jul 2022. doi: 10.1103/PhysRevB.106.014405. URL https://link.aps.org/doi/10.1103/PhysRevB.106.014405.

[50] J. A. Otálora, A. Kákay, J. Lindner, H. Schultheiss, A. Thomas, J. Fassbender, and K. Nielsch. Frequency linewidth and decay length of spin waves in curved magnetic membranes. *Phys. Rev. B*, 98:014403, Jul 2018. doi: 10.1103/PhysRevB.98.014403. URL https://link.aps.org/doi/10.1103/PhysRevB.98.014403.

[51] A. Aharoni. *Introduction to the Theory of Ferromagnetism*. International Series of Monographs on Physics. Clarendon Press, 2000. ISBN 9780198508090. URL https://books.google.cl/books?id=Ru-z9b3WcfMC.

[52] Claas Abert. Micromagnetics and spintronics: models and numerical methods. *The European Physical Journal B*, 92(6):120, 06 2019. ISSN 1434-6036. doi: 10.1140/epjb/e2019-90599-6. URL https://doi.org/10.1140/epjb/e2019-90599-6.

[53] W.F. Brown. *Micromagnetics*. Interscience tracts on physics and astronomy. Interscience Publishers, 1963. URL https://books.google.cl/books?id=KvuXnAEACAAJ.

[54] O. Madelung. *Introduction to Solid-State Theory*. Springer Series in Solid-State Sciences. Springer, 1996. ISBN 9783540604433. URL https://books.google.cl/books?id=yK_J-3_p8_oC.

[55] A. Altland and B.D. Simons. *Condensed Matter Field Theory*. Cambridge books online. Cambridge University Press, 2010. ISBN 9780521769754. URL https://books.google.cl/books?id=GpF0Pgo8CqAC.

[56] David Ignacio Cortés Ortuño. Influencia de las interacciones de dzyaloshinskii-moriya en el espectro de ondas de espín de láminas ferromagnéticas delgadas. Master's thesis, Universidad Tecnica Federico Santa Maria, Valparaiso, Chile, 2013.

[57] Jürgen Lindner and Michael Farle. *Magnetic Anisotropy of Heterostructures*, pages 45–96. Springer Berlin Heidelberg, Berlin, Heidelberg, 2008. ISBN 978-3-540-73462-8. doi: 10.1007/978-3-540-73462-8_2. URL https://doi.org/10.1007/978-3-540-73462-8_2.

[58] John David Jackson. *Classical electrodynamics*. Wiley, New York, NY, 3rd ed. edition, 1999. ISBN 9780471309321. URL http://cdsweb.cern.ch/record/490457.

[59] A. Crépieux and C. Lacroix. Dzyaloshinsky–moriya interactions induced by symmetry breaking at a surface. *Journal of Magnetism and Magnetic Materials*, 182(3):341–349, 1998. ISSN 0304-8853. doi: https://doi.org/10.1016/S0304-8853(97)01044-5. URL https://www.sciencedirect.com/science/article/pii/S0304885397010445.

[60] I. E. Dzyaloshinskii. A thermodynamic theory of weak ferromagnetism of antiferromagnetics. *Journal of Physics and Chemistry of Solids*, 4:241–255, 1958.

[61] I. Dzyaloshinsky. A thermodynamic theory of "weak" ferromagnetism of antiferromagnetics. *Journal of Physics and Chemistry of Solids*, 4(4):241–255, 1958. ISSN 0022-3697. doi: https://doi.org/10.1016/

0022-3697(58)90076-3. URL https://www.sciencedirect.com/science/article/pii/0022369758900763.

[62] Tôru Moriya. Anisotropic superexchange interaction and weak ferromagnetism. *Phys. Rev.*, 120:91–98, Oct 1960. doi: 10.1103/PhysRev.120.91. URL https://link.aps.org/doi/10.1103/PhysRev.120.91.

[63] S. Tacchi, R. E. Troncoso, M. Ahlberg, G. Gubbiotti, M. Madami, J. Åkerman, and P. Landeros. Interfacial dzyaloshinskii-moriya interaction in Pt/CoFeB films: Effect of the heavy-metal thickness. *Phys. Rev. Lett.*, 118:147201, Apr 2017. doi: 10.1103/PhysRevLett.118.147201. URL https://link.aps.org/doi/10.1103/PhysRevLett.118.147201.

[64] A. Fert and Peter M. Levy. Role of anisotropic exchange interactions in determining the properties of spin-glasses. *Phys. Rev. Lett.*, 44:1538–1541, Jun 1980. doi: 10.1103/PhysRevLett.44.1538. URL https://link.aps.org/doi/10.1103/PhysRevLett.44.1538.

[65] Peter M. Levy and A. Fert. Anisotropy induced by nonmagnetic impurities in Cu mn spin-glass alloys. *Phys. Rev. B*, 23:4667–4690, May 1981. doi: 10.1103/PhysRevB.23.4667. URL https://link.aps.org/doi/10.1103/PhysRevB.23.4667.

[66] Albert Fert, Vincent Cros, and João Sampaio. Skyrmions on the track. *Nature Nanotechnology*, 8(3):152–156, 2013. ISSN 1748-3395. doi: 10.1038/nnano.2013.29. URL https://doi.org/10.1038/nnano.2013.29.

[67] C. Ríos-Venegas, F. Brevis, R. A. Gallardo, and P. Landeros. Dynamic origin of conical helix magnetization textures stabilized by dzyaloshinskii-moriya interaction. *Phys. Rev. B*, 105:224403, Jun 2022. doi: 10.1103/PhysRevB.105.224403. URL https://link.aps.org/doi/10.1103/PhysRevB.105.224403.

[68] D Mancilla-Almonacid, R Jaeschke-Ubiergo, A S Núñez, and S Allende. Ultrafast domain wall propagation due to the interfacial dzyaloshinskii–moriya interaction. *Nanotechnology*, 31(12):125707, jan 2020. doi: 10.1088/1361-6528/ab5f83. URL https://dx.doi.org/10.1088/1361-6528/ab5f83.

[69] Nam-Hui Kim, Dong-Soo Han, Jinyong Jung, Kwonjin Park, Henk J. M. Swagten, June-Seo Kim, and Chun-Yeol You. Dependence of interfacial dzyaloshinskii–moriya interaction and perpendicular magnetic anisotropy on the thickness of the heavy-metal layer. *Applied Physics Express*, 10(10):103003, sep 2017. doi: 10.7567/APEX.10.103003. URL https://dx.doi.org/10.7567/APEX.10.103003.

[70] A. S. Samardak, A. V. Davydenko, A. G. Kolesnikov, A. Yu. Samardak, A. G. Kozlov, Bappaditya Pal, A. V. Ognev, A. V. Sadovnikov, S. A. Nikitov, A. V. Gerasimenko, In Ho Cha, Yong Jin Kim, Gyu Won Kim, Oleg A.

Tretiakov, and Young Keun Kim. Enhancement of perpendicular magnetic anisotropy and dzyaloshinskii–moriya interaction in thin ferromagnetic films by atomic-scale modulation of interfaces. *NPG Asia Materials*, 12 (1):51, 2020. ISSN 1884-4057. doi: 10.1038/s41427-020-0232-9. URL https://doi.org/10.1038/s41427-020-0232-9.

[71] B. Mimica-Figari, F. Brevis, D. Cortés-Ortuño, R. A. Gallardo, and P. Landeros. Magnetic textures in nanotubes with interfacial Dzyaloshinskii-Moriya interaction. *unpublished*, 2025.

[72] Jan Kisielewski, Paweł Gruszecki, Maciej Krawczyk, Vitalii Zablotskii, and Andrzej Maziewski. Between waves and patterns: Spin wave freezing in films with dzyaloshinskii-moriya interaction. *Phys. Rev. B*, 107:134416, Apr 2023. doi: 10.1103/PhysRevB.107.134416. URL https://link.aps.org/doi/10.1103/PhysRevB.107.134416.

[73] Marc-Antonio Bisotti, Marijan Beg, Weiwei Wang, Maximilian Albert, Dmitri Chernyshenko, David Cortés-Ortuño, Ryan A. Pepper, Mark Vousden, Rebecca Carey, Hagen Fuchs, Anders Johansen, Gabriel Balaban, Leoni Breth, Thomas Kluyver, and Hans Fangohr. FinMag: finite-element micromagnetic simulation tool, April 2018. URL https://doi.org/10.5281/zenodo.1216011.

[74] David Cortés-Ortuño. Fork of FinMag: finite-element micromagnetic simulation tool. Github https://github.com/davidcortesortuno/finmag. Version 0.1d., 2024. URL https://github.com/davidcortesortuno/finmag.

[75] C. Bane Sullivan and Alexander Kaszynski. PyVista: 3d plotting and mesh analysis through a streamlined interface for the visualization toolkit (VTK). *Journal of Open Source Software*, 4(37):1450, may 2019. doi: 10.21105/joss.01450. URL https://doi.org/10.21105/joss.01450.

[76] M. M. Salazar-Cardona, L. Körber, H. Schultheiss, K. Lenz, A. Thomas, K. Nielsch, A. Kákay, and J. A. Otálora. Nonreciprocity of spin waves in magnetic nanotubes with helical equilibrium magnetization. *Appl. Phys. Lett.*, 118(26):262411, 06 2021. ISSN 0003-6951. doi: 10.1063/5.0048692. URL https://doi.org/10.1063/5.0048692.

[77] George B Arfken and Hans J Weber. *Mathematical methods for physicists; 4th ed.* Academic Press, San Diego, CA, 1995. URL https://cds.cern.ch/record/379118.

[78] B. Mimica-Figari, P. Landeros, and R. A. Gallardo. Spin-wave dynamics in nanotubes with interfacial Dzyaloshinskii-Moriya interaction. *unpublished*, 2025.

[79] G. Leaf, H. Kaper, M. Yan, V. Novosad, P. Vavassori, R. E. Camley, and M. Grimsditch. Dynamic origin of stripe domains. *Phys. Rev. Lett.*, 96:

017201, Jan 2006. doi: 10.1103/PhysRevLett.96.017201. URL https://link.aps.org/doi/10.1103/PhysRevLett.96.017201.

[80] Kostiantyn V. Yershov, Volodymyr P. Kravchuk, Denis D. Sheka, and Ulrich K. Rößler. Curvature effects on phase transitions in chiral magnets. *SciPost Phys.*, 9:043, 2020. doi: 10.21468/SciPostPhys.9.4.043. URL https://scipost.org/10.21468/SciPostPhys.9.4.043.

Appendix A

Dipolar Energy of the Conical-Helix

The magnetostatic general solution for energy is given by Eq. (1.21). The effective field $\boldsymbol{H}_\mathrm{d} = -\nabla\Phi$ is calculated by using the magnetostatic potential form of Eq. (1.20) and the CH magnetization model (2.1). The following cylindrical expansion is used [58][1]:

$$\begin{aligned}\frac{1}{|\boldsymbol{r}-\boldsymbol{r}'|} &= \sum_{j=-\infty}^{\infty} e^{ij(\phi-\phi')}\int_0^\infty J_j(x\rho)J_j(x\rho')e^{-x|z-z'|}dx \\ &= \frac{1}{R}\sum_{j=-\infty}^{\infty} e^{ij(\phi-\phi')}\int_0^\infty J_j\left(\frac{x\rho}{R}\right)J_j\left(\frac{x\rho'}{R}\right)e^{-\frac{x}{R}|z-z'|}dx,\end{aligned} \tag{A.1}$$

where the change of variable $x \to x/R$ has been used so the integral in the former equation is dimensionless.

A.1 Magnetostatic potential

Consider the nanotube described in Fig. 2.3. It has 4 surfaces: two ends at $z = -L/2, L/2$ and two cylindrical mantles at $\rho = \beta R, R$. The potential due to the external mantle is given by setting $\rho' = R$ on Eq. (1.20). The normal vector to the surface is $\hat{\boldsymbol{n}} = \hat{\boldsymbol{\rho}}$. Therefore, the superficial magnetic charges are given by

$$\sigma_\mathrm{m} = \hat{\boldsymbol{n}}\cdot\boldsymbol{M} = M_\mathrm{s}\cos(n\phi + q_z z). \tag{A.2}$$

[1]For details refer to problem 3.16.

In the other surface. The surface differential $dS' = Rd\phi' dz'$, so that:

$$\Phi_S^{\text{ext}} = \iint_{\text{ext}} \frac{M_\rho(\boldsymbol{r}')}{4\pi|\boldsymbol{r}-\boldsymbol{r}'|} dS' = \frac{M_s R}{4\pi} \int_0^{2\pi} \int_{-L/2}^{L/2} \frac{m_\rho(\phi', z')}{|\boldsymbol{r}-\boldsymbol{r}'|} dz' d\phi'.$$

Using expansion (A.1), integration on the azimuthal angle ϕ' yields nonzero terms only for $j = \pm n$. Also, using the relation $J_{-n}(x) = (-1)^n J_n(x)$:

$$\Phi_S^{\text{ext}} = \frac{M_s \sin\theta}{2} \int_{-L/2}^{L/2} \int_0^{\infty} e^{-\frac{x}{R}|z-z'|} J_n\left(\frac{x\rho}{R}\right) J_n(x) \cos(n\phi + q_z z') dx dz'. \tag{A.3}$$

Integration with respect to variable z' yields an analytical expression

$$\gamma_{n,q_z}(x, z, \phi) = \int_{-L/2}^{L/2} e^{-\frac{x}{R}|z-z'|} \cos(n\phi + q_z z') dz', \tag{A.4}$$

so we can write the resulting potential (A.3) as

$$\Phi_S^{\text{ext}} = \frac{M_s \sin\theta}{2} \int_0^{\infty} J_n\left(\frac{x\rho}{R}\right) J_n(x) \gamma_{n,q_z}(x, z, \phi) dx.$$

Note that the procedure to obtain the potential of the internal surface is analogous, identifying $\hat{\boldsymbol{\rho}} \to -\hat{\boldsymbol{\rho}}$ and $\rho' \to R_i = \beta R$:

$$\Phi_S^{\text{int}} = -\frac{\beta M_s \sin\theta}{2} \int_0^{\infty} J_n\left(\frac{x\rho}{R}\right) J_n(x\beta) \gamma_{n,q_z}(x, z, \phi) dx. \tag{A.5}$$

Now consider the top surface with $z' = L/2$. Again, it is easy to see that the normal vector to the surface is $\hat{\boldsymbol{n}} = \hat{\boldsymbol{z}}$ and the surface differential $dS' = \rho' d\rho' d\phi'$. The z component of the magnetization is constant, then the potential is calculated as

$$\Phi_S^{\text{top}} = \iint_{\text{top}} \frac{M_z(\boldsymbol{r}')}{4\pi|\boldsymbol{r}-\boldsymbol{r}'|} dS' = \frac{M_s \cos\theta}{4\pi} \int_0^{2\pi} \int_{\beta R}^{R} \frac{\rho' d\rho' d\phi'}{|\boldsymbol{r}-\boldsymbol{r}'|}.$$

Again, using Eq. (A.1), integration on the azimuthal angle is nonzero only for $j = 0$. Also, integration with respect variable ρ' yields an analytical expression, resulting in

$$\Phi_S^{\text{top}} = \frac{R M_s \cos\theta}{2} \int_0^{\infty} \frac{e^{-\frac{x}{R}(L/2-z)}}{x} J_0\left(\frac{x\rho}{R}\right) g_1(x) dq, \tag{A.6}$$

where $g_n(x) = J_n(x) - \beta J_n(\beta x)$. Integration in the bottom-end surface is analogous. Setting $|z - z'| = L/2 - z \to z + L/2$ and the normal vector $\hat{\boldsymbol{z}} \to -\hat{\boldsymbol{z}}$, the potential of the bottom end is

$$\Phi_{\mathrm{S}}^{\mathrm{bot}} = -\frac{RM_{\mathrm{s}}\cos\theta}{2}\int_0^\infty \frac{e^{-\frac{x}{R}(L/2+z)}}{x} J_0\left(\frac{x\rho}{R}\right) g_1(x)dx. \tag{A.7}$$

The total surface dipolar potential is given by all four contributions $\Phi_{\mathrm{S}} = \Phi_{\mathrm{S}}^{\mathrm{ext}} + \Phi_{\mathrm{S}}^{\mathrm{int}} + \Phi_{\mathrm{S}}^{\mathrm{top}} + \Phi_{\mathrm{S}}^{\mathrm{bot}}$:

$$\Phi_{\mathrm{S}} = M_{\mathrm{s}}\int_0^\infty \left(\frac{\sin\theta}{2}\gamma_{n,q_z}(x,z,\phi)J_n\left(\frac{x\rho}{R}\right)g_n(x) + R\cos\theta J_0\left(\frac{x\rho}{R}\right)g_1(x)\frac{e^{-\frac{xL}{2R}}}{x}\sinh\left(\frac{xz}{R}\right)\right)dx. \tag{A.8}$$

To obtain the volume term, consider the volumetric effective magnetic charges:

$$\sigma_{\mathrm{m}} = -\boldsymbol{\nabla}\cdot\boldsymbol{m} = -\frac{1}{\rho}m_\rho - \frac{1}{\rho}\frac{\partial m_\phi}{\partial\phi} = -\frac{n+1}{\rho}\cos(n\phi + q_z z)\sin\theta. \tag{A.9}$$

Volumetric charges appear due to oscillations in the azimuthal direction. This term is proportional to $\sim 1/\rho$, so it is larger for small-radius nanotubes. Considering that integration on azimuthal angle yields nonzero terms only for $j = \pm n$, and integration on z is the same as in (A.4), the volume potential results in

$$\begin{aligned}
\Phi_{\mathrm{V}} &= -\int_{\beta R}^{R}\int_{-L/2}^{L/2}\int_0^{2\pi}\frac{M_{\mathrm{s}}}{|\boldsymbol{r}-\boldsymbol{r'}|}(\boldsymbol{\nabla}\cdot\boldsymbol{m})\rho' d\phi' dz' d\rho' \\
&= -\frac{(n+1)M_{\mathrm{s}}\sin\theta}{2R}\int_0^\infty\int_{\beta R}^{R}\int_{-L/2}^{L/2} J_n\left(\frac{x\rho'}{R}\right)J_n\left(\frac{x\rho}{R}\right)\cos(n\phi + q_z z')e^{-\frac{x}{R}|z-z'|}dz'd\rho' dx \\
&= -\frac{(n+1)M_{\mathrm{s}}\sin\theta}{2}\int_0^\infty J_n\left(\frac{x\rho}{R}\right)\gamma_{n,q_z}(x,z,\phi)\Omega_n(x)dx
\end{aligned} \tag{A.10}$$

where $\Omega_n(x) = \int_\beta^1 J_n(ux)du$.

A.2 Dipolar Energy

With the total potential $\Phi = \Phi_S + \Phi_V$, the dipolar effective field is obtained using ∇ operator in cylindrical coordinates

$$\nabla = \hat{\boldsymbol{\rho}}\frac{\partial}{\partial \rho} + \frac{\hat{\boldsymbol{\phi}}}{\rho}\frac{\partial}{\partial \phi} + \hat{z}\frac{\partial}{\partial z}, \tag{A.11}$$

to find the normalized energy given by

$$\epsilon_d = \frac{E_d}{\mu_0 M_s^2 V} = \frac{1}{2M_s}\iiint_V \boldsymbol{m}\cdot\nabla\Phi\, dV. \tag{A.12}$$

Note that the potential dependence on variable ϕ is only through function γ_{n,q_z} (equations (A.10) and (A.8)). Additionally, note that:

$$\int_0^{2\pi}\frac{\partial \gamma_{n,q_z}}{\partial z}d\phi = \int_0^{2\pi}\cos(n\phi + q_z z)d\phi = 0, \tag{A.13}$$

for $n \neq 0$. Consequently:

$$\begin{aligned}
\epsilon_d &= \frac{1}{2M_s V}\int_V \boldsymbol{m}\cdot\nabla(\Phi_S + \Phi_V)dV \\
&= \frac{1}{2M_s V}\int_V \left(m_\rho\frac{\partial\Phi}{\partial\rho} + \frac{m_\phi}{\rho}\frac{\partial\Phi}{\partial\phi} + m_z\frac{\partial\Phi}{\partial z}\right)dV \\
&= \frac{1}{4VR}\int_0^\infty\int_V \cos(n\phi + q_z z)\sin^2\theta x J_n'\left(\frac{x\rho}{R}\right)\gamma_{n,q_z}(x,z,\phi)[g_n(x) - (n+1)\Omega_n(x)]dVdx + \\
&\quad + \frac{1}{4V}\int_0^\infty\int_V \frac{1}{\rho}\sin(n\phi + q_z z)\sin^2\theta\frac{\partial\gamma_{n,q_z}(x,z,\phi)}{\partial\phi}J_n\left(\frac{x\rho}{R}\right)[g_n(x) - (n+1)\Omega_n(x)]dVdx + \\
&\quad + \frac{1}{4V}\int_0^\infty\int_V 2\cos^2\theta J_0\left(\frac{x\rho}{R}\right)g_1(x)e^{-\frac{xL}{2R}}\cosh\left(\frac{xz}{R}\right)dVdx.
\end{aligned}$$

The term on the RHS proportional to $\cos^2\theta$ reduces to,

$$\frac{N_z}{2} = \frac{R}{L(1-\beta^2)}\int_0^\infty g_1(x)^2\left(\frac{1 - e^{-\frac{xL}{R}}}{x^2}\right)dx \tag{A.14}$$

which is the same demagnetization term reported on reference [44]. Integration with respect to variables ϕ, z of the remaining terms can be done and expressed

in terms of the following function:

$$\alpha_{q_z}(x) = \frac{1}{2\pi R^2}\int_0^{2\pi}\int_{-L/2}^{L/2}\cos(n\phi + q_z z)\gamma_{n,q_z}(x,z,\phi)dzd\phi$$
$$= \left(-\frac{1}{n}\right)\frac{1}{2\pi R^2}\int_0^{2\pi}\int_{-L/2}^{L/2}\sin(n\phi + q_z z)\frac{\partial\gamma_{n,q_z}(x,z,\phi)}{\partial\phi}dzd\phi \tag{A.15}$$
$$= \frac{(x^2+q_z^2R^2)Lx/R - (x^2-q_z^2R^2) - e^{-\frac{xL}{R}}(2xq_zR\sin(q_zL) + (x^2-q_z^2R^2)\cos(q_zL))}{\left(x^2+q_z^2R^2\right)^2}, \tag{A.16}$$

so terms proportional to $\sin^2\theta$ are given by the expression

$$\frac{N_{\text{ch}}}{2} = \frac{R}{2L(1-\beta^2)}\int_0^\infty \alpha_{q_z}(x)[g_n(x) - (n+1)\Omega_n(x)] \cdot \int_\beta^1 (xuJ_n'(xu) - nJ_n(xu))dudx. \tag{A.17}$$

This can be further simplified using the following identities [77]

$$nJ_n(x) = \frac{x}{2}(J_{n-1}(x) + J_{n+1}(x))$$
$$J_n'(x) = \frac{1}{2}(J_{n-1}(x) - J_{n+1}(x)),$$

so that

$$g_n(x) = J_n(x) - \beta J_n(\beta x) = \int_\beta^1 \frac{d}{du}[uJ_n(xu)]du$$
$$= \int_\beta^1 (J_n(xu) + xuJ_n'(xu))du,$$

and

$$\begin{aligned} g_n(x) - (1+n)\Omega_n(x) &= \int_\beta^1 (J_n(xu) - xuJ'(xu) - (1+n)J_n(xu))du \\ &= \int_\beta^1 (xuJ_n'(xu) - nJ_n(xu))du \\ &= \int_\beta^1 \left\{ \frac{xu}{2}(J_{n-1}(xu) - J_{n+1}(xu)) - \frac{xu}{2}(J_{n-1}(xu) + J_{n+1}(xu)) \right\} du \\ &= -\int_\beta^1 xuJ_{n+1}(xu)du \\ &= -\Lambda_{n+1}(x). \end{aligned}$$

Then, Eq. (A.17) reduces to

$$\frac{N_{\mathrm{ch}}}{2} = \frac{R}{2L(1-\beta^2)} \int_0^\infty \alpha_{q_z}(x)(\Lambda_{n+1}(x))^2 dx. \tag{A.18}$$

This term is quadratic in Λ_{n+1}, therefore it has the property $N_{\mathrm{ch}}(n) = N_{\mathrm{ch}}(-n-2)$. The total dipolar energy for $n \neq 0$ finally results in

$$\epsilon_{\mathrm{d}} = \frac{N_{\mathrm{ch}}}{2} \sin^2\theta + \frac{N_z}{2} \cos^2\theta. \tag{A.19}$$

This energy term can be approximated as a local radial anisotropy, as discussed in Sec. 2.1.3. It is expected that the local anisotropy approximation does not work for low aspect ratio R/L nanotubes. In determining the lower value of n and q_z, the full dipolar term must be calculated. The term N_{ch} is plotted as a function of the nanotubes' height L for a radius $R = 18$ nm and thickness $R-a = 3$ nm in Fig. A.1 for $n = 1, 2, 3$. The numerical calculations show small deviations from the anisotropy approximation. As a reference, the dimensionless energy difference between two $n-$states of the DMI is calculated for the same set of parameters and a small DMI value $D = 1 * 10^-3$ and shown in the figure $\Delta\epsilon_{\mathrm{dmi}} \approx 0.076$. A close look at the energy is shown in the inset, which shows small deviations from the anisotropy approximation. The largest energy difference of the dipolar term is between the $n = 1$ and $n = 2$ states at $L = 100$ nm, and it is found to be $\Delta\epsilon_{\mathrm{d}} \approx 0.005$, namely 15 times lower than the DMI contribution. As a consequence, the energy difference is negligible in determining the value of n that maximizes the nucleation field, which holds even for thicker nanotubes,

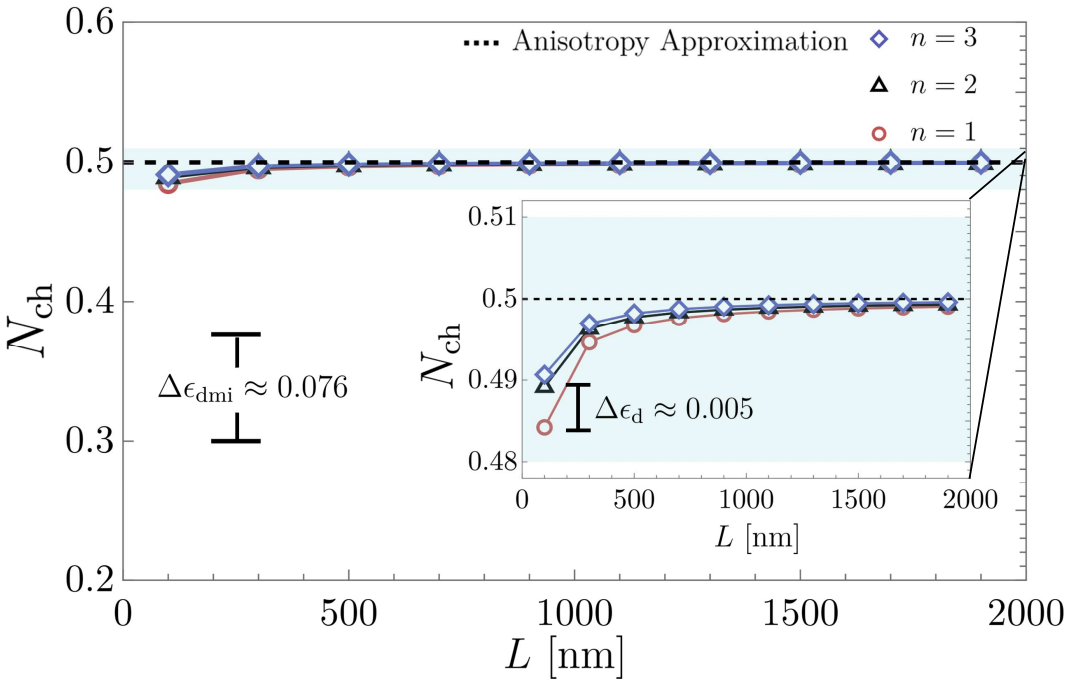

Figure A.1: Numerical calculation of the dipolar dimensionless N_{CH} term of a nanotube of radius $R = 18$ nm and thickness $R - a = 3$ nm as a function of the height L. A value $q_z = 0$ is considered. Three values of the azimuthal index are considered: $n = 1$ (red circles), $n = 2$ (black triangles) and $n = 3$ (blue diamonds). The radial anisotropy approximation as described in Sec. 2.1.3 is plotted in the dashed black line. The energy difference between two $\Delta\epsilon_{dmi} = \epsilon_{dmi}(n+1) - \epsilon_{dmi}(n)$ states given for reference for $D = 1$ mJ/m^2. The inset shows a close up of the dipolar energy. The higher difference value is given $\Delta\epsilon_d$ for a $L = 100$ nm nanotube between the $n = 1$ and $n = 2$ state.

which are out of the scope of this work.

Appendix B

DMI Effective Field on Magnetic Nanotubes

The energy of interfacial DMI is given by Eq. (1.24). The effective magnetic field can be obtained from Eq. (1.6). Using definition (1.3):

$$\delta E_{\text{dmi}} = \frac{\mathrm{d}}{\mathrm{d}\epsilon} \iiint_V w(\boldsymbol{m} + \epsilon \boldsymbol{v}) dV. \tag{B.1}$$

The objective of this calculation is to achieve the structure of Eq. (1.4), that is, $\iiint (\sim) \cdot \boldsymbol{v} dV + \iint (\sim) \cdot \boldsymbol{v} dS$. Explicitly,

$$w(\boldsymbol{m} + \epsilon \boldsymbol{v}) = D\hat{\boldsymbol{\rho}}[(\boldsymbol{m} + \epsilon \boldsymbol{v})(\nabla \cdot (\boldsymbol{m} + \epsilon \boldsymbol{v})) - ((\boldsymbol{m} + \epsilon \boldsymbol{v}) \cdot \nabla)(\boldsymbol{m} + \epsilon \boldsymbol{v})]. \tag{B.2}$$

Then Eq. (B.1) reduces to,

$$\begin{aligned} \delta E_{\text{dmii}} &= D \iiint_V \hat{\boldsymbol{\rho}} \cdot [\boldsymbol{m}(\nabla \cdot \boldsymbol{v}) + \boldsymbol{v}(\nabla \cdot \boldsymbol{m}) - (\boldsymbol{m} \cdot \nabla)\boldsymbol{v} - (\boldsymbol{v} \cdot \nabla)\boldsymbol{m}] dV \\ &= D \iiint_V \boldsymbol{\rho}(\nabla \cdot \boldsymbol{m}) \cdot \boldsymbol{v} dV + \\ & D \iiint_V [m_\rho(\nabla \cdot \boldsymbol{v}) - \hat{\boldsymbol{\rho}} \cdot (\boldsymbol{m} \cdot \nabla)\boldsymbol{v} - \hat{\boldsymbol{\rho}} \cdot (\boldsymbol{v} \cdot \nabla)\boldsymbol{m}] dV, \end{aligned} \tag{B.3}$$

The first term on the RHS has the structure required. The integrand of the second term on RHS is given by

$$(\text{RHS - second term}) = m_j \rho_j (\partial_k v_k) - \rho_j m_k \partial_k v_j - \rho_j v_k \partial_k m_j, \tag{B.4}$$

where a summation over repeated indices is assumed. Then, considering the following identities

$$m_j\rho_j\partial_k v_k = \partial_k(m_j\rho_j v_k) - v_k\partial_k(m_j\rho_j) \tag{B.5a}$$

$$\rho_j m_k\partial_k v_j = \partial_k(m_k\rho_j v_j) - v_j\partial_k(m_k\rho_j) = \partial_k(m_k\rho_j v_j) - v_j\rho_j\partial_k m_k - v_j m_k\partial_k\rho_j \tag{B.5b}$$

$$\rho_j v_k(\partial_k m_j) = v_k\partial_k(m_j\rho_j) - v_k m_j\partial_k\rho_j. \tag{B.5c}$$

Eq. (B.4) results in

$$\begin{aligned}\text{(RHS - second term)} =&\partial_k(m_j\rho_j v_k - m_k\rho_j v_j) - 2v_k\partial_k(m_j\rho_j)\\ &+ v_j\rho_j\partial_k m_k + v_j m_k\partial_k\rho_j + v_k m_j\partial_k\rho_j.\end{aligned} \tag{B.6}$$

Then,

$$\begin{aligned}\delta E_{\text{dmii}} =&D\iiint_V \boldsymbol{v}\cdot 2(\hat{\boldsymbol{\rho}}(\nabla\cdot\boldsymbol{m}) - \nabla(\hat{\boldsymbol{\rho}}\cdot\boldsymbol{m}))dV\\ &+ D\iiint_V [\boldsymbol{v}\cdot(\boldsymbol{m}\cdot\nabla)\hat{\boldsymbol{\rho}} + \boldsymbol{m}\cdot(\boldsymbol{v}\cdot\nabla)\hat{\boldsymbol{\rho}}]dV\\ &+ D\iiint_V \nabla\cdot[(\boldsymbol{m}\cdot\hat{\boldsymbol{\rho}})\boldsymbol{v} - (\boldsymbol{v}\cdot\hat{\boldsymbol{\rho}})\boldsymbol{m}]dV\end{aligned} \tag{B.7}$$

The derivatives on the second integral can be explicitly calculated, noting that $\hat{\boldsymbol{\rho}} = (x, y)/\sqrt{x^2+y^2}$:

$$[\boldsymbol{v}\cdot(\boldsymbol{m}\cdot\nabla)\hat{\boldsymbol{\rho}} + \boldsymbol{m}\cdot(\boldsymbol{v}\cdot\nabla)\hat{\boldsymbol{\rho}}] = \frac{2(\hat{\boldsymbol{\rho}}\times\boldsymbol{m})\cdot(\hat{\boldsymbol{\rho}}\times\boldsymbol{v}) - 2m_z v_z}{\rho}, \tag{B.8}$$

and using the identity $(\boldsymbol{a}\times\boldsymbol{b})\cdot(\boldsymbol{c}\times\boldsymbol{d}) = (\boldsymbol{a}\cdot\boldsymbol{c})(\boldsymbol{b}\cdot\boldsymbol{d}) - (\boldsymbol{a}\cdot\boldsymbol{d})(\boldsymbol{b}\cdot\boldsymbol{c})$ it results in

$$\begin{aligned}[\boldsymbol{v}\cdot(\boldsymbol{m}\cdot\nabla)\hat{\boldsymbol{\rho}} + \boldsymbol{m}\cdot(\boldsymbol{v}\cdot\nabla)\hat{\boldsymbol{\rho}}] =&\frac{2(\hat{\boldsymbol{\rho}}\cdot\hat{\boldsymbol{\rho}})(\boldsymbol{m}\cdot\boldsymbol{v}) - (\hat{\boldsymbol{\rho}}\cdot\boldsymbol{v})(\hat{\boldsymbol{\rho}}\cdot\boldsymbol{m}) - (\boldsymbol{m}\cdot\hat{\boldsymbol{z}})(\boldsymbol{v}\cdot\hat{\boldsymbol{z}})}{\rho}\\ =&\boldsymbol{v}\cdot\frac{2(\boldsymbol{m} - m_\rho\hat{\boldsymbol{\rho}} - m_z\hat{\boldsymbol{z}})}{\rho}\\ =&\boldsymbol{v}\cdot\frac{2m_\phi\hat{\boldsymbol{\phi}}}{\rho}.\end{aligned} \tag{B.9}$$

Finally, the last term can be transformed into a surface integral using Gauss' theorem

$$\begin{aligned} D\iiint_V \nabla\cdot[(\boldsymbol{m}\cdot\hat{\boldsymbol{\rho}})\boldsymbol{v}-(\boldsymbol{v}\cdot\hat{\boldsymbol{\rho}})\boldsymbol{m}]dV &= D\iint_{\partial V}[(\boldsymbol{m}\cdot\hat{\boldsymbol{\rho}})\boldsymbol{v}-(\boldsymbol{v}\cdot\hat{\boldsymbol{\rho}})\boldsymbol{m}]\cdot\hat{\boldsymbol{n}}dS \\ &= D\iint_{\partial V}[(\boldsymbol{m}\cdot\hat{\boldsymbol{\rho}})\hat{\boldsymbol{n}}-\hat{\boldsymbol{\rho}}(\boldsymbol{m}\cdot\hat{\boldsymbol{n}})]\cdot\boldsymbol{v}dS \\ &= D\iint_{\partial V}[\boldsymbol{m}\times(\hat{\boldsymbol{n}}\times\hat{\boldsymbol{\rho}})]\cdot\boldsymbol{v}dS, \end{aligned} \tag{B.10}$$

where the following identity has been used $\boldsymbol{a}\times(\boldsymbol{b}\times\boldsymbol{c})=(\boldsymbol{a}\cdot\boldsymbol{c})\boldsymbol{b}-(\boldsymbol{a}\cdot\boldsymbol{b})\boldsymbol{c}$. The final result is

$$\begin{aligned} \delta E_{\mathrm{dmii}} = D\iiint_V \boldsymbol{v}\cdot 2\left(\hat{\boldsymbol{\rho}}(\nabla\cdot\boldsymbol{m})-\nabla(\hat{\boldsymbol{\rho}}\cdot\boldsymbol{m})+\frac{m_\phi}{\rho}\hat{\boldsymbol{\phi}}\right)dV \\ +\iint_{\partial V}[\boldsymbol{m}\times(\hat{\boldsymbol{n}}\times\hat{\boldsymbol{\rho}})]\cdot\boldsymbol{v}dS. \end{aligned} \tag{B.11}$$

The terms in Eq. (1.3) are identified to obtain the effective interfacial DMI field

$$\boldsymbol{H}_{\mathrm{dmi}} = -\frac{2D}{\mu_0 M_{\mathrm{s}}}\left(\hat{\boldsymbol{\rho}}(\nabla\cdot\boldsymbol{m})-\nabla(\hat{\boldsymbol{\rho}}\cdot\boldsymbol{m})+\frac{m_\phi}{\rho}\hat{\boldsymbol{\phi}}\right) \tag{B.12}$$

$$\boldsymbol{B}_{\mathrm{dmi}} = [\boldsymbol{m}\times(\boldsymbol{n}\times\hat{\boldsymbol{\rho}})] \tag{B.13}$$

Suppose that the normal vector is not $\hat{\boldsymbol{\rho}}$ but an arbitrary $\hat{\boldsymbol{n}}$. If the energy term is the same, the extra term is

$$= \frac{1}{2}(\nabla\hat{\boldsymbol{n}})^{\mathrm{T}}+\frac{1}{2}(\boldsymbol{m}\cdot\nabla)\hat{\boldsymbol{n}} \tag{B.14}$$

so that

$$\boldsymbol{H}_{\mathrm{dmi}} = -\frac{2D}{\mu_0 M_{\mathrm{s}}}\left(\hat{\boldsymbol{n}}(\nabla\cdot\boldsymbol{m})-\nabla(\hat{\boldsymbol{n}}\cdot\boldsymbol{m})+\frac{1}{2}(\nabla\hat{\boldsymbol{n}})^{T}\boldsymbol{m}+\frac{1}{2}(\boldsymbol{m}\cdot\nabla)\hat{\boldsymbol{n}}\right) \tag{B.15}$$

which coincides with $+(m_\phi/\rho)\hat{\boldsymbol{\phi}}$ if $\hat{\boldsymbol{n}}=\hat{\boldsymbol{\rho}}$.

Appendix C

Reversal Modes on Magnetic Nanotubes

The conical-helix (CH) magnetization model has to be compared with other known reversal modes in long nanotubes like the uniform mode (U), the curling mode (C), and the Hedgehog mode (Hg) [44, 80]. The normalized magnetization fields that describe the U, C, and Hg reversal modes respectively are

$$\boldsymbol{m}^{\mathrm{u}} = \sin\theta\hat{\boldsymbol{x}} + \cos\theta\hat{\boldsymbol{z}} \tag{C.1a}$$

$$\boldsymbol{m}^{\mathrm{c}} = \mathrm{C}\sin\theta\hat{\boldsymbol{\phi}} + \cos\theta\hat{\boldsymbol{z}} \tag{C.1b}$$

$$\boldsymbol{m}^{\mathrm{hg}} = \sin\theta\hat{\boldsymbol{\rho}} + \cos\theta\hat{\boldsymbol{z}}, \tag{C.1c}$$

where θ is the angle between $\boldsymbol{m}$ and the applied magnetic field along the z-axis. First of all, notice that the U mode can be obtained as a part of the CH model (2.1) by setting $n = -1$ and $q_z = 0$. Although the Hg mode is obtained similarly with $n = q_z = 0$, this special case yields different values of the energy than the ones obtained in Section 2.1. A phase ψ could be added in the CH model to obtain the C mode at $n = q_z = 0$ and $\psi = \pi/2$. However, this phase's role is only to move the CH texture along the z axis and consequently modify the tube ends contribution, but since the dipolar interaction is approximated as a local anisotropy, the energy of the texture is unaltered. Instead, the C and Hg states are analyzed separately. The addition of interfacial DMI is straightforward using Eq. (1.24), so that the total energy—considering the local approximation of the dipolar energy (2.11) and the addition of interfacial DMI is given by [44]:

$$\epsilon^{\mathrm{c}} = -\frac{H_{\mathrm{n}}^{\mathrm{c}}}{2M_{\mathrm{s}}}\sin^2\theta - \frac{H}{M_{\mathrm{s}}}\cos\theta \tag{C.2a}$$

$$\epsilon^{\mathrm{hg}} = -\frac{H_{\mathrm{n}}^{\mathrm{hg}}}{2M_{\mathrm{s}}}\sin^2\theta - \frac{H}{M_{\mathrm{s}}}\cos\theta, \tag{C.2b}$$

where nucleation fields are respectively

$$H_{\mathrm{n}}^{\mathrm{c}} = -\frac{4A\ln 1/\beta}{\mu_0 M_{\mathrm{s}} R^2(1-\beta^2)} - \frac{4D}{\mu_0 M_{\mathrm{s}} R(1+\beta)} \tag{C.3a}$$

$$H_{\mathrm{n}}^{\mathrm{hg}} = (Q-1)M_{\mathrm{s}} - \frac{4A\ln 1/\beta}{\mu_0 M_{\mathrm{s}} R^2(1-\beta^2)} - \frac{4D}{\mu_0 M_{\mathrm{s}} R(1+\beta)}. \tag{C.3b}$$

Appendix D

Low energy approximation of SW dynamics

The low k approximation of integrals defined in Eqns.(3.39) can be computed analytically using complex variable theory. Only the most important used mathematical tools are listed in the following section. For extensive details and demonstrations, see Ref.[77].

D.1 Mathematical tools: complex analysis

A point z_0 is called a *pole* of the function $f(z)$ if f is not analytic at $z = z_0$ but is analytic at all neighboring points. The order n of the pole is defined as the smallest integer n such that the limit

$$\lim_{z \to z_0} (z - z_0)^n f(z_0) \tag{D.1}$$

exists. The *residue* of a function $f(z)$ is defined as the $n = -1$ coefficient in the Laurent series expansion around z_0:

$$f(z) = \sum_{n=-\infty}^{\infty} a_n (z - z_0)^n \qquad \text{res}_{z_0}(f) = a_{-1}. \tag{D.2}$$

The residue of first order pole can be computed as

$$a_{-1} = \lim_{z \to z_0} (z - z_0) f(z), \tag{D.3}$$

while for a pole of order $n > 1$

$$a_{-1} = \frac{1}{(n-1)!} \lim_{z \to z_0} \left[\frac{d^{n-1}}{dz^{n-1}} (z - z_0)^n f(z) \right] \tag{D.4}$$

The *residue theorem* allows to replace the problem of evaluating contour integrals by the algebraic problem of computing residues at the enclosed singular points. That is:

$$\oint_C f(z)dz = 2\pi i \sum_C \text{res}(f), \tag{D.5}$$

where the sum is over the integrals enclosed by the curve C. Consider the integral of the form,

$$I = \int_0^{2\pi} f(\sin\theta, \cos\theta)d\theta \tag{D.6}$$

where f is finite for all values of θ. This integral can be solved by using the change of variable $z = e^{i\theta}$, thus,

$$d\theta = -i\frac{dz}{z}, \quad \sin\theta = \frac{z - z^{-1}}{2i}, \quad \cos\theta = \frac{z + z^{-1}}{2}. \tag{D.7}$$

The integral (D.6) results then in,

$$I = -i \oint_{\partial C} f\left(\frac{z - z^{-1}}{2i}, \frac{z + z^{-1}}{2} \right) \frac{dz}{z} \tag{D.8}$$

where ∂C is the circumference of radius $r = 1$. Applying the residue theroem (Eqn. (D.5)), the integral is computed by calculating the residues inside the unit circle C:

$$I = 2\pi \sum_C \text{res}(f/z) \tag{D.9}$$

To calculate this integral, it is sufficient to calculate the residues at the poles inside C.

D.2 Low k approximation

An analytical expression can be found for the dipolar tensor $\mathbf{\Lambda}_\text{d}$ close to $k \approx 0$ by using a first-order approximation of the Bessel function $K_0(x) \approx -\ln\frac{x}{2} - \gamma + \mathcal{O}(x^2)$, where $\gamma = 0.577\ldots$ is the Euler-Mascheroni constant. The G_0 function

(3.36a) is then given up to first order in kR by,

$$G_0(\rho,\rho,\phi') \approx \tilde{G}_0(\rho,\rho,\phi') = \frac{e^{i\phi' l}}{2\pi R\,(1-\beta)}\Gamma(\rho,\rho',\phi'). \tag{D.10}$$

where, $\Gamma(\rho,\rho',\phi') = -\ln\left(\frac{|k|}{2}\sqrt{\rho^2 - 2\rho\rho'\cos\phi' + \rho'^2}\right) - \gamma$.

D.2.1 Computation of I_0

To avoid singularities at $\phi' = 0$, the former function is evaluated by slightly modifying the consideration of Eq. (3.37), namely $G_0(R_\mathrm{m}, R_\mathrm{m}+\delta, \phi')$, where δ is a small parameter. This allows to use integration by parts for $l \neq 0$,

$$\begin{aligned} I_0^\delta &= \frac{1-\beta}{\pi(1+\beta)}\left(\left[\frac{e^{i\phi' l}}{l}\Gamma(R_\mathrm{m}, R_\mathrm{m}+\delta,\phi')\right]\Big|_0^{2\pi} - \int_0^{2\pi}\frac{e^{il\phi'}}{l}\partial_{\phi'}\Gamma(R_\mathrm{m}, R_\mathrm{m}+\delta,\phi')d\phi'\right) \\ &= -\frac{1-\beta}{\pi(1+\beta)}\int_0^{2\pi}\frac{e^{il\phi'}}{l}\partial_{\phi'}\Gamma(R_\mathrm{m}, R_\mathrm{m}+\delta,\phi')d\phi', \end{aligned} \tag{D.11}$$

so that $I_0 = \lim_{\delta\to 0} I_0^\delta$. Note that,

$$\begin{aligned} f_l^0(\sin\phi',\cos\phi') &= \frac{e^{il\phi'}}{l}\partial_{\phi'}\Gamma(R_\mathrm{m}, R_\mathrm{m}+\delta,\phi') \\ &= -\frac{(\cos\phi' + i\sin\phi')^l}{l}\frac{R_\mathrm{m}\,(R_\mathrm{m}+\delta)\sin\phi'}{R_\mathrm{m}^2 - 2R_\mathrm{m}\,(R_\mathrm{m}+\delta)\cos\phi' + (R_\mathrm{m}+\delta)^2} \end{aligned} \tag{D.12}$$

this last function has the following property,

$$f_l^0(\sin\phi',\cos\phi') = f_{-l}^0(\sin(-\phi'),\cos(-\phi')) \tag{D.13}$$

and so,

$$\begin{aligned} I_0^\delta(-l) &= -\frac{1-\beta}{\pi(1+\beta)}\int_0^{2\pi} f_{-l}^0(\sin\phi',\cos\phi')d\phi' \\ &= -\frac{1-\beta}{\pi(1+\beta)}\int_0^{2\pi} f_l^0(\sin(-\phi'),\cos(-\phi'))d\phi' \\ &= -\frac{1-\beta}{\pi(1+\beta)}\int_{-2\pi}^{0} f_l^0(\sin\varphi,\cos\varphi)d\varphi = I_0^\delta(l) \end{aligned} \tag{D.14}$$

where the variable change $\varphi = -\phi'$ has been used. It is then sufficient to calculate the integral for $l > 0$. These integrals can be solved using the residue theorem by using Eq. (D.9). For $l > 0$, the only pole of the function f_l^0/z that fulfills the condition $|z| < 1$ is $z_0 = R_\mathrm{m}/(R_\mathrm{m} + \delta)$ and it is a pole of first order. According to Eq. (D.3), the residue is given by,

$$\mathrm{res}_{z_0} = \lim_{z\to z_0}\left(z - \frac{R_\mathrm{m}}{R_\mathrm{m}+\delta}\right)\frac{f_l^0\left(\frac{z-z^{-1}}{2i}, \frac{z+z^{-1}}{2}\right)}{z} = \frac{1}{2l}\left(\frac{R_\mathrm{m}}{R_\mathrm{m}+\delta}\right)^l \tag{D.15}$$

and then,

$$I_0^\delta = -\frac{1-\beta}{\pi(1+\beta)}(2\pi\mathrm{res}_{z_0}) = -\frac{1}{l}\left(\frac{1-\beta}{1+\beta}\right)\left(\frac{R_\mathrm{m}}{R_\mathrm{m}+\delta}\right)^l \tag{D.16}$$

so finally,

$$I_0 = \lim_{\delta\to 0} I_0^\delta = -\left(\frac{1-\beta}{1+\beta}\right)\frac{1}{|l|}. \tag{D.17}$$

where the absolute value has been added given that $I_0(l) = I_0(-l)$.

D.2.2 Computation of I_1

According to Eq. (3.39b) and using the approximation given by (D.10),

$$\begin{aligned} I_1 &= R^2(1-\beta)^2\int_0^{2\pi}(\partial_\rho\tilde{G}_0)(R_\mathrm{m}, R_\mathrm{m}, \phi)d\phi \\ &= -\frac{1}{2\pi}\left(\frac{1-\beta}{1+\beta}\right)\int_0^{2\pi} e^{i\phi' l}d\phi \\ &= -\left(\frac{1-\beta}{1+\beta}\right)\delta_{l0} \end{aligned} \tag{D.18}$$

D.2.3 Computation of I_2

To calculate the integral I_2, it is more convenient to use the integral $\Omega_3(\rho)$ in the form given by Eq. (3.31a). Then, from the potential form in equation (3.32a):

$$I_2 = \partial_\rho(-\Omega_1 + \Omega_3)(R_\mathrm{m}). \tag{D.19}$$

Using the approximated function (D.10) it is obtained,

$$I_2 = \int_0^{2\pi} \frac{e^{il\phi'}}{2\pi} \left(-\frac{1-\beta}{1+\beta} + \frac{2\beta(1+\beta-2\beta\cos\phi')}{4\beta^2 - 2\beta(1+\beta)\cos\phi' + (1+\beta)^2} - \frac{2(1+\beta-2\cos\phi')}{4-2(1+\beta)\cos\phi' + (1+\beta)^2} \right) d\phi'. \tag{D.20}$$

The first term on the RHS is the same as the one obtained in Eq. (D.18) so that $I_2 = I_1 + \int_0^{2\pi} f_l^2(\sin\phi', \cos\phi')d\phi'$. Again, it is necessary to calculate the residues inside the unit circle to obtain this integral. The singularities that fulfill this condition are $z_0 = 0$, $z_1 = 2\beta/(1+\beta)$ and $z_2 = (1+\beta)/2$. It is obtained,

$$\begin{aligned} I_2 &= I_1 + 2\pi(\mathrm{res}_{z_0} + \mathrm{res}_{z_1} + \mathrm{res}_{z_2}) \\ &= \frac{1}{1+\beta}\left(\left(\frac{1+\beta}{2}\right)^{|l|} + \beta\left(\frac{2\beta}{1+\beta}\right)^{|l|} \right) \end{aligned} \tag{D.21}$$

where the absolute value has been added due to the same argument given in equations (D.14), which can be used to conclude $I_2(l) = I_2(-l)$.

D.2.4 Summary of results

In summary, for $l = 0$:

$$I_0(l=0) = \frac{4(1-\beta)}{(1+\beta)^2}\left(\gamma + \ln\left(\frac{|k|R}{2}\right)\right) \tag{D.22a}$$

$$I_1(l=0) = -\left(\frac{1-\beta}{1+\beta}\right) \tag{D.22b}$$

$$I_2(l=0) = 1 \tag{D.22c}$$

while for $l \neq 0$ we get,

$$I_0 = \left(\frac{1-\beta}{1+\beta}\right)\frac{1}{|l|} \tag{D.23a}$$

$$I_1 = 0 \tag{D.23b}$$

$$I_2 = \frac{1}{1+\beta}\left(\left(\frac{1+\beta}{2}\right)^{|l|} + \beta\left(\frac{2\beta}{1+\beta}\right)^{|l|} \right) \tag{D.23c}$$